

Assembly and Characterization of Supramolecular Architectures for Biosensor Applications

Dissertation zur Erlangung des Grades
“Doktor der Naturwissenschaften”

am Fachbereich Biologie
der Johannes Gutenberg-Universität
in Mainz

vorgelegt von
Fei Xu
aus Changchun, Jilin, V. R. China

Mainz, Mai, 2005

Dekan: Prof. Dr. H. Paulsen

Tag der mündlichen Prüfung: 31, Mai 2005

Die vorliegende Arbeit wurde unter Betreuung von Herrn Prof. Dr. W. Knoll im Zeitraum zwischen Juli 2002 bis Mai 2005 am Max-Planck-Institute für Polymerforschung, Mainz, Deutschland angefertigt.

CONTENTS

1	INTRODUCTION.....	1
1.1	BIOSENSOR.....	1
1.1.1	<i>Optical fiber biosensors</i>	2
1.1.2	<i>Optical fiber biosensors based on immobilized enzymes</i>	3
1.2	SUPRAMOLECULAR ARCHITECTURES.....	4
1.2.1	<i>Hydrogel</i>	5
1.2.2	<i>Colloidal gold nanoparticles</i>	12
1.3	AIM OF THE STUDY.....	17
2	METHODS AND THEORIES.....	20
2.1	SURFACE PLASMON OPTICS.....	20
2.1.1	<i>Surface plasmon resonance spectroscopy (SPR)</i>	20
2.1.1.1	SPR principle.....	20
2.1.1.2	Surface Plasmon Spectroscopy with Prism Coupling.....	25
2.1.1.3	SPR Response to a Thin Film Deposition.....	28
2.1.2	<i>Surface Plasmon Field-Enhanced Fluorescence Spectroscopy (SPFS)</i>	31
2.1.2.1	Field Enhancement.....	31
2.1.2.2	Fluorescence at the Metal/Dielectric Interface.....	35
2.1.3	<i>Home-Made SPFS Setup</i>	39
2.2	ENZYMATIC ACTIVITY ASSAY.....	41
2.2.1	<i>Properties and classification of enzymes</i>	41
2.2.2	<i>Enzyme kinetics</i>	42
2.2.3	<i>Michaelis-Menten Kinetics</i>	45
2.2.4	<i>Lineweaver-Burk Plots</i>	47
2.2.5	<i>Combination of surface plasmon spectroscopy and fiber optic absorbance spectroscopy</i>	48
2.2.6	<i>Catalytic activity assay of β-lactamase</i>	49
2.3	LANGMUIR ISOTHERM.....	51
3	COMPARATIVE DETECTION OF INTERFACIAL BINDING OF β-LACTAMASE TO DIFFERENT MATRICES COMBINED WITH CATALYTIC ACTIVITY ASSAY.....	56
3.1	INTRODUCTION.....	56
3.2	MATERIALS.....	58
3.3	SUBSTRATES.....	59
3.4	COMPARISON OF SURFACE MODIFICATION BASED ON FIVE KINDS OF MATRICES.....	60
3.5	COMPARISON OF DIFFERENT OPTICAL DETECTION METHODS (OWLS AND SPR):.....	64
3.6	ESTIMATION OF REGENERATION POSSIBILITIES.....	65
3.7	ENZYME ACTIVITY ASSAY.....	67
3.8	CONCLUSION.....	73
4	QUANTIFICATION OF DNA HYBRIDIZATION BASED ON ORGANOMETALLIC CHEMICAL VAPOR DEPOSITION (OMCVD) GOLD PARTICLES.....	75
4.1	INTRODUCTION.....	75
4.2	MATERIALS.....	77

4.3	METHODS	80
4.4	COMPARATIVE QUANTIFICATION OF DNA HYBRIDIZATION BASED ON PLANAR AND GOLD PARTICLE MATRICES.....	83
4.5	NON-SPECIFIC BINDING OF DNA ON A OMCVD GOLD PARTICLE MATRIX.....	86
4.6	SEQUENCE-SPECIFIC DETECTION OF DNA HYBRIDIZATION BASED ON OMCVD GOLD PARTICLES.....	88
4.7	CONCLUSION AND OUTLOOK.....	88
5	EXTERNAL STIMULI AND INTERNAL CROSSLINK RESPONSES OF CARBOXYMETHYL DEXTRAN (CMD) FOR SURFACE PLASMON RESONANCE (SPR) APPLICATIONS.....	90
5.1	INTRODUCTION.....	90
5.2	MATERIALS.....	92
5.3	STIMULI RESPONSES OF CMD CHARACTERIZED FROM SPR SIMULATION	93
5.4	STIMULI RESPONSE OF FLUOROPHORES LABELED CMD DETECTED BY SPFS	97
5.5	INFLUENCE OF SURFACE CHARGE AND CROSSLINK DENSITIES ON THE STIMULI RESPONSES OF CMD.....	101
5.6	CONCLUSION	104
6	SUMMARY	105
7	SUPPLEMENT	108
7.1	ABBREVIATIONS	108
7.2	LIST OF FIGURES	110
7.3	LIST OF TABLES	113
7.4	BIBLIOGRAPHY	114
	CURRICULUM VITAE.....	121

1 INTRODUCTION

1.1 Biosensor

Biosensors are used to measure biological effects, such as genotoxicity, immunotoxicity, biotoxins, and endocrine effects. In addition, they are used to measure the concentration of specific analytes that are difficult to detect, which are usually important contaminants of water, waste water, soil, or air, for instance, surfactants, chlorinated hydrocarbons, and pesticides. Other benefits include simple operation, fast response times, high sensitivity, selectivity, in situ monitoring, compact, rugged, and miniature-size instrument, easy to interface, and integrate with microprocessors of signal devices. These qualities make biosensors eligible for different applications, such as in the biochemical field, environmental monitoring, clinical analysis, food processing, brewing, and pharmaceutical industries.

A biosensor device comprises of a biological recognition element directly interfaced to a signal transducer, which together relate the concentration of an analyte or group of analytes to a measurable response. A receptor is a biologically sensitive element of biosensors responsible for the recognition of an analyte and, to a large extent, for the specificity and sensitivity of the final device. These elements must be substances that can attach themselves to one particular substrate, but not to others. The biological component has to be properly attached to the transducer by immobilization. The immobilization method is determined by the nature of the biocomponent to be immobilized. The type of transducing element used and the physical properties of the analyte are also important factors that assist in selecting a method. Generally, there are five common methods of immobilization: adsorption, microencapsulation, entrapment, cross-linking, and covalent bonding.¹ The transducing element of a biosensor is used to convert the biological recognition step into an optical signal that can be coupled to a microprocessor for control and display. Transducers are mainly divided into four categories: electrochemical, optical, piezoelectric and calorimetric devices.

Generally, there are two categories of biosensors, as follows:

1) Affinity biosensors: In this type of biosensors, receptor molecules, such as antibodies, nucleic acids, lectins and hormone receptors, are used to bind molecules irreversibly and non-catalytically. The bioaffinity agents include biological components, such as antibodies, nucleic acids, dyes, cell membrane receptors and other specific binding agents. These biosensors pose the ability of affinity interactions to separate an individual or selected range of compounds from complex mixtures of biomolecules on the basis of chemical or biological function.²

2) Catalytic biosensors: In this type of biosensors, biocatalysts, such as enzymes and micro-biological cells, are used to recognize, bind, and chemically convert a molecule. Catalytic biosensors are based on the recognition and binding of an analyte followed by a catalyzed chemical conversion of the analyte from a non-detectable form to a detectable form, which is detected and recorded by a transducer.

1.1.1 Optical fiber biosensors

Optical biosensors, which comprise transducers for detecting the presence of biological molecules, are applied to measure the responses to illumination or to light emission. Compared with classical homogeneous solution methods for investigating molecular recognition, optical biosensors offer several assets: (1) generally there is no need to label the molecules being detected; (2) they can be used to monitor recognition processes in real time *in situ*; (3) many important biological recognition processes take place at surfaces, which is therefore a highly relevant environment; (4) signal/noise ratios are better, hence sensitivity is higher.

Optical biosensors also offer advantages in terms of miniaturization, low cost, disposability and no electrical interference. The optical technology can be applied to design absorbance, reflectance, fluorescence, fluorescence quenching, evanescent wave, surface plasmon resonance, and luminescence biosensors. These biosensors are constructed from electronic as well as standard optical components, which are light sources such as light-emitting diodes (LEDs), lasers, and detectors (photodiodes), as well as filters and lenses. Light-intensity measurements can be read directly or can be interpreted by standard analogue or digital circuitry.

Among optical biosensors, the most frequently and commercially available detection instrument is SPR or related spectroscopies (evanescent waveguide or refractometry) to monitor the changes of the refractive index at the solid/liquid interface. The first commercial SPR biosensor was released by Biacore (Uppsala, Sweden) in 1990³. Just as is indicated by the name of the company, BIA, which is the abbreviation of “biomolecular interaction analysis”, SPR instruments are designed to detect molecular recognitions and reactions on surfaces. A recent paper⁴ has documented that judicious use of SPR to measure interactions on the surface can provide data equivalent to, or better than, solution methods of analysis. SPFS (surface plasmon field-enhanced fluorescence spectroscopy)^{5,6}, recently developed and based on SPR technology, has enabled successful quantitative analysis of oligonucleotide and other trace targets. Moreover, the ability of SPFS for simultaneously monitoring

the interfacial refractive index changes and fluorescence variations presents the possibility of detecting biological activity detection of intrinsic fluorescent proteins or biomolecules.

Another kind of optical-biosensor applied in the study uses absorbance measurements to determine any changes in the concentration of analytes that absorb at a given wavelength of light. The systems work by transmitting light through an optical fiber to the sample; the amount of light absorbed by the analyte is detected through the same fiber or a second optical fiber. Such kind of optical fiber-based biosensors combine the use of a biological recognition element with an optical fiber or optical fiber bundle. Optical fiber biosensors mainly consist of fiber optic devices with an integrated biochemical transducer system, which changes its optical properties upon interaction with the analyte.⁷ In most instances, the optical fibers serve only as a light conduit to view the optical properties of the chemical transducing system, which is separately fabricated and only later attached to the fiber. The transduction reagent can be immobilized directly on a membrane, which is coupled to the fiber. The reagent can be in a powder or solid bead form, which is supported on the fiber end by a membrane. Another alternative is to bind the reagent directly to the fiber itself or to attach a thin layer of a reagent-containing polymer onto the fiber.⁸

Measurements for these sensors can be performed using single, dual, or multiple fiber arrangements. In a single fiber configuration, the same fiber is used to transport the excitation radiation from the source optics and the emitted radiation from the sensor tip to the detection optics. For dual or multiple fiber configurations, separate fibers or fiber bundles transmit the radiation to and from the reagent phase. Single fiber configurations have the advantage of a small sample volume. It is also more efficient optically since the overlap between the incident and collected radiation is maximized. The merits of a multiple fiber arrangement include a simpler instrumentation set-up, higher optical throughput (since more fibers transport the radiation), and the capability of using non-laser sources and relatively inexpensive detection systems.

1.1.2 Optical fiber biosensors based on immobilized enzymes

Enzymes are still indispensable tools in biosensing. The use of immobilized enzymes as the chemical transducing element for fiber optic sensors has provided a considerable advancement in the state of optical fiber sensing, due to the unique biocatalytic properties of enzymes, their remarkable specificity for a particular substrate or a certain group of substrates, the wide range of enzymes that are readily available. The focus of most studies involving immobilized enzymes and optical fiber devices has been mainly on the determination of enzyme substrates. This type of application has been

in the forefront of research in terms of the number of measured analytes, the body of published data, and the extent of adaptation in real sample analysis. As the recognition element, the immobilized enzyme here simply functions as the biocatalytic element of the sensing system. Since the enzymatic reaction is accompanied by the consumption or the production of low-molecular weight species, such as O₂, CO₂, NH₃, H₂O₂, or protons, a normal way for measuring the substrate concentration has been through the use of suitable optical transducers (e.g., pH, O₂, or NH₃ sensor). Substrates have also been measured in a more direct manner, whenever a luminescent or colored product is generated during the enzymatic reaction. In some instances, however, no readily optically detectable species may be produced from the reaction of a mono-enzyme system that multiple enzymes are utilized to produce the measurable species. Alternatively, classical photometric reactions have also been employed so that enzymatic product(s) is (are) converted to some colored or luminescent species and consequently monitored using the optical fibers.

Enzymes, in combination with catalytic biosensors, were utilized in their immobilized forms on the solid support working as a part of the affinity biosensor in this study. Generally, numerous methods can be utilized for the immobilization of enzymes to the devices, but generally the techniques comprise either chemical or physical methods. In this study, a covalent binding method which involves binding a functional group in the biomaterial to the support matrix was used. The immobilization of the enzymes confers a number of advantages for their application in optical sensors. It is more permanent, demonstrate from 4-14 months,¹ and offers the most stable immobilized enzyme preparation in that the immobilization process is not easily reversed by pH, ionic strength, temperature, or solvent variations. In many cases, the immobilized biomaterial achieves greater pH, thermal, and storage stability. Immobilization also allows for the reuse of the enzyme over an extended period of time, hence leading to greater reagent economy. Furthermore, it allows easier sensor manipulation and operation.

1.2 Supramolecular Architectures

The performance of any (bio-) medical device crucially depends on the proper functionalization of its surface. This is obviously true for prosthetic implants, for scaffolds used in cell and tissue engineering, or for biosensors and alike. The challenge is not only to generate a passive biocompatibility, i.e. to engineer the surface of the device such that any biomaterial-from proteins to cells and whole living tissues-tolerate the “foreign” object, the proper design and synthesis of surface

functional groups also control the desired active or interactive communication between the device and its bioenvironment. For the case of biosensors these criteria reduce to the seemingly “simple” requirements which the sensor surface needs to fulfill: an optimized density of highly selective and specific biofunctional groups for the recognition (and binding) of the analyte molecule of interest must be combined with a matrix that passivates the sensor surface for any unspecific and, hence, undesired interaction between the many other components in the analyte solution and the sensor surface.⁹

The fabrication of highly organized molecular systems opens up new vistas for the control of matter and the design of novel functional materials. In recent years significant progress was made in their assembly at solid surfaces, which can be directed and monitored in exquisite detail using physical nanoscience methods. Moreover, this approach facilitates integration in environments structured at a higher level.

1.2.1 Hydrogel

Hydrogels are three-dimensional, water-swallowable networks connected by chemical or physical crosslinks. One of the more interesting, and technology promising, features of hydrogels is their ability to transition in aqueous solutions from a collapsed state to a highly swollen one, in response to environmental changes.¹⁰⁻¹⁴ Charged, i.e. polyelectrolyte hydrogels are composed of polymer chains containing charged groups. Unlike the uncharged hydrogels, the dominant driving force for swelling in these systems is the inherent electrostatic repulsion between gel charges (cf. Figure 1.1): As a result, swelling of polyelectrolyte hydrogels can be induced through such stimuli as changes in pH and salinity.¹⁵⁻²⁹ The ability of charged hydrogels to transition, in response to an environmental trigger, from a collapsed to swollen configuration or vice versa may be utilized for various technological applications. For example, hydrogels have been widely examined as drug delivery agents^{11;30-32} where the swelling trigger leads to the release of pharmaceuticals entrapped in the collapsed gel. Thus, successful utilization of charged hydrogels requires understanding, and control, of the swelling transition mechanism. The relationship between the system pH and the swelling transition of charged hydrogels has been widely examined. They find that swelling in acidic or basic hydrogels (i.e., hydrogels carrying acidic or basic groups) is indeed triggered by pH changes.¹⁶⁻²⁷ As may be expected, the maximal degree of swelling was found to increase with the subchain length (i.e., the length of chains between crosslinks).^{22;26} Less well studied is the effect of salt concentration. One would expect that increasing the salt concentration (at fixed pH), which increases the degree of

electrostatic screening, would lead to a reduction in electrostatic repulsion and, therefore, to gel collapse.

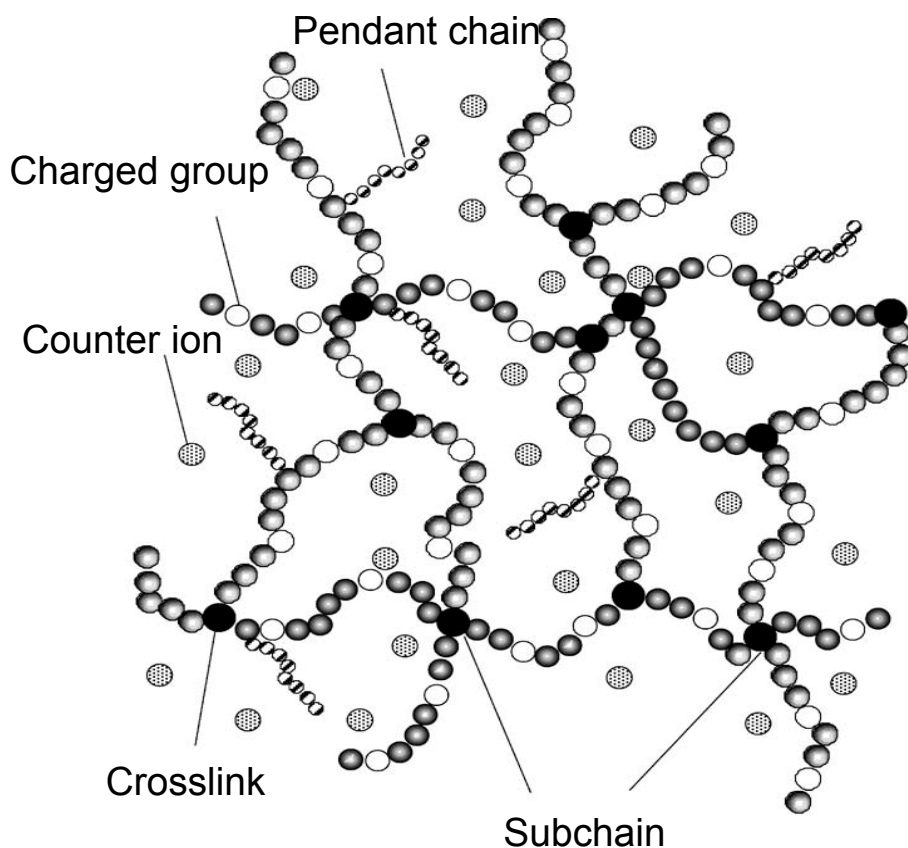


Figure 1.1: a schematic of a charged hydrogel film. The gel is composed of subchains (dark grey) linked through crosslinks (black). Each subchain carries fixed charges (white). However, the charges may be dissociated (active) or undissociated (inactive), depending on the location of their counterions (light grey). The electrostatic repulsion between neighboring fixed charges drives for swelling, while the stretching energy of the subchains between crosslinks favors collapse. The gel may also carry uncharged pendant chains (striped) such as PEG, which do not participate in the electrostatic interactions or in the hydrogel chain elasticity, but do contribute to the overall osmotic force in the system.

Hydrogel swelling equilibrium occurs if the osmotic force driving solvent into the gel is balanced by the elastic force of the stretched subchains. In uncharged systems the osmotic force is set by the chain solubility in the surrounding media. In the charged hydrogel system, the osmotic force driving solvent into the gel is dominated by the electrostatic repulsion between charges.¹⁰ We describe the hydrogel as a penetrable network of fixed, charged groups;^{33;34} Water and small ions (counter ions and additional salt) are free to move in and out of the gel. The fixed charges represent the charges that are attached to the polymer chains, and they are ‘charge regulating’ because their dissociation is subject to electrochemical equilibrium (e.g., acidic groups will dissociate in high pH but remain un-

dissociated in low pH). This system is, in effect, a ‘Donnan system’ since we have here one spatially immobilized charged species and two species of mobile ions.³⁵ A hydrogel sample can be described through several parameters (see Figure 1.1). The gel thickness D ; the average length of a subchain in the gel L ; the salt concentration n and the concentration of H^+ ions H (note that H and n can be set separately in experiments). The type of charged groups is defined through their dissociation equilibrium constant K .^{35;36} The average density of (dissociated) charged groups ρ depends on the total number of charged groups on the polymer chains, the degree of gel swelling and the solution conditions

$$\rho \approx \rho^* (\alpha_0 + \alpha_1 e \beta \psi) \quad \text{--- 1.1}$$

where $\beta=1/kT$, and e the charge of an electron. ρ^* defines the average (nominal) density of charged groups in the system and is given by the number of polymer chains times the number of charged groups per chain divided by the sample volume. The degree of dissociation is related^{35;36} to the pH and type of charged groups through $\alpha_0 = 1/(1+H/K)$ and $\alpha_1 = (H/K)/(1+H/K)^2$ for the anionic $PH \rightleftharpoons P^- + H^+$ type gels we focus on in this study. ψ is the electrostatic potential and is determined by the Poisson–Boltzmann equation. In the Debye-Hueckel limit³³⁻³⁶ the electrostatic driving force for swelling is given by

$$F_{elect} = \frac{1}{4\beta en} \left(\frac{\rho^* \alpha_0}{1 + \rho^* \alpha_1 / 2n} \right)^2 \quad \text{--- 1.2}$$

where F is the force (per unit gel area). Note that the force depends on the size of the sample (i.e. degree of swelling) implicitly through ρ^* which scales as $1/D$ for systems with fixed surface area, or as $1/D^3$ in systems for which swelling is three dimensional. As expected, Eq. 1.2 indicates that the electrostatic force is minimized if $\rho^* \rightarrow 0$ or if $D \rightarrow \infty$. It should be noted that, as in any Donnan system, the electrostatic force is a result of a potential difference between the interior (where there are immobilized charges) and the exterior (where there are only free ions).³⁵

As the gel degree of swelling increases, so does the elastic energy of the subchains. This energy, per subchain, is given in theta conditions as³⁷

$$F_{elas} = \frac{3L}{\beta b l^2} \quad \text{--- 1.3a}$$

For chains in a good solvent this changes slightly to

$$F_{elas} = \frac{3L}{\beta b^{6/5} l^2} \quad \text{--- 1.3b}$$

where L is the end-to-end distance of a subchain, b the subchain molecular weight (inversely proportional to the crosslink density), and l is a step length. As may be expected, the elastic free energy decreases with L . Note that L is proportional to D divided by the number of crosslinks.

Increasing the salt concentration in the hydrogel system increases the degree of electrostatic screening. Therefore one would expect that the electrostatic repulsion between hydrogel charges, which causes swelling, will be mitigated by salt. This trend should be manifested by a monotonic decrease in the degree of swelling (Q), at a fixed pH, as a function of salinity.

At equilibrium, the electrostatic repulsion, or swelling force, between hydrogel charges (Eq. 1.2) is balanced by the elastic restoring force of the stretched polymer chains (Eq. 1.3). Two cases, or system geometries, may be considered: One in which the gel area is fixed so that swelling can occur only in one dimension (the thickness), and one in which the gel area is free to vary so that swelling can occur in three dimensions. In the first case, which applies to surface films of fixed area, the charge density ρ^* decreases inversely with the film thickness D . In the second case (which applies to hydrogel pellets) the charge density ρ^* scales as $1/D^3$.

To demonstrate the effect of system geometry clearly we consider the limit of maximal swelling, which corresponds, in our case of an anionic gel, to the limit where the pH is much higher than the pK of the gel charges (corresponding to $\alpha_0 \approx 1$ and $\alpha_1 \approx 0$). The subscript (1) denotes surface films swelling in one dimension, and (3) denotes pellets that swell in three dimensions

$$D_1^{\max} \approx \left(\frac{\rho_i^2 l^2 b}{n e^2} \right)^{1/3}, \quad Q_1^{\max} \approx A \left(\frac{\rho_i^2 l^2 b}{n e^2} \right)^{1/3}, \quad \text{--- 1.4a}$$

$$D_3^{\max} \approx \left(\frac{\rho_i^2 l^2 b}{n e^2} \right)^{1/7}, \quad Q_3^{\max} \approx A \left(\frac{\rho_i^2 l^2 b}{n e^2} \right)^{3/7}, \quad \text{--- 1.4b}$$

with ρ_i defining the nominal charge density in the collapsed melt hydrogel, given by the hydrogel density in the melt state times the fraction of monomers that carry charges. n is the salt concentration, l is the characteristic polymer persistence length and e is the charge of an electron. b is the subchain molecular weight between crosslinks, and A is the area of the hydrogel in the one dimensional case. D_1^{\max} and Q_1^{\max} define the maximal thickness and degree of swelling in the one-dimensional case for which the gel area is fixed, and D_1^{\max} , Q_1^{\max} defines the thickness and degree of swelling in the case for which the gel swells uniformly.

We see that as may be expected, the maximal degree of swelling increases with the subchain molecular weight and the overall (melt) charge density, and decreases with the salt concentration. Also as expected is the fact that the hydrogel thickness (D) increases more in the onedimensional case, when it can expand only in one direction, than in the three-dimensional case, but the overall degree of swelling (Q) is larger for the three dimensional case.

With respect to the effect of the solution salt concentration on the degree of swelling, a non-monotonic relationship between the strength of electrostatic interactions and salt concentration appeared in weakly charge systems. In the limit of low salt, the range of the electrostatic repulsion is large. Neighboring charges strongly interact, in an unfavorable way. As a result, the degree of charge dissociation decreases leading to a reduction in the number of “active” charges and thus, to gel collapse. As the salinity increases, two opposing trends take place. The degree of charge dissociation increases, thereby increasing the repulsive forces leading to swelling, while the range of the electrostatic interactions and their strength decreases due to salt-induced screening. This competition leads to an initial increase in the electrostatic repulsion (and thus increase in the degree of swelling), reaching a peak where most of the hydrogel charges are dissociated. Above this critical salt concentration the degree of gel charging, or dissociation, remains more or less constant, so that the system is dominated by the increase in charge screening and the hydrogel volume decreases.

The salt concentration at which a hydrogel, at a fixed pH, obtains the maximal degree of swelling is given by

$$n^* \approx \sqrt{\frac{\rho_i e^{pH}}{b} \frac{eK^{3/2}}{l(e^{pH} + K)^2}} \quad \text{--- 1.5}$$

And the degree of swelling at that point is equal to

$$Q(n^*) \approx A \sqrt{\frac{l^2 b \rho_i e^{pH}}{e^2 K}} \quad \text{--- 1.6}$$

We see that the salt concentration at which the maximal degree of swelling occurs increases and then decreases with pH. N^* is approximately zero in the limit of both very low (negative) or very high pH. This is because in either pH limit the equilibrium governing the dissociation of the hydrogel charges is dominated by the concentration of H^+ ions, and is therefore relatively insensitive to the presence of salt. Increasing the salinity in these systems does not affect the degree of dissociation, acting only to monotonically screen the electrostatic repulsion.

The salt concentration at which swelling is maximal is highest if the pH is approximately equal to the pK of the hydrogel charges, since this is the region where the degree of charge dissociation is most sensitive to the system electrochemical potential (ψ). Thus, we expect the degree of swelling of hydrogels at pH values that are either below or above the transition value to vary little with changes in the salt concentration, while gels near the transition value will display great sensitivity to the solution salinity.

In order to determine transition pH from the collapse to swollen, we calculate the pH at which the maximal increase in the gel volume occurs (namely, the pH as the point of inflection where $\partial^2 Q / \partial pH^2 = 0$). We find that, in the limit of high b and n

$$pH^* = -\ln[3K] + \left(\frac{e \rho_i}{l^2 n^2 b} \right)^{1/3} \quad \text{--- 1.7}$$

We see that in the limit of $b \rightarrow \infty$, where we do not expect chain elasticity to play a role, the transition occurs if the concentration of H^+ ions is a function of the equilibrium coefficient only. As may be expected, in this limit the transition depends only on the chemistry of the polymer charges and not on their elasticity. As the subchain molecular weight decreases, the pH necessary to induce the swelling transition increases. This is due to the fact that the degree of charge dissociation increases, in the anionic hydrogels discussed here, with pH. However, the effect of crosslink density may be quite weak, depending on the other parameters in the system. Increasing the salt concentration, in this limit, also leads to a decrease in the transition pH. Note that these predictions are applicable to anionic

hydrogels of the type $\text{PH} \rightleftharpoons \text{P}^+ + \text{H}^+$. In the case of cationic gels ($\text{POH} \rightleftharpoons \text{P}^+ + \text{OH}^-$) the trends will be similar but opposite, namely, the transition pH will decrease with decreasing b and n values.

To estimate the type, or width of the transition we calculate the slope S of the degree of swelling at the transition pH. A high value of the slope indicates a sharp transition that takes place over a small range of pH. A small value of the slope indicates a wide transition occurring over a large pH range. In the limit of high molecular weight between crosslinks

$$S^* = \left(\frac{bl^2 \rho_i^2}{en} \right)^{1/3} \quad \text{--- 1.8}$$

We see that the slope increases with b , the molecular weight between crosslinks, so that in the limit of $b \rightarrow \infty$ the transition becomes infinitely sharp. This is as may be expected, since in the limit of large b the effect of crosslinking becomes negligible, and the system behaves as a solution of weakly charged polymer chains characterized by a specific equilibrium constant K . We also find that the salinity affects the transition type. In low salt solutions the transition will be sharper than in higher salt concentrations.

The investigation of the parameters controlling the swelling transition of charged hydrogels lead to a better understanding of the environmental parameters that trigger and control the hydrogel transition from a collapsed to a swollen state, thereby enabling hydrogel design for biomedical applications ranging from controlled drug delivery to muscle-like actuators.^{11;30-32}

In conclusion,²⁶ the maximal degree of hydrogel swelling increases weakly with the subchain molecular weight, scaling with the subchain length as $b^{1/3}$ for surface films. The maximal degree of swelling also increases with the polymer chain charge density (degree of charging), and decreases with the salt concentration.²⁸ The degree of swelling depends on the gel geometry, and is higher for gels that swell in three dimensions than for hydrogel surface films that can swell only in one dimension. Increasing the solution salt concentration leads to a non-monotonic variation in the degree of swelling Q : first increasing and then decreasing with n . The location of the maximum in Q as a function of n decreases with decreasing pH, as do the overall salt effects. Thus, when the system pH is far from the transition value the degree of gel swelling is nearly independent of the solution salt concentration. However, at pH values that are near the transition salt has a large effect on the degree of swelling, first increasing and then decreasing the gel volume. One would expect that, in the limit

of high salt concentrations, the high degree of screening will eliminate the role of electrostatics in determining the degree of swelling.

Utilization of hydrogels for technological applications requires control over the transition pH (the pH at which the gels undergo a collapsed to swelling transition) and the sharpness of the transition (which determines the sensitivity). In the limit of long subchains the transition pH is set solely by the chemistry of the gel charges, and the transition is quite sharp. In this limit, a small change in the pH leads to a large jump in the hydrogel volume. The transition pH shifts (in the case of anionic gels to lower values and in the case of cationic gels to higher values) with decreasing subchain length, or, when b is fixed, with decreasing salt concentration. The width of the transition increases with decreases chain length between crosslinks and with increasing salinity. However, the effect of all parameters besides the charge type (i.e. pK) is shown-experimentally and theoretically to be relatively weak.

The incorporation of water-soluble uncharged pendent chains increases the driving force for swelling without affecting the subchain elastic restoring force.^{38;39} As a result, the maximal degree of swelling of gels incorporating such pendent chains is much higher than that of standard gels. Moreover, since the pendent chains are uncharged they are insensitive to parameters such as pH or salinity, we expect that the transition pH will shift (to lower values in the case of anionic gels or higher values in cationic ones) with increasing pendent chain concentration.

1.2.2 Colloidal gold nanoparticles

Over the last decade, there has been increased interest in “nanochemistry”. Metal particles are particularly interesting nanoscale systems because of the ease with which they can be synthesized and modified chemically. From the standpoint of understanding their optical and electronic effects, metal nanoparticles also offer an advantage over other systems because their optical (or dielectric) constants resemble those of the bulk metal to exceedingly small dimensions (i.e., <5 nm). Gold nanoparticles are the most stable metal nanoparticles, and they present fascinating aspects such as their assembly of multiple types involving materials science, the behavior of the individual particles, size-related electronic, and optical properties, and their applications to catalysis and biology.

Perhaps the most intriguing observation is that metal particles often exhibit strong plasmon resonance extinction bands in the visible spectrum, and therefore deep colors reminiscent of molecular dyes. These extinction bands occur if the incident photo frequency is resonant with the collective oscillation of the conduction electrons which is known as the localized surface plasmon

resonance (LSPR). LSPR excitation results in wavelength selective absorption with extremely large molar extinction coefficients $\sim 3 \times 10^{11} \text{M}^{-1} \text{cm}^{-1}$,⁴⁰ resonant Rayleigh scattering with an efficiency equivalent to that of 10^6 fluorophores, and the enhanced local electromagnetic fields near the surface of the nanoparticle which are responsible for the intense signals observed in all surface-enhanced spectroscopies. It is well established that the peak extinction wavelength of LSPR spectrum is dependent upon the size, shape, and interparticle spacing of the nanoparticle as well as its dielectric properties and those of the local environment.⁴¹

Recent experimental studies of metal particle optical properties and single-electron-device applications have demonstrated yet another aspect of versatility: since the surface chemistry of nanoscopic metal particles is similar to that of continuous metal surfaces, chemical surface modification (e.g., self-assembled monolayers) is straightforward and allows for particles that are soluble in a variety of media⁴² or possess specific affinities for certain species in solution.⁴³

Recently there has been growing interest in characterizing the optical properties of metal nanoparticles that are made by lithographic methods, such as nanosphere lithography, e-beam lithography, and by other methods that produce well-defined shapes and sizes without aggregation. This has stimulated new interest in the electrodynamics of isolated nanoparticles, but this time specific attention has been directed to nonspherical nanoparticles with structures that are known from AFM or STM measurements. Other complicating factors include the presence of a substrate that supports the particles, a solvent layer on top of the particles, and particles that are sometimes close enough together that their electromagnetic coupling changes the spectra. Although extinction, absorption, and scattering are still the primary optical properties of interest, other spectroscopic techniques are also being brought to bear on these particles, including surface-enhanced Raman spectroscopy (SERS) and a variety of nonlinear scattering measurements [hyper-Rayleigh, hyper-Raman, SHG, etc.]. These techniques are sensitive to the electromagnetic fields at or near the particle surfaces, thus providing new challenges to the development of accurate methods.

Among the diverse and complex optical properties of metallic particles and surfaces, the interactions of fluorophores with metallic particles and surfaces (metals) have been used to obtain increased fluorescence intensities, to develop assays based on fluorescence quenching by gold colloids, and to obtain directional radiation from fluorophores near thin metal films. For metal-enhanced fluorescence it is difficult to predict whether a particular metal structure, such as a colloid, fractal, or continuous surface, will quench or enhance fluorescence. The effects of metals on fluorescence can be explained using a simple concept, based on radiating plasmons (RPs).⁴⁴

According to the RP model, the emission or quenching of a fluorophore near the metal can be predicted from the optical properties of the metal structures as calculated from electrodynamics, Mie theory, and/or Maxwell's equations. For example, according to Mie theory depending on the size and shape of the particle, the extinction of metal colloids can be due to either absorption or scattering. Incident energy is dissipated by absorption. Far-field radiation is created by scattering. Based on our model small colloids are expected to quench fluorescence because absorption is dominant over scattering. Larger colloids are expected to enhance fluorescence because the scattering component is dominant over absorption. For enhanced fluorescence from silver and gold colloids the RP model predicts the need for radii larger than 20 and 40 nm, respectively.⁴⁴ The ability of a metal's surface to absorb or reflect light is due to wavenumber matching requirements at the metal-sample interface. Wavenumber matching considerations can also be used to predict whether fluorophores at a given distance from a continuous planar surface will be emitted or quenched. These considerations suggest that the so called "lossy surface waves" which quench fluorescence are due to induced electron oscillations which cannot radiate to the far-field because wavevector matching is not possible. The energy from the fluorophores thought to be lost by lossy surface waves can be recovered as emission by adjustment of the sample to allow wavevector matching. The RP model provides a rational approach for designing fluorophore-metal configurations with the desired emissive properties and a basis for nanophotonic fluorophore technology.⁴⁴

The use of colloidal particles as versatile and efficient templates for the immobilization of biomolecules has been recognized since the early 1980s.⁴⁵ Examples of colloidal particle-biomolecule conjugates include immunomicrospheres, which can be used to react in a very specific way with antibodies, target cells, or viruses, depending on the type of antigen adsorbed on the microspheres. A number of groups have studied the adsorption of proteins on colloidal particles. In making a shift to nanoscale curved or 3-D surfaces, Caruso et al. have successfully extended the l-b-l technique to the assembly of protein layers on polystyrene (PS) latex particles.⁴⁶ By virtue of the high surface-to-volume ratio exhibited by colloidal particles, their use in the immobilization of enzymes and formation of bioconjugate materials would result in a concentration of the enzymes considerably higher than that afforded by protocols based on immobilization on planar, 2-D surfaces. Schmitt et al.⁴⁷ reported on the formation of a monomolecular layer of bovine serum albumin (BSA) on the surface of PS latex particles while Elgersma et al. have demonstrated the adsorption of BSA on positively and negatively charged polystyrene lattices.⁴⁸

The interaction of colloidal metal particles such as gold and silver with proteins/enzymes as well as the study of the enzymatic activity of the nano-bioconjugates has also received attention. Natan and co-workers have studied cytochrome c: gold colloid conjugates in great detail as regards their stability, protein orientation on the colloidal particle surface as well as possible application in surface enhanced Raman scattering (SERS).^{49;50} Macdonald and Smith have studied the orientation of cytochrome c adsorbed on citrate-reduced silver colloidal particles.⁵¹ Furthermore, single molecule spectroscopy (SMS) of hemoglobin molecules adsorbed on 100 nm sized citrate-reduced silver colloidal particles using SERS has been reported.⁵² In the area of metal nanoparticle-enzyme conjugate materials, Crumbliss, Stonehuerner, and co-workers have studied the formation and enzymatic activity of gold nanoparticles complexed with horseradish peroxidase and xanthine oxidase as well as glucose oxidase and carbonic anhydrase molecules.⁵³ A salient feature of their work is the demonstration that enzyme molecules are bound tightly to gold colloidal particles and retain significant biocatalytic activity in the conjugated form while the enzyme molecules denature on adsorption to planar surfaces of gold.⁵⁴

Conjugates of AuNPs-oligonucleotides are of great current interest because of the potential use of the programmability of DNA base-pairing to organize nanocrystals in space and the multiple ways of providing a signature for the detection of precise DNA sequences. Applications in the fields of biosensors, disease diagnosis, and gene expression are clearly called for. The two groups of Mirkin-Letsinger at Northwestern^{43;55} and Alivisatos-Schultz at Berkeley⁵⁶ have pioneered strategies for the organization of functionalization of AuNPs with oligonucleotides. The former group used DNA as a linker to form macroscopic assemblies consisting in discrete 13-nm-diameter particles. The DNA attached to the nanoparticles retained its ability to hybridize with complementary DNA, and the annealing process was thermally reversible and nondestructive. The reaction was sequence-specific.⁵⁵ The latter group used DNA as a template to prepare nanocrystal molecules consisting of two or three 1.4- nm-diameter particles on a single oligonucleotide strand. DNA-driven assemblies of AuNPs have indeed attracted considerable interest, and a new colorimetric technique based on the sensitivity of the SPB to monitor DNA modification was designed by the Mirkin-Letsinger group.^{43;55;57} In this strategy, AuNPs are used as building blocks, allowing the assembly of alkanethiol-capped oligonucleotides such as single-stranded DNA and complementary linker oligonucleotide (DNA) strands. Aggregation of AuNPs linked by the oligonucleotides provokes a red-to-blue color change (red shift from 520 to 600 nm of the SPB) that is most useful for this DNA-sensing method. The parameters to be controlled are the AuNP composition, the periodicity, and the aggregate thermal

stability. These parameters are organized in order to influence the optical, mechanical, and electrical properties of the AuNPs. In particular, the optical properties due to the SPB of AuNPs led to the development of a highly selective diagnostic method for DNA, based on the distance-related SPB of AuNPs. The effect of the length of the DNA strands that control the interparticle distance was studied, and it was found that the SPB frequency changes are inversely dependent on the oligonucleotide linker length. An interesting result was that the most important parameter that controls the SPB shift of these AuNPs-DNA materials is the aggregate size. This aggregate size is under kinetic control, and it is the growth rate that depends on the linker length. Annealing of the kinetic structures formed at temperatures just below their melting points lead to a SPB shift. This growth, leading to the red shift of the SPB, occurs through an Oswald ripening mechanism whereby larger aggregates grow at the expense of smaller ones. Electrodynamics modeling contributes to show that these SPB shifts are much more consistent with changes in aggregate size than with interparticle distance. Thus, DNA linkers could be more useful as kinetic controllers of aggregate growth than as spacer units, a valuable indication for the development of quantitative assays for DNA.⁵⁸

Another important characteristic of the AuNPbased pair detection is the “melting” transition of the complementary DNA strand. The AuNPs are linked in the presence of the complementary strand. These H-bonded connections of the links are broken at sufficiently high temperatures, which unzips the oligonucleotides, “melting” the DNA and releasing the particles.⁵⁹ Calculations using AuNP polarizabilities determined from Mie theory, an iterative conjugate-gradient solution algorithm, and fast Fourier transform methods for efficient solution of the electrodynamics of interacting AuNP equations show that the UV extinction lowering and the shift and broadening of the SPB of the DNA-linked AuNPs are explained as the collective electromagnetic response of thousands of AuNPs.⁶⁰

DNA-nucleotides and AuNP-DNA nanostructures were analyzed using electrochemical techniques,⁶¹ including scanning electrochemical microscopy.⁶² Imaging of DNA-AuNPs assemblies by TEM, AFM, and near-field scanning optical microscopy was provided.⁶³ Other techniques used were SPB,⁵⁹ luminescence,⁶⁴ Fourier transform infrared and Raman spectroscopy,^{61;65} surface-enhanced Raman spectroscopy,⁶⁶ labeling and scanning force microscopy,⁶⁵ differential light-scattering spectroscopy,⁶⁷ and quartz crystal microbalance (QCM).^{67;68} The latter technique was shown to be especially useful for the design of new DNA sensors^{68;69} involving dendritic amplification of DNA analysis.⁶⁹ Microcantilevers were used to detect DNA strands with a specific sequence using AuNPmodified DNA. This method is analogous to QCM in the vibration-working mode, but it has various advantages over QCM.⁷⁰ When the size of the AuNPs is 50 nm, a sensitivity

of 10^{-15} M for singlebase mutation detection has been achieved with this method.⁷¹ Dry-reagent strip-type biosensors based on AuNP-DNA interaction enabled visual detection within minutes, and quantitative data were obtained by densitometric analysis.⁷² AuNP-streptavidin conjugates covered with 6-ferrocenylhexanethiol were attached onto a biotinylated DNA detection probe of a sandwich DNA complex, and the amplified voltammetric signal was recorded. A detection level down to 2.0 pM for oligonucleotide was obtained.⁷³ Nonspecific binding of biological molecules can be eliminated, however, using ethylene glycol core protection.⁷⁴

1.3 Aim of the Study

There are several challenges in the field of design, assembly, and characterization of supramolecular (bio-) functional interfacial architectures for optical biosensing applications. The first is the development of immobilization technologies for stabilizing biomolecules and tethering them to the surfaces⁷⁵. The usual aim is to produce a thin film of immobilized biologically active material on or near the transducer surface which responds only to the presence of one or a group of materials or substances requiring detection. Since the immobilization technique used to attach the biological material to the sensor surface is crucial to the operational behavior of the biosensor, realistic strategies for the development of immobilization techniques are essential for practically useful biosensors. The second important challenge is to develop a combination of detection techniques that has a substantial potential for highly controlled on-line monitoring of surface-bound enzyme activity. Another important challenge involves a good understanding of how supramolecular architectures behave under external perturbations. The several projects included in this dissertation will touch on all three of these issues. However, for different objects being investigated, the emphasis is not identical.

In Chapter 3, biotin-functionalized β -lactamase was covalently immobilized to the gold surface of a SPR chip through five different types of interfacial architectures, forming a generic biotin-NeutrAvidin binding matrix. Quantitative comparisons were made between different matrices and binding strategies. In addition, surface biocompatibility and feasibility of regeneration were tested. Furthermore, the results obtained by SPR and optical waveguide measurements were quantitatively compared. For all five matrices investigated, real time enzymatic activity assays of β -lactamase were performed by a detection scheme that combines Surface Plasmon Resonance Spectroscopy (SPR) and miniature Fiber Optic Absorbance Spectroscopy (FOAS) to monitor in-situ and quantitatively an

enzymatic model reaction catalyzed by β -lactamase. SPR was used to control the density of the surface-bound enzyme. Nitrocefin as the enzymatic substrate was allowed to react with the immobilized enzyme in the SPR flow cell, and its turnover was detected with the FOAS system acting as the catalytic biosensor. The coupling of the two techniques has a substantial potential for highly controlled on-line monitoring of surface-bound enzyme activity. The FOAS technique may also be easily employed as an add-on device to other types of affinity sensing instruments, an affinity and a catalytic sensor. In the end, the effect of surface immobilization on the catalytic activity of the enzyme is discussed.

It is increasingly accepted to use colloidal gold-oligonucleotide bioconjugate particles as amplification tags in bioassay application. To evaluate the utility of such a method, supramolecular architectures were designed in Chapter 4 using gold particles obtained by organometallic chemical vapor deposition (OMCVD) for surface immobilization of complementary DNA double strands. OMCVD gold particles were prepared with the extinction maximum at around $\lambda = 520\text{-}530$ nm, a surface coverage of 2×10^{17} gold atoms / cm^2 , and a mean lateral size of 12 nm. DNA hybridization between surface-attached oligonucleotide strands and chromophore-labeled target strands from solution were performed based on OMCVD gold particles and planar metal films for comparison. SPFS allows for a very detailed and quantitative evaluation of the kinetics and affinities of the association and dissociation reactions following a simple Langmuir model. The three-dimensional gold particle interfacial architecture with larger aspect ratios provides a faster and more forceful DNA hybridization process of target from solution to the probe immobilized on the surface, which contributes to a higher affinity constant compared to the two-dimensional metal film matrix with smaller aspect ratios. It is shown that a single mismatch of DNA target with probe reduced the equilibrium constant by two orders of magnitude, allowing for an excellent sequence-specific detection of DNA hybridization based on OMCVD gold particles.

In chapter 5, the conformational changes of a commercial carboxymethyl dextran (CMD) substrate induced by pH and ionic strength variations were studied using surface plasmon resonance spectroscopy. In order to better understand the CMD conformational changes corresponding to stimuli variations, a detection method is preferred, providing more information, rather than balancing several factors like conventional SPR. As a result, SPFS served as a more sensitive detection technique for further investigations with the aim of fluorophore labeling of carboxymethyl groups. CMD matrices showed typical pH and ionic strength responses, such as high pH and low ionic strength swelling. Furthermore, the effects of surface charge and crosslink density of CMD on the

extent of stimuli responses were investigated. The swelling/collapse ratio decreased with decreasing carboxyl group surface concentration and increasing crosslink density.

2 Methods and theories

2.1 Surface Plasmon Optics

Surface plasmon resonance (SPR) is an optical detection technology that has been widely used in characterizing interfaces, thin films and in the development of various sensors. It is an electron charge density wave phenomenon that arises on the surface of a metallic film when light is reflected at the film under specific conditions. The resonance is a result of energy and momentum being transformed from incident photons into surface plasmons, and is sensitive to the refractive index of the medium in contact to the metal film. The phenomenon of anomalous diffraction on diffraction gratings due to the excitation of surface plasmon waves was initially described in the beginning of the twentieth century by Wood⁷⁶ although it was the works by Otto,⁷⁷ Kretschmann and Raether,⁷⁸ Agerwal,⁷⁹ and Swalen⁸⁰ that brought understanding and showed the versatility of the technique.

2.1.1 Surface plasmon resonance spectroscopy (SPR)

2.1.1.1 SPR principle

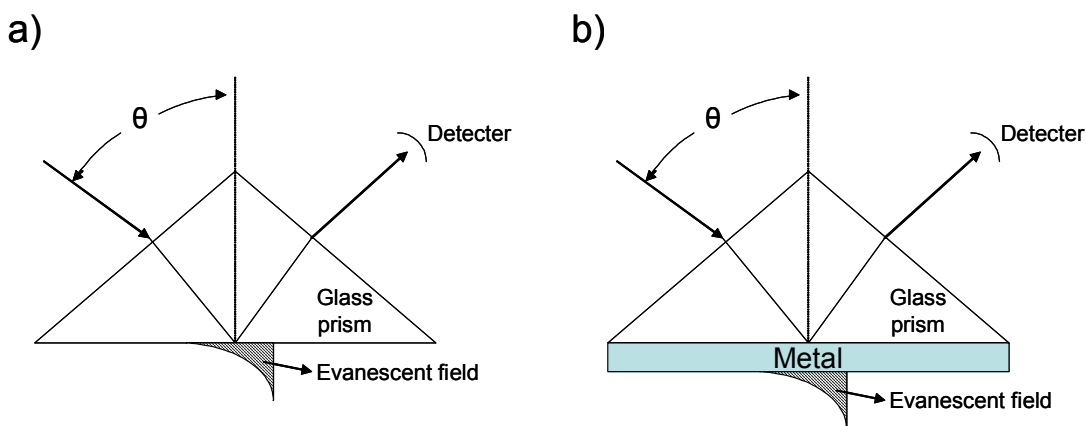


Figure 2.1: Evanescent field excitation using TIR (a) and SPR (b) mode.

Optical characterization of thin films can be carried out by using various configurations of evanescent wave optics. One of the easiest methods of exciting an evanescent wave is by the

total internal reflection (TIR) of a plane electromagnetic light at the base of a glass prism in contact with an optically less dense medium (cf. Figure 2.1a). A light beam (wavelength λ) propagating in a medium with higher refractive index $n_p = \sqrt{\epsilon_p}$, e.g. glass prism, hits an interface at a medium with lower refractive index $n_d = \sqrt{\epsilon_d}$, e.g. water, at an angle of incidence above a critical angle θ_c , is totally reflected at the interface and propagates back into the high refractive index medium. θ_c is given by Snell's law and depends on the refractive indices of the two media.

Although the fully reflected beam does not lose any net energy across the TIR interface, a scrutinization of the optical field near the interface would indicate that above the critical angle, the optical electric field along the propagation direction, E_x , has the oscillatory character of an electromagnetic mode, while the component perpendicular to the interface, E_z , does not fall to zero abruptly, but decays exponentially with a decay length l which is a function of the angle of incidence

$$l = \frac{\lambda}{2\pi\sqrt{(n \cdot \sin \theta)^2 - 1}}, \quad \theta > \theta_c. \quad \text{--- 2.1}$$

This penetration depth is usually of the order of a wavelength of light and this propagating electromagnetic wave is termed an evanescent wave. One way to enhance the evanescent field is by using a metal film in combination with the prism (cf. Figure 2.1 b).

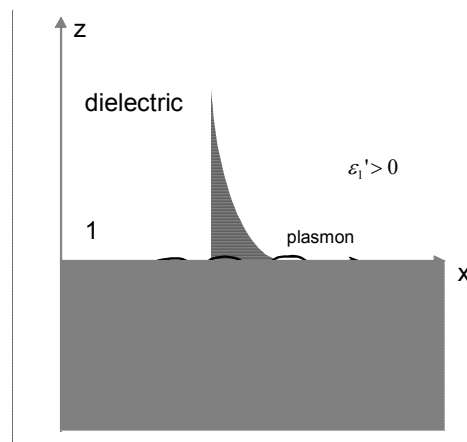


Figure 2.2: Schematic presentation of a surface plasmon at the interface between a metal and a dielectric. Note the sign of the two media need to be opposite to allow for plasmon excitation.

If the TIR interface is coated with a thin noble metal layer so as to provide an optical resonator, one is still dealing with an evanescent wave phenomenon, however, with a few significant differences.

As shown in Figure 2.2, we consider an interface in the xy -plane between two half-infinite spaces, 1 and 2, whose optical properties can be described by their complex dielectric functions $\varepsilon_1 = \varepsilon_1' + i\varepsilon_1''$ and $\varepsilon_2 = \varepsilon_2' + i\varepsilon_2''$, respectively. Ignoring magnetic materials, surface polaritons can only be excited at such an interface if the dielectric displacement \vec{D} of the electromagnetic mode has a component normal to the surface (z -direction) which can induce a surface charge density σ ,

$$(\vec{D}_2 - \vec{D}_1) \cdot \vec{z} = 4\pi\sigma \quad \text{--- 2.2}$$

The electric field of an electromagnetic plane wave can be described in a complex form by the equation:

$$\vec{E} = \vec{E}_0 e^{i(\vec{k} \cdot \vec{r} - \omega t)} \quad \text{--- 2.3}$$

where \vec{E}_0 is the electric field amplitude, \vec{k} is the wavevector pointing into the propagation direction, \vec{r} is the position vector, ω is the angular frequency ($\omega = 2\pi f$) and t is the time. The magnitude of \vec{k} is given by:

$$|k| = \sqrt{\mu\mu_0\varepsilon\varepsilon_0\omega^2} \quad \text{--- 2.4}$$

where μ and μ_0 are the magnetic permeability (dimensionless) and magnetic permeability in free space, respectively, ε and ε_0 are dielectric constant (without dimension) and dielectric constant in free space, respectively.

S-polarized light (transversal electric (TE) waves) propagating along the x -direction possesses only electric field components, $\vec{E}_i = (0, E_y, 0)$, parallel to the surface, and hence are unable to excite surface polaritons. Only p-polarized light (transversal magnetic (TM) waves) modes with $\vec{E}_i = (E_x, 0, E_z)$ or, equivalently, $\vec{H}_i = (0, H_y, 0)$ can couple to such modes. Therefore, the resulting surface electromagnetic wave will have the following form:

$$\begin{aligned}
 \vec{E}_1 &= (E_{x1}, 0, E_{z1}) e^{i(\vec{k}_{x1}\vec{x} + \vec{k}_{z1}\vec{z} - \omega t)} \\
 \vec{H}_1 &= (0, H_{y1}, 0) e^{i(\vec{k}_{x1}\vec{x} + \vec{k}_{z1}\vec{z} - \omega t)} \quad z > 0 \\
 \vec{E}_2 &= (E_{x2}, 0, E_{z2}) e^{i(\vec{k}_{x2}\vec{x} + \vec{k}_{z2}\vec{z} - \omega t)} \\
 \vec{H}_2 &= (0, H_{y2}, 0) e^{i(\vec{k}_{x2}\vec{x} + \vec{k}_{z2}\vec{z} - \omega t)} \quad z < 0
 \end{aligned} \quad \text{--- 2.5}$$

where \vec{k}_{x1} and \vec{k}_{x2} are the wavevectors in x -direction and \vec{k}_{z1} and \vec{k}_{z2} are those in z -direction.

Both fields \vec{E} and \vec{H} must fulfill the Maxwell equations:

$$\begin{aligned}
 \nabla \cdot \vec{H} &= 0 \\
 \nabla \cdot \vec{E} &= 0 \\
 \nabla \times \vec{E} + \frac{1}{c} \frac{\partial \vec{H}}{\partial t} &= 0 \\
 \nabla \times \vec{H} - \frac{\varepsilon}{c} \frac{\partial \vec{E}}{\partial t} &= 0
 \end{aligned} \quad \text{--- 2.6}$$

with c being the speed of light in vacuum. Considering the continuity relations of the in-plane components:

$$\begin{aligned}
 E_{x1} &= E_{x2} \\
 H_{y1} &= H_{y2}
 \end{aligned} \quad \text{--- 2.7}$$

inserting (2.7) into (2.5) yields:

$$k_{x1} = k_{x2} = k_x. \quad \text{--- 2.8}$$

And it follows from Equations (2.5) and (2.6) that

$$\begin{aligned} k_{z1}H_{y1} &= \frac{\omega}{c} \varepsilon_1 E_{x1} \\ k_{z2}H_{y2} &= -\frac{\omega}{c} \varepsilon_2 E_{x2} \end{aligned} \quad \text{--- 2.9}$$

Together with the continuity relations (2.7), this leads to the only nontrivial solution if:

$$\frac{k_{z1}}{\varepsilon_1} + \frac{k_{z2}}{\varepsilon_2} = 0. \quad \text{--- 2.10}$$

This indicates that surface electromagnetic modes can only be excited at interfaces between two media with dielectric constants of opposite sign. As mentioned above, we are dealing here with the interface between a metal ($\varepsilon_2 = \varepsilon_m = \varepsilon_m' + i\varepsilon_m''$) and a dielectric material ($\varepsilon_1 = \varepsilon_d = \varepsilon_d' + i\varepsilon_d''$), and the coupling is essentially the collective plasma oscillations of the nearly free electron gas in a metal to an electromagnetic field. These excitations are called plasmon surface polaritons (PSP) or surface plasmons (SP).

From (2.6) and (2.9), one can obtain:

$$k_x^2 + k_{zd}^2 = \left(\frac{\omega}{c}\right)^2 \varepsilon_d. \quad \text{--- 2.11}$$

Inserting (2.10) into (2.11) leads to the dispersion relationships (i.e. the energy momentum relation) for surface plasmons at a metal/dielectric interface:

$$k_x = \frac{\omega}{c} \sqrt{\frac{\varepsilon_m \cdot \varepsilon_d}{(\varepsilon_m + \varepsilon_d)}}. \quad \text{--- 2.12}$$

In the usual treatment, ω is taken to be real. Since ε_m is complex, k_x is also complex. Therefore, the amplitude of the electric field decays exponentially into both media in z -direction as well as into the propagation direction. The penetration depth of the evanescent field wave, l_c , is usually defined as the distance over which the wave decays to $1/e$, or about 37%, of its maximum

intensity. For $\lambda = 632.8 \text{ nm}$ light at gold/water interface, L_x is $\sim 27 \text{ nm}$ at the gold side, and $\sim 242 \text{ nm}$ at the water side. The propagation length, L_x , can be calculated by $L_x = 1/2k_x''$. For $\lambda = 632.8 \text{ nm}$ light at gold/air interface, $L_x = 10 \mu\text{m}$, while the length becomes $4 \mu\text{m}$ at gold/water interface. This decay has a strong impact on lateral resolution of methods like surface plasmon microscopy. The damping of the electromagnetic field will cause heat, dissipating into the metal and the dielectric.

2.1.1.2 Surface Plasmon Spectroscopy with Prism Coupling

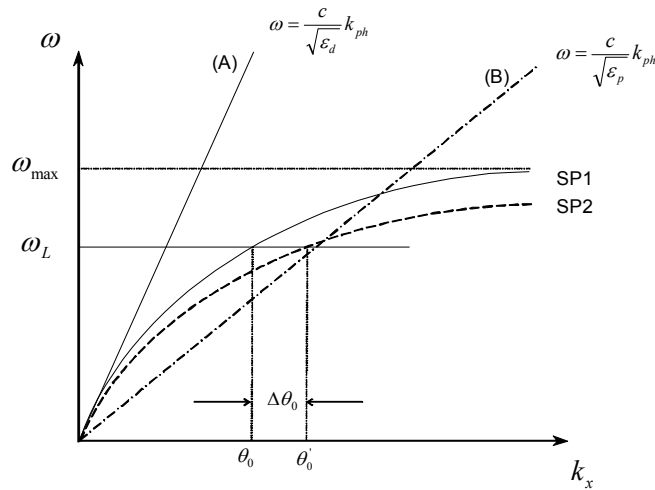


Figure 2.3: The dispersion relation of free photos in a dielectric (A), and in a coupling prism (B), compared to the dispersion relation for non-radiative surface plasmons at the metal/dielectric interface before (SP1) and after (SP2) the adsorption of an additional dielectric layer.

In the frequency (spectral) range of interest we have:

$$\sqrt{\frac{\epsilon_m \cdot \epsilon_d}{(\epsilon_m + \epsilon_d)}} \geq \sqrt{\epsilon_d} \cdot \tag{--- 2.13}$$

This leads to the consequence that the momentum of a free photon propagating in a dielectric medium (line (A) in Figure 2.3),

$$k_{ph} = \frac{\omega}{c} \sqrt{\epsilon_d} , \quad \text{--- 2.14}$$

is always smaller than the momentum of a surface plasmon mode (curve SP1 in Figure 2.3), propagating along an interface between that same medium and the metal. Thus, it tells us that in addition to the energy conservation, this is not sufficient to fulfill the momentum matching condition for resonant SP excitation because, for very low energies, the SP dispersion curve asymptotically reaches the line (A), whereas for higher energies it approaches the cutoff angular frequency ω_{max} determined by the plasma frequency of the employed metal, ω_p :

$$\omega_{max} = \omega_p / \sqrt{1 + \epsilon_d} . \quad \text{--- 2.15}$$

It is therefore important to note, that surface plasmons are not directly excited by light in vacuum, unless the wavevector of the free photos, is increased by passing the photos through a medium with higher refractive index than the dielectric, or adding a grating vector through the periodically corrugated surface structure to match the plasmon wavevector at the interface. Experimentally, the former can be achieved by reflecting the incident light on the base plate of a high refractive index prism, namely, the prism coupling, and the latter can be realized by the grating coupling.

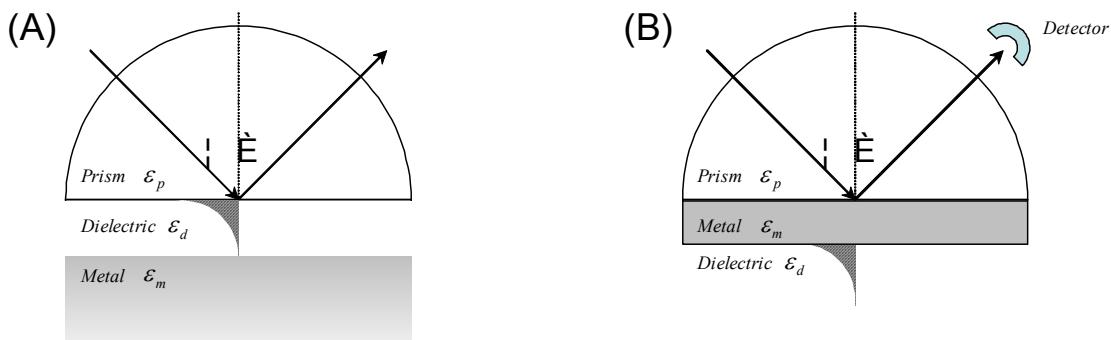


Figure 2.4: Prism coupling geometries for Otto configuration (A) and Kretschmann-Raether configuration (B). Coupling is only possible when the refractive index of the prism is higher than that of the dielectric.

By far, the prism coupling is the most predominant coupling techniques for increasing the wavevector of the incident light, k_{ph} , and also the main technique which will be discussed in our

research. Various shapes of prisms can be used for exciting PSP, such as triangular prisms, half cylindrical prisms, hemispherical prisms. For simplicity, we will use half cylindrical prisms in the discussion of this chapter, to avoid considering of angle conversion by refraction at the air/prism interface.

In the prism coupling, the light travels through the high refractive index prism ($\varepsilon_p > \varepsilon_d$), characterized by a larger momentum of $k_{ph} = \frac{\omega}{c} \sqrt{\varepsilon_p}$, which for a certain spectral range can exceed the momentum of the SP to be excited on the metal surface (cf. line (B) in Figure 2.3). For the excitation of surface plasmons, only the photo wavevector projection to the x -direction is the relevant parameter. Hence, resonant coupling between the incident photons and surface plasmons can be obtained by choosing the appropriate angle of incidence θ_0 ,

$$k_{ph} \sin \theta_0 = \frac{\omega_L}{c} \sin \theta_0 \sqrt{\varepsilon_p} = k_{sp} = k_x = \frac{\omega_L}{c} \sqrt{\frac{\varepsilon_m \cdot \varepsilon_d}{(\varepsilon_m + \varepsilon_d)}} \quad \text{--- 2.16}$$

$$\theta_0 = \arcsin \sqrt{\frac{\varepsilon_m \cdot \varepsilon_d}{(\varepsilon_m + \varepsilon_d) \cdot \varepsilon_p}}$$

Two prism coupling geometries are schematically shown in Figure 2.4, which are called Otto configuration and Kretschmann-Raether configuration, respectively.⁸¹ In the case of the Otto configuration (cf. Figure 2.4 (A)), the evanescent field bridges a 200 nm wide air gap between the prism and the metal, and the plasmons are excited at the metal/air interface.⁷⁷ Since this configuration is experimentally challenging, it has not gained any practical importance.⁸² The Kretschmann-Raether configuration (cf. Figure 2.4 (B)) is more versatile because it is much easier to realize.⁷⁸ In this most widespread version of surface plasmon spectroscopy, the photos in the prism couple through a very thin metal layer to the PSP states at the other side in contact with the dielectric medium. The thickness of the metal film influences the coupling angle, θ_0 , as well as the coupling efficiency, *e.g.* the minimum reflectivity. This dependence can be simulated by Fresnel's equations using the transfer matrix methods. For the excitation by $\lambda = 632.8$ nm He-Ne laser light, an optimal thickness is in the range of 47 nm for gold with dielectric function $\varepsilon_m = -12.3 + 1.29i$.

2.1.1.3 SPR Response to a Thin Film Deposition

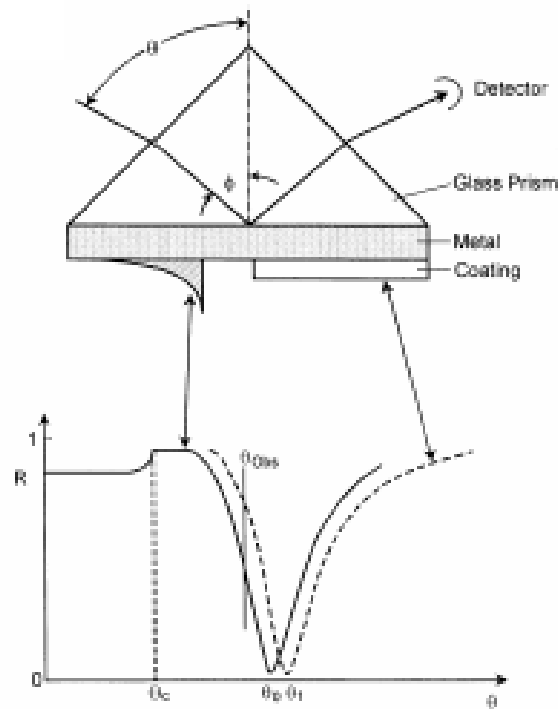


Figure 2.5: Typical surface plasmon resonance curves of the prism/gold/water system before (solid line) and after (dot line) the deposition of an ultrathin layer onto the gold.

If one makes the experiment by recording the reflected intensity, *e.g.* with a diode detector (cf. Figure 2.4 (B)), as a function of the angle of incidence, θ , a typical SPR angular-dependent reflectivity scan curve will be produced and the critical angle for TIR, θ_c , as well as the appropriate angle for the resonance minimum, θ_0 , can be observed. Such a typical resonance curve of the prism/gold/water system is shown in Figure 2.5 in solid line.

Since the evanescent field of the surface plasmons decays exponentially into the dielectric medium, changes of the optical properties of the adjacent dielectric will alter the excitation conditions for plasmons. If an ultrathin and non-adsorbing layer with different dielectric constant ($\epsilon_f \neq \epsilon_d$) is deposited onto the metal layer, it will induce a change on the overall dielectric function integrated over the range of the evanescent field, thus shifts the SPR resonance minimum angle. This can be directly inferred from (2.16), where the new dielectric

function ε_d' is larger than the original one, ε_d , which results in a higher resonance minimum angle, θ_0' .

Similarly, k_{sp} in the surface plasmon dispersion equation (2.12) shifts to a larger wavevector, depicted as curve SP2 in Figure 2.3. This can be expressed mathematically by:

$$k_{sp2} = k_{sp1} + \Delta k \quad \text{--- 2.17}$$

where k_{sp1} and k_{sp2} are the surface plasmon wavevectors before and after the adsorption. It is important to note that the increment Δk depends strongly on the refractive index and the thickness of the adsorbed layer. At a given frequency ω_L , the intersection with the dispersion relation of the photons is therefore shifted towards a higher k value. As a consequence, the angle of incidence that determines the photon wavevector projection along the SP propagation direction has to be slightly increased to fulfill the resonance criterion (cf. Figure 2.3, from θ_0 to θ_0'). This is also experimentally shown in Figure 2.5 where the angular scan curve is shifted from the left (solid line) to the right (dotted line).

In conclusion, in the case of the adsorption of an ultrathin, non-adsorbing layer defined by a thickness d and a refractive index n , the resonance angle displacement $\Delta\theta$ is proportional to the optical thickness d of the layer:

$$\Delta\theta \propto n \cdot d \quad \text{--- 2.18}$$

If the refractive index of the material is known, the geometrical thickness can be determined, and vice versa. This characteristic resonance minimum shift is one of the most fundamental and significant features for the practical application in methods like surface plasmon spectroscopy or microscopy.

On the other hand, for the surface mass change resulting from the protein immobilization, through the calibration between the reflectivity responses measured by our home-made setup and Biacore, Yu⁸³ deduced an empirical equation for the calculation of the surface protein concentration A by the angle of resonance minimum shift $\Delta\theta$:

$$A = \frac{\Delta\theta}{0.19^\circ} (ng \cdot mm^{-2}). \quad \text{--- 2.19}$$

A number of practical experimental conditions, such as metal film thickness and incident wavelength, must be considered when designing an SPR experiment for optimal sensitivity. 47-nm-thick gold film is the optimal substrate for sensing applications (largest signal difference). In the optimal (47 nm) film, a portion of the incident radiation reflects from the glass/Au interface, while a portion propagates through the film to the Au/sample interface and excites surface plasmons, which in turn radiate back into the metal film. The back-scattered radiation is then out of phase with the incident radiation, thereby resulting in a destructive interference process and, hence, a decrease in reflectance. For the thicker Au film, much of the wave propagating into the metal has decayed before reaching the Au/sample surface, resulting in a decrease in the magnitude of the back-reflected plasmon radiation. Conversely, the thin film displays a back-reflected field that is much greater in magnitude and therefore increases the reflectance of the ATR device near the plasmon angle.

Because the optical constants for thin metal films are varying functions of the incident wavelength, the photon energy can be used to change the shape and position of the SPR curve. SPR curve becomes sharper at longer wavelength, reflecting a decrease in the amount of damping experienced by the surface mode. Quantitatively, this damping is related to the mean-free path of electrons at the incident frequency and is therefore related to the decay length of plasmons at the Au/sample interface:

$$I(x) = \exp(-2k_x''x) \quad \text{--- 2.20}$$

in which the imaginary portion of the plasmon wavevector is

$$K_x'' = \frac{\omega}{c} \left(\frac{\epsilon_m' \epsilon_s}{\epsilon_m' + \epsilon_s} \right)^{3/2} \frac{\epsilon_m''}{2(\epsilon_m')^2} \quad \text{--- 2.21}$$

Equation (2.21) assumes that the real (‘) and imaginary (‘’) portions of the metal dielectric function are frequency dependent. From these equations, it follows that decreases in the optical

frequency will result in less plasmon damping and, hence, longer-range propagation of the plasmon mode (i.e. Eq. (2.20) decays more slowly). This effect has been exploited by Corn's group, where IR-excited plasmons are used to obtain higher SPR sensitivity.^{84,85}

Taken alone, the above discussion of the surface plasmon effect suggests the numerous advantages of the technique with respect to biomolecular interaction analysis. This technique is tagless; no enzyme, fluorophore, or radioisotope labeling is required for detection or amplification of a binding event. SPR can also be performed in real time, thereby allowing for kinetic as well as thermodynamic parameters to be determined. Finally, the technique is noninvasive due to a "back-side" illumination geometry is employed; the source beam does not have to travel through the sample solution during operation. This decreases any interference that could arise from turbid or strongly absorbing solutions. (Despite these advantages, it is still desirable in some applications to utilize "tagging" to either amplify or differentiate observables in the SPR experiment.)

2.1.2 Surface Plasmon Field-Enhanced Fluorescence Spectroscopy (SPFS)

Surface plasmon spectroscopy has matured into a well-accepted analytical tool for the characterization of interfaces and thin films as well as for the sensitive detection of kinetic processes, e.g. for monitoring interfacial binding reactions.^{86,87} With a lower limit for a reliable signal detection corresponding to an effective layer of about 0.1-0.2 nm, SPR has generated a sufficient signal-to-noise level allowing for a detailed kinetic analysis and determination of binding kinetics.⁸⁸ However, problems arise if only a very dilute lateral packing of the proteins can be achieved or if very small analytes of low molecular weight are to be detected, resulting in angular shifts too low to be observed.⁸⁹ Therefore, the concept of SPFS combining surface plasmon spectroscopy with fluorescence label techniques is developed to enhance the signal response of the interfacial binding events.

2.1.2.1 Field Enhancement

A quantitative description is possible for layered architectures at an interface solid/liquid with a theoretical treatment that goes back to Fresnel and models the optical response of a layered architecture by solving Maxwell's equations. Each layer is described by its complex

dielectric function with a real and an imaginary part (for absorbing materials) and the layer thicknesses. This treatment allows one to calculate all quantities of interest, e.g. transmitted and reflected intensities (for each interface, but also for the complete multilayer sandwich), the (local) field intensities, hence the state of polarization, the phases (differences) of the various partial waves, etc. The pure dielectric case, in which a plane wave from a laser light source impinges upon the interface between a transparent solid and a liquid, e.g. glass/aqueous medium, is schematically sketched in Figure 2.6 (a). If we monitor the reflectivity, R , i.e. the reflected light intensity I_r , scaled to the incoming intensity, $I_0:R = I_r:I_0$, as a function of the angle of incidence θ (relative to the normal of the interface) we observe the well-known behavior of the total internal reflection: Below a certain critical angle θ_c which is given by Snellius' law, i.e. by the refractive indices of the solid and the liquid, respectively, most of the light is transmitted and hence the reflectivity is very low. As we approach θ_c , however, the reflectivity steeply increases and reaches unity above θ_c . If we calculate the light intensity at the interface, I_s , and scale it to I_0 we find a moderate enhancement of a factor of 4 right at θ_c which originates from the constructive interference of the two amplitudes of the incoming and reflected electromagnetic field at θ_c . This enhancement together with the evanescent character of this surface light at $\theta > \theta_c$ triggered its successful use in surface-selective fluorescence spectroscopies.⁹⁰

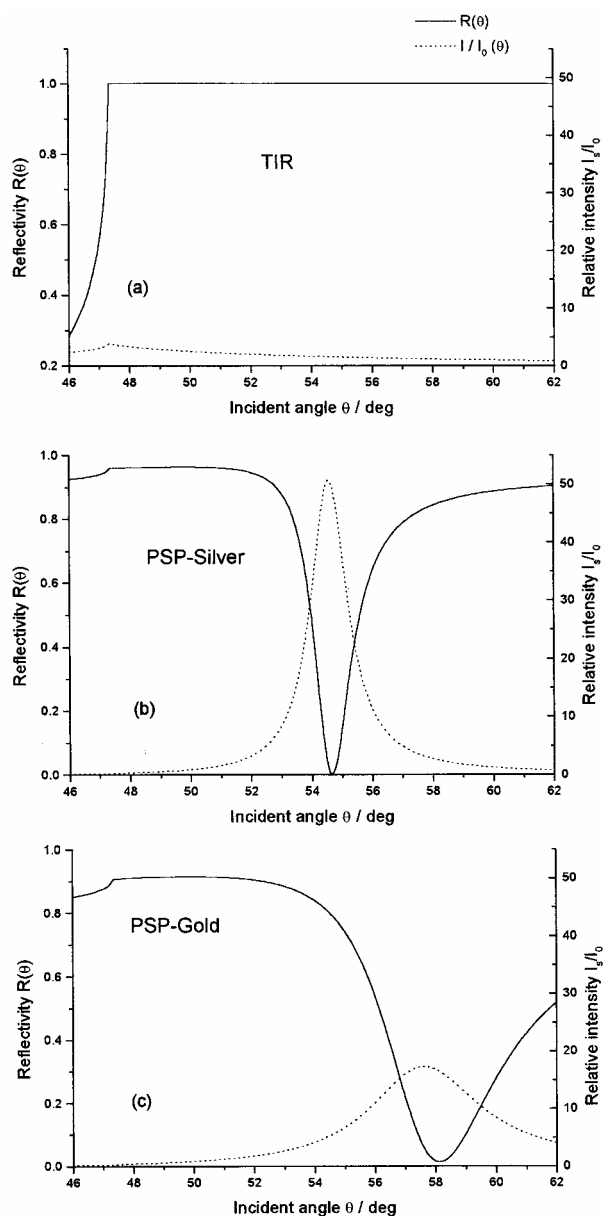


Figure 2.6: Reflectivity R and the relative intensity $I_s:I_0$, i.e. the optical intensity at the surface, I_s , scaled to the incoming intensity, I_0 , as a function of the angle of incidence, u , for a mere total internal reflection (TIR) geometry, i.e. for a glass:water-interface (a), or for plasmon surface polariton excitation at a silver:water-interface (b), or a Au:water-interface (c). Note the different intensity enhancements for the three situations.

If the prism base is covered with a thin (noble) metal layer (cf. also Fig. 6 (a)) so as to provide an optical resonator, i.e. the nearly free electron gas in the metal that can be driven by the incoming photon field,⁹¹ we still are dealing with an evanescent wave phenomenon,

however, with a few significant differences (cf. Figure 2.6 (b) and (c)). Below θ_c , the reflectivity is already rather high because the evaporated metal layer acts as a mirror that reflects most of the otherwise transmitted light. θ_c can still be identified at the original position (depending only on the (accurately known) refractive index of the prism and the bulk dielectric, respectively, and hence in practice allows for an angular calibration of the experimental set-up). Slightly above θ_c , however, the resonant excitation of a plasmon surface polariton (PSP or surface plasmon for short) can be seen in the reflectivity curve as a narrow dip with a minimum intensity that can reach virtually zero reflectivity and shows a half width that depends on the damping of the excited mode which is dominated by the losses in the metal described by the imaginary part of its dielectric function.⁹² What is particularly relevant in the context of fluorescence spectroscopy is the substantial field enhancement that can be found near the minimum of the reflected intensity. As calculated by Fresnel's theory and shown in Figure 2.6 (b) and (c), respectively, the surface light intensity at the metal/dielectric interface increases strongly as one approaches the resonance condition for the excitation of a surface plasmon, reaches a maximum at a characteristic angle and decays again as one increases the angle of excitation further. Peak intensities scaled again to the incoming intensity can reach an enhancement factor of ca. 50 for Ag (cf. Figure 2.6 (b)) and 16 for Au (Figure 2.6(c)). The exact values depend on the actual real and imaginary parts of the dielectric functions of the metals and can vary from sample to sample. But, generally, however, the smaller ϵ'' , i.e. the lower the absorption and hence dissipation of the optical field intensity, the higher the enhancement factor. The smaller ϵ'' of Ag as compared to Au also manifests itself in a narrower resonance for Ag, with a half-width (@ $\lambda=633$ nm) of $\Delta\theta \approx 0.5^\circ$, as compared to Au with $\Delta\theta \approx 2-3^\circ$. This field enhancement phenomenon is well known and widely applied in other spectroscopy technologies, *e.g.* surface-enhanced Raman scattering (SERS)⁹³.

The peak intensity is found at a slightly lower angle of incidence than the minimum in the reflectivity. The reason again is related to the resonance character of the PSP excitation: as one sweeps through the resonance the phase difference of the surface mode relative to the driving photon field changes as for any other resonator: for a fictive loss-free metal the phase would change from 0° below the resonance to 180° above it, with a sharp step at the resonance. Any damping (loss) in the system broadens and smears this phase change. Since we are observing in reflection a coherent superposition of a partial wave directly reflected from the metal/prism

interface with (a fraction of) the surface mode re-radiated via the prism, the minimum in the total reflection then is the destructive interference of the two partial waves differing in phase by 180° which is reached just above the angle of maximum surface plasmon intensity. Again, the higher the loss of metal ($\epsilon''_{\text{Au}} > \epsilon''_{\text{Ag}}$) the more smeared-out is the phase change of the PSP resonance and hence the larger the difference in the angular position of the surface mode peak intensity and the reflectivity minimum (cf. Figure 2.6 (b) for Ag and (c) for Au).

2.1.2.2 Fluorescence at the Metal/Dielectric Interface

As mentioned above, in the case of total internal reflection, only a moderate field enhancement by a factor of 4 is obtained at the critical angle due to constructive interference between the incoming and reflected electromagnetic field. This enhancement together with the evanescent character of this surface light triggered its successful use in total internal reflection fluorescence (TIRF)⁹⁰. The electromagnetic field enhancement of SPR is more substantial than that of TIR, as a consequence, much stronger fluorescence emission should be obtained if the fluorophores are excited by surface plasmon evanescent wave.

As discussed in Section 2.1.1.2, the evanescent field decays exponentially into the dielectric layer adjacent to the metal film with the characteristic parameter, the penetration depth, at which the surface field intensity drops down to $1/e$ of the interface value, typically several hundred nanometers into the dielectric medium. Therefore, surface plasmon sensitive fluorescence measurements will only be possible if the dyes are in close proximity to the metal film.

However, the electronic coupling of the molecular orbitals localized in the chromophore with the extended band structure of the metallic electrons in the solid substrate generates new decay channels for the excitation energy of the dye, leading to a strong modification of radiative lifetimes and fluorescence intensities as the fluorophores are coming closer and closer to the metal surface.⁹⁴ Figure 2.7 summarizes some of the observed distance-dependent energy transfer mechanisms.

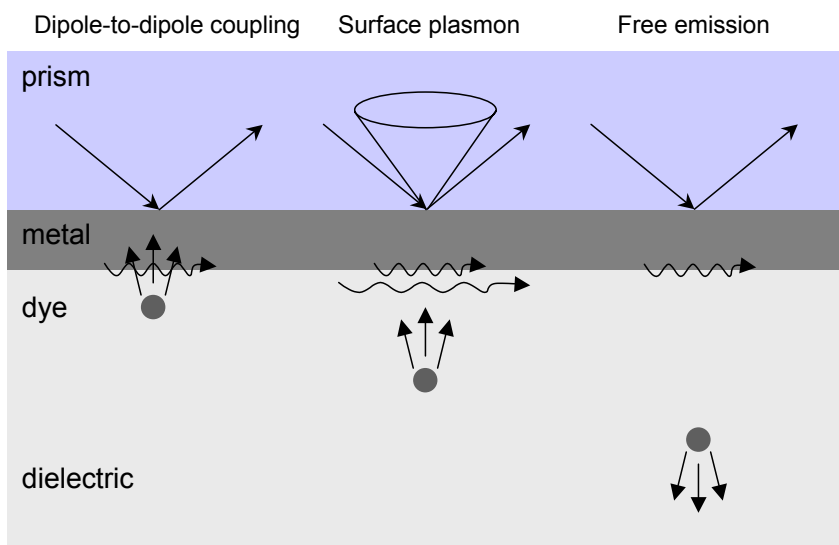


Figure 2.7: Schematic of the different electronic coupling regimes for a fluorophore in water at different distances to a metal film surface.

If a dye is positioned at a distance within 10 nm to the metal surface, a substantial ‘radiation-less’ de-excitation with a corresponding reduction of the radiative lifetime and the fluorescence intensity is found. The fluorescence is ‘quenched’, dissipating the excitation energy in the metal as heat. This quenching phenomenon can be modeled by the Förster resonance energy transfer, showing a R^{-6} dependence of the transfer efficiency to the separation distance. However, integrating over all possible sites of an entire surface of acceptors will yield a R^{-4} dependence (cf. dashed curve in Figure 2.8).

At an intermediate-distance regime (a few nm up to ~ 20 nm), the optically excited chromophores can effectively couple back to the plasmonic states of the metal substrate. Since some of the excitation energy is dissipated in the dye molecule via vibronic excitation, the corresponding back-coupled surface plasmon mode is red-shifted relative to the excitation and hence re-radiates in a cone via the prism at a slightly smaller angle.

At sufficient separation distances (>20 nm), free emission of the fluorophores can be achieved. The fluorescence intensity only depends on the intensity of the evanescent field except for some (negligible) interference effects between the radiation field directly emitted and the one reflected from the metallic surface.

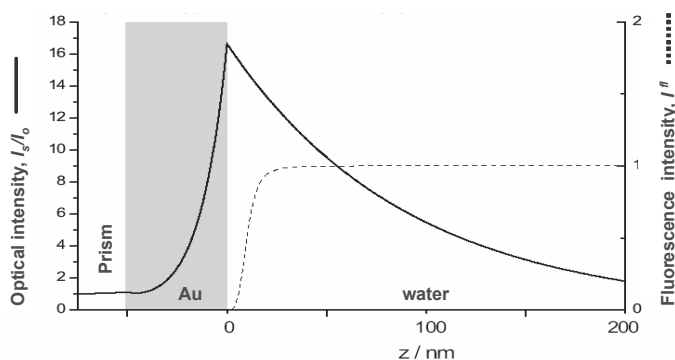


Figure 2.8: Comparative presentation of the distance dependence of the optical field enhancement of a surface plasmon evanescent wave mode excited at a prism/Au/water interface (solid curve), and the Förster energy transfer mechanism, expressed as the relative fluorescence intensity (dashed curve) placed at a certain distance above the metal/water interface.

Figure 2.8 summarizes these findings in their consequence for the design of an interfacial architecture optimized for maximum sensitivity enhancement by combining the spatial characteristics of surface plasmon fields and the quantum efficiency for radiative dipoles near a metal surface. In contrast to the quenching processes that only occur for chromophores within 10-15 nm of the surface, the exponential decay of the surface plasmon field ranges on a much longer distance of several hundred nanometers. This means that fluorescent species placed at least 1 Förster distance (typically 5-7 nm) away from the surface experience a loss in the fluorescence intensity of a factor of 2 at most. They are still in the largely enhanced optical field of a resonantly excited surface plasmon mode used for chromophore excitation. Therefore, by carefully designing the supramolecular interfacial layers providing the binding sites for the recognition process of fluorescently labeled analyte, one can gain enormously in detection sensitivity by exploiting the enhanced surface plasmon optical field without being compromised by the quenching mechanism.

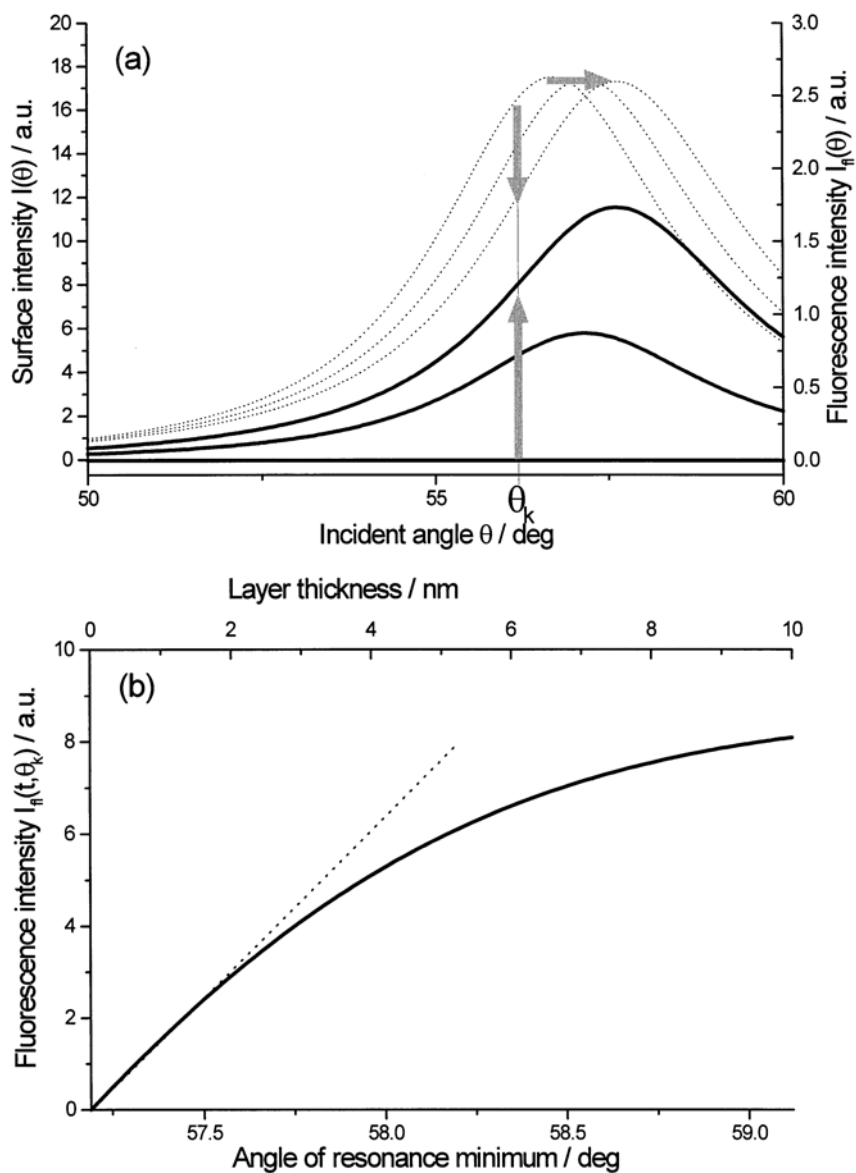


Figure 2.9: (a) Surface intensity (dotted curves) and resulting fluorescence intensity (full curve) for a bare Au:water interface, and with a thin dielectric coating of 2.5 or 5 nm, respectively, doped with a fictive fluorescent dye system. The corresponding shift of the PSP resonance angle results, at a fixed angle of observation, e.g. at θ_k , in a less than linear increase of the fluorescence intensity (cf. the different shaded arrows). (b) Simulation of the deviation of a linear fluorescence intensity increase from an increase in layer thickness, equivalent to a shift of the resonance angle for PSP excitation. Note that only for very thin layers, i.e. for ≤ 2 nm, a linear approximation holds.

The next point that is relevant and hence has to be taken into account for a quantitative understanding of kinetic (association/dissociation) fluorescence measurements concerns a situation where the fluorophore is coupled to a molecular unit, the molecular mass of which is

large enough so as to induce upon binding an angular shift of the surface plasmon resonance angle. Such kinetic runs are typically recorded by monitoring the reflected intensity at a fixed angle of observation. As long as only small thickness changes are obtained by the binding of the analyte one can select this angle of observation within the approximately constant slope at the low-angle side of the PSP resonance dip thus guaranteeing a linear relation between the observed intensity change and the angular resonance shift (which, in turn, is a linear function of the adsorbed mass per unit area for small thickness changes). If the enhanced optical field of a surface plasmon at or near resonance is used to excite the fluorophores of an adsorbed analyte molecule, this shift, however, influences the degree of coupling and hence the illumination intensity at a fixed angle of incidence. This is schematically depicted in Figure 2.9, which shows simulated angular spectra of the PSP optical intensity for a bare Au/H₂O interface, as well as, after deposition of 2.5 and 5 nm of coating material (@ $n=1.5$), respectively. If the latter contains fluorophores, their emission intensity is assumed to scale linearly with the respective thickness, and, of course, shows the corresponding angular dependence (cf. Figure 2.9 (a), thick curves). As can be seen directly, the fluorescence intensity at a fixed angle of observation does not scale linearly with the thickness of the adsorbed layer even in the absence of any Förster energy transfer effects which might-thickness dependent-complicate the experimental situation even further. The deviation from linearity can be seen in Figure 2.9 (b) in which the fluorescence intensity is plotted as a function of the film thickness or, equivalently, as a function of the correspondingly shifting resonance angle. The effect can be ignored only for adsorbed layer thickness smaller than ca. 1–2 nm. Above this limit, however, the deviations are quite substantial and need to be taken into account.

2.1.3 Home-Made SPFS Setup

The surface plasmon field-enhanced fluorescence spectroscopy (SPFS) setup used for the described study was based on a conventional Kretschmann configuration, which is also the most widely used geometry in SPR sensors.⁹⁵ The schematic description of the setup is depicted in Figure 2.10.

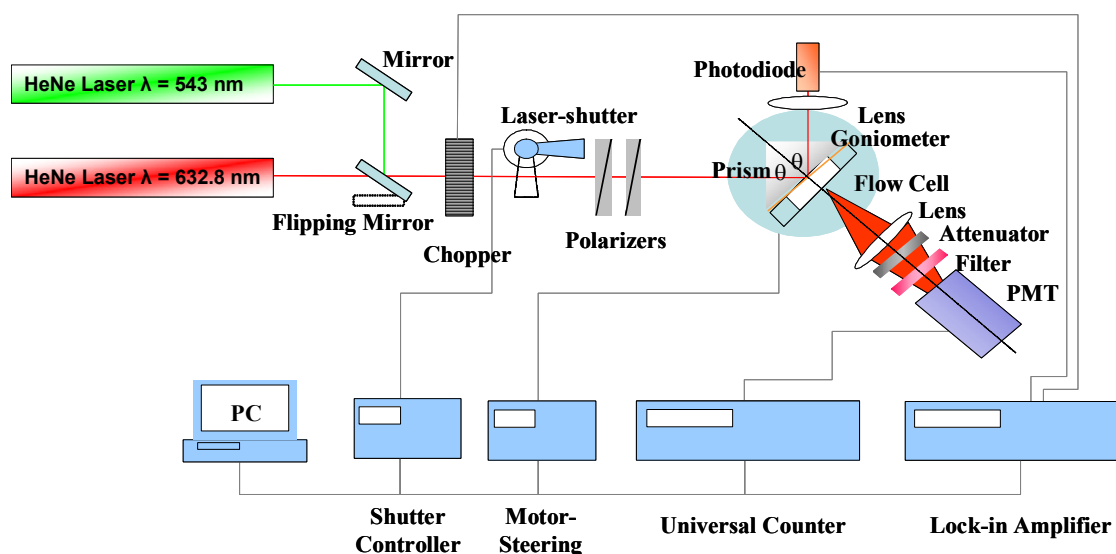


Figure 2.10: Schematic of a surface plasmon field-enhanced fluorescence spectroscopy setup with two separate excitation laser sources.

In this setup, surface plasmons can be excited by two different lasers, which are both Helium-Neon (HeNe) lasers with the incident wavelength $\lambda = 632.8$ nm and $\lambda = 543$ nm, respectively. A manually controlled flipping mirror (Owis) is utilized to select between the two lasers. The continuous laser beam passes through a chopper (Perkin Elmer, frequency = 1331 Hz) connected to a lock-in amplifier (Perkin Elmer). A PC-controlled shutter is also mounted in the optical path in order to minimize the photobleaching of the fluorophores. Two polarizers (Glan-Thompson) are used next, adjusting the plane of polarization and the intensity of the laser. Finally, the laser beam enters a right angle coupling prism (Schott, LASFN9, $n = 1.85$ @ $\lambda = 632.8$ nm) and is reflected off the metal/dielectric interface, focused by a convex lens (Owis, $f = 50$ mm) onto a photodiode detector which is connected to the same lock-in amplifier as the chopper. The prism/sample unit and the photodiode detecting unit are mounted on two-axial goniometers (Huber) with the precision of 0.001° rotational movements, enabling an independent tuning of respective angular positions. Normally, the former unit rotates at θ , while the latter unit rotates at 2θ , relative to the fixed excitation laser beam, in the surface plasmon resonance scan measurements.

The fluorescence detection module is mounted along the normal direction of the metal-dielectric interface, rotating together with the prism/sample unit. In a general surface plasmon field-enhanced fluorescence mode, the fluorescence emission emitted normal to the meta/dielectric base plane is collected by a focusing lens (Owis, $f = 50$ mm) and passes through an interference filter [LOT, $\lambda = 671$ nm, transmittance = 60%, especially for Cy5 (Cyanine 5, from MWG GmbH) or Alexa Fluor 647 (from Molecular Probes Inc.) excitation, and $\lambda = 620$ nm or 560 nm, transmittance = 50%, for Cy3 (Cyanine 3, from MWG GmbH) excitation, with $\Delta\lambda = 10$ nm for both cases] to block the scattered and out-coupled excitation light, before it's finally gathered by a photomultiplier tube (PMT, Hamamatsu), which is connected to a universal counter (Agilent) via a home-made electronic interface to convert analog to digital data, expressed in counts per second (cps). In the case where the fluorescence light intensity is beyond the PMT's linear input-versus-output range ($< 2.5 \times 10^6$ cps), an appropriate attenuator (neutral filter, LOT) is added to weaken the intensity according to its attenuation factor.

Two modes of operation are possible: an angular scan mode in a θ - 2θ reflection geometry, or a kinetics mode in order to resolve time-dependent processes at a fixed angle of observation. For both modes, the reflectivity channel as well as the fluorescence intensity channel can be recorded simultaneously. Data acquisition and electronics control are accomplished by custom programs.

2.2 Enzymatic activity assay

2.2.1 Properties and classification of enzymes

Enzymes are biological catalysts. They enhance reaction rates because they provide an alternative reaction pathway that requires less energy than an uncatalyzed reaction. In contrast to some inorganic catalysts, most enzymes catalyze reactions at mild temperatures. In addition, enzymes are specific to the types of reactions they catalyze. Each type of enzyme has a unique, intricately shaped binding surface called an active site. Substrate binds to the enzyme's active site, which is a small cleft or crevice in a large protein molecule. In the lock-and-key model of enzyme action, the structures of the enzyme's active site and the substrate are complementary. In the induced-fit model, the protein molecule is assumed to be flexible.

Enzymes use the same catalytic mechanisms as nonenzymatic catalysts. Several factors contribute to enzyme catalysis: proximity and strain effects, electrostatic effects, acid-base catalysis, and covalent catalysis. Combinations of these factors affect enzyme mechanisms. Active site amino acid side chains are primarily responsible for catalyzing proton transfers and nucleophilic substitutions. Nonprotein cofactors (metal and coenzymes) are used by enzymes to catalyze other type of reactions. Enzymes are sensitive to environmental factors such as temperature and pH. Each enzyme has an optimum temperature and an optimum pH. The chemical reactions in living cells are organized into a series of biochemical pathways. The pathways are controlled primarily by adjusting the concentrations and activities of enzymes through genetic control, covalent modification, allosteric regulation, and compartmentation.

Each enzyme is currently classified and named according to the type of reaction it catalyzes. There are six major enzyme categories: oxidoreductases, transferases, hydrolases, lyases, isomerases, and ligases.

2.2.2 Enzyme kinetics⁹⁶

Enzyme kinetics is the quantitative study of enzyme catalysis. Kinetic studies measure reaction rates and the affinity of enzymes for substrates and inhibitors. Kinetics also provides insight into reaction mechanisms.

To be useful to an organism, biochemical reaction is defined as the change in the concentration of a reactant or product per unit time. The initial velocity v of the reaction $A \rightarrow P$ is

$$v = -\frac{\Delta[A]}{\Delta t} = \frac{\Delta[P]}{\Delta t} \quad \text{--- 2.22}$$

where

[A]= concentration of substrate

[P]= concentration of product

t = time

Initial velocity, the rate of the reaction immediately after mixing the enzyme and substrate, is measured because it can be assumed that the reverse reaction, if possible, (i.e., conversion of product into substrate) has not yet occurred to any appreciable extent.

Enzyme kinetics has several practical applications. These include a greater comprehension of the forces that regulate metabolic pathways and the design of improved therapies.

The rate of the above reaction is proportional to the frequency with which the reaction molecules form product. The reaction rate is

$$\text{Rate} = k[A]^x \quad \text{--- 2.23}$$

where k is a rate constant, which depends on the reaction conditions (e.g., temperature, pH, and ionic strength).

Combining equations (2.22) and (2.23), we have

$$\frac{\Delta[A]}{\Delta t} = -k[A]^x \quad \text{--- 2.24}$$

Another term that is useful in describing a reaction is the reaction's order. Order is determined empirically, that is, by experimentation. Order is defined as the sum of the exponents on the concentration terms in the rate expression. Determining the order of the reaction allows an experimenter to draw certain conclusions regarding the reaction's mechanism. A reaction is said to follow first order kinetics if the rate limiting step is a unimolecular reaction (i.e. no molecular collisions are required). In the reaction $A \rightarrow P$ the experimental rate equation becomes

$$\text{Rate} = k[A]^1 \quad \text{--- 2.25}$$

If $[A]$ is doubled, the rate is observed to double. Reducing $[A]$ by half results in halving the observed reaction rate. In first-order reactions the concentration of the reactant is the function of time, so k is expressed in units of s^{-1} . In any reaction the time required for one-half of the reactant molecules to be consumed is called a half life ($t_{1/2}$).

In the reaction $A+B\rightarrow P$, if the order of A and B is 1 each, then the reaction is said to be second-order and A and B must collide for product to form (a bimolecular reaction):

$$\text{Rate} = k[A]^1[B]^1 \quad \text{--- 2.26}$$

In this circumstance the reaction rate depends on the concentration of the two reactants. In other words, both A and B take part in the reaction's rate-determining step. Second-order rate constants are measured in units of $M^{-1}s^{-1}$. Sometimes, second-order reactions involve reactants such as water that are present in great excess:



The second-order rate expression is

$$\text{Rate} = k[A]^1[H_2O]^1 \quad \text{--- 2.27}$$

Because water is present in excess, however, the reaction appears to be first-order. Such reactions are said to be pseudo-first-order. Another possibility is that only one of two reactants is involved in the rate-determining step, that is,

$$\text{Rate} = k[A]^2 \quad \text{--- 2.28}$$

The other reactant still participates in the mechanisms, but not in the rate-determining step.

When the addition of the reactant does not alter a reaction rate, the reaction is said to be zero-order. For the reaction $A\rightarrow P$ the experimentally determined rate expression is

$$\text{Rate} = k[A]^0 = k \quad \text{--- 2.29}$$

The rate is constant because reactant concentration is high enough to saturate all the catalytic sites on the enzyme molecules.

2.2.3 Michaelis-Menten Kinetics⁹⁶

One of the most useful models in the systematic investigation of enzyme rates was proposed by Leonor Michaelis and Maud Menten in 1913. The concept of the enzyme-substrate complex, first enunciated by Victor Henri in 1903, is central to Michaelis-Menten Kinetics. When the substrate S binds in the active site of an enzyme E, an intermediate complex (ES) is formed. During the transition state, the substrate is converted into product. After a brief time, the product dissociates from the enzyme. This process can be summarized as follows:



where

k_1 = rate constant for ES formation

k_{-1} = rate constant for ES dissociation

k_2 = rate constant for product formation and release from the active site

(This equation ignores the reversibility of the step in which the ES complex is converted into enzyme and product. This simplifying assumption is allowed if the reaction rate is measured while [P] is still very low. Recall that initial velocities are measured in most kinetic studies.)

According to the Michaelis-Menten model, as currently conceived, it is assumed that (1) k_{-1} is negligible when compared with k_1 and (2) the rate of formation of ES is equal to the rate of its degradation over most of the course of the reaction. (The latter premise is referred to as the steady-state assumption.)

$$Rate = \frac{\Delta[P]}{\Delta t} = k_2[ES] \quad \text{--- 2.31}$$

To be useful, a reaction rate must be defined in terms of [S] and [E]. The rate of formation of ES is equal to $k_1[E][S]$, while the rate of ES dissociation is equal to $(k_2+k_3)[ES]$. The steady-state assumption equates these two rates.

$$k_1[E][S] = (k_{-1} + k_2)[ES] \quad \text{--- 2.32}$$

$$[ES] = \frac{[E][S]}{(k_{-1} + k_2)/k_1} \quad \text{--- 2.33}$$

Michaelis and Menten introduced a new constant, K_m (now referred to as the Michaelis constant):

$$K_m = \frac{k_{-1} + k_2}{k_1} \quad \text{--- 2.34}$$

They also derived the equation

$$v = \frac{V_{\max} [S]}{[S] + K_m} \quad \text{--- 2.35}$$

Where V_{\max} = maximum velocity that the reaction can attain. This equation, now referred to as the Michaelis-menten equation, has proven to be very useful in defining certain aspects of enzyme behavior. For example, when $[S]$ is equal to K_m , the denominator in equation (2.35) is equal to $2[S]$, and v is equal to $V_{\max}/2$. The experimentally determined value K_m is considered a constant that is the characteristic of the enzyme and the substrate under specified conditions. It may reflect the affinity of the enzyme for its substrate. (If k_2 is much smaller than k_{-1} , that is, $k_2 \ll k_{-1}$, then the K_m value approximates k_{-1}/k_1 . In this circumstance, K_m is the dissociation constant for the ES complex.) The lower the value of K_m , the greater the affinity of the enzyme for ES complex formation.

An enzyme's kinetic properties can also be used to determine its catalytic efficiency. The turnover number (k_{cat}) of an enzyme is

$$k_{cat} = \frac{V_{\max}}{[E_{total}]} \quad \text{--- 2.36}$$

This quantity is the number of moles of substrate converted to product each second per mole of enzyme. Enzyme activity is measured in international units (I.U.). One I.U. is defined as the amount of enzyme that produces $1 \mu\text{mol}$ of product per minute. An enzyme's specific activity, a quantity that is used to monitor enzyme purification, is defined as the number of international units per milligram of protein. (A new unit for measuring enzyme activity called the *katal* has

recently been introduced. One katal (kat) indicates the transformation of 1 mole of substrate per second.)

2.2.4 Lineweaver-Burk Plots

K_m and V_{max} values for an enzyme are determined by measuring initial reaction velocities at various substrate concentrations. Approximate values of K_m and V_{max} can be obtained by constructing a graph, as shown in Figure 2.11. A more accurate determination of these values results from an algebraic transformation of the data. The Michaelis-Menten equation (2.35), whose graph is a hyperbola, can be rearranged by taking its reciprocal.

$$\frac{1}{v} = \frac{K_m}{V_{max}} \frac{1}{S} + \frac{1}{V_{max}} \quad \text{--- 2.37}$$

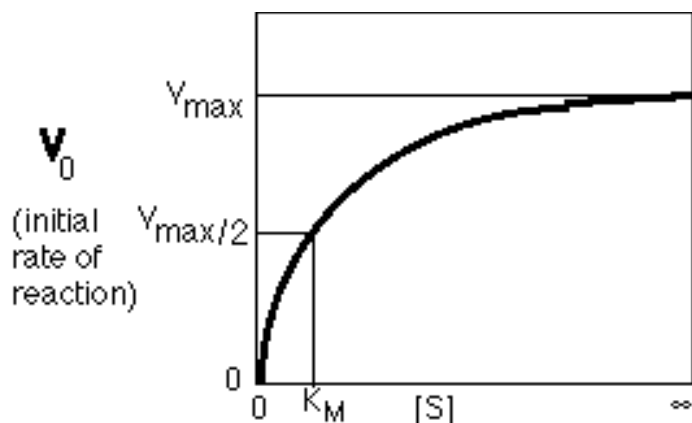


Figure 2.11: Lineweaver-Burk Plots

The reciprocals of the initial velocities are plotted as functions of the reciprocals of substrate concentrations. In such a graph, referred to as a Lineweaver-Burk double-reciprocal plot, the straight line that is generated has the form $y = mx + b$, where y and x are variables ($1/v$ and $1/[S]$, respectively) and m and b are constants (K_m/V_{max} and $1/V_{max}$, respectively). The slope of the straight line is K_m/V_{max} (Figure). As indicated in Figure, the intercept on the vertical axis is $1/V_{max}$. The intercept on the horizontal axis is $-1/K_m$.

2.2.5 Combination of surface plasmon spectroscopy and fiber optic absorbance spectroscopy

In this study, the combination of the two different types of biosensors both based on optical transduction principles is presented. Optical biosensors offer advantages in terms of miniaturization, low cost, disposability and lack of electrical interference. A home-built Surface Plasmon Resonance Spectrometer (SPR) and a commercial miniature Fiber Optic Absorbance Spectrometer (FOAS) served as a combined affinity and catalytic biosensor, respectively. A model enzyme was covalently attached to the SPR chip to catalyze the turnover of a substrate, which was detected in situ with the FOAS system.

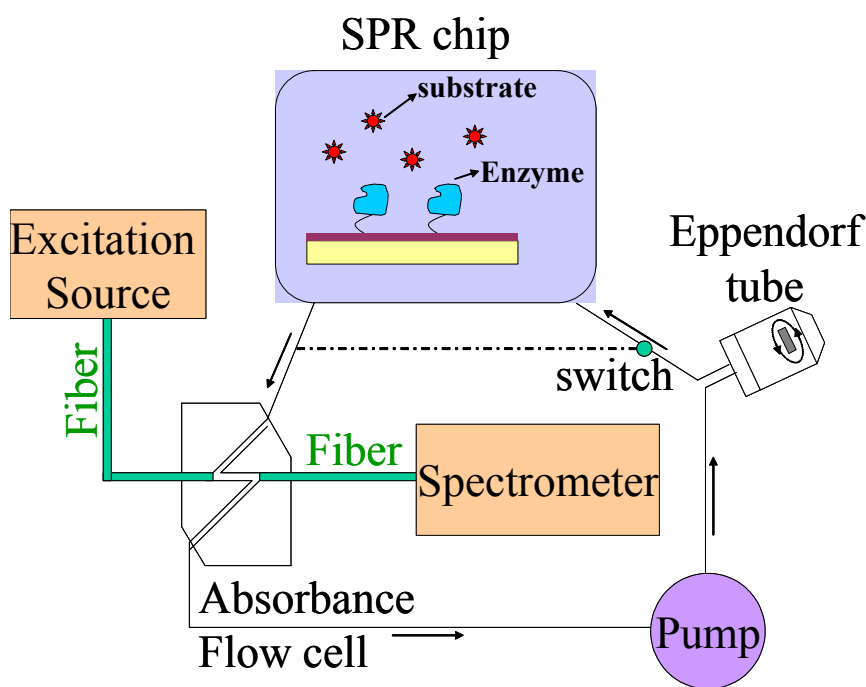


Figure 2.12: Schematic of the FOAS setup for the enzymatic activity assay.

The setup shown in Figure 2.12 consists of a 7-W Tungsten halogen light source (HL-2000-LL) powered by a regulated power supply, a “Z” configuration “FIA-Z-SMA” flow cell to measure the optical absorbance of fluids moving through the flow injection systems, a S2000 miniature fiber optic spectrometer with its own operating software, and a couple of 2m 400 μm diameter optical fibers (P400-2-UV/VIS), one of which is used for the connection of the light

source and the flow cell, and the other connecting the flow cell and spectrometer. In the flow cell, the optical fibers were connected to SMA fittings to project and receive light through the central axis of the “Z”. The flow cell has a 10mm optical path length and a 1.5 mm inner diameter, and uses UV-vis silica windows as wetting surfaces at each fiber optic junction. All components described above were purchased from Ocean Optics, Inc., The Netherlands. We used a peristaltic pump to circulate the substrate solution from an Eppendorf tube stirred by a magnetic stirring bar to the FOAS flow cell and the SPR flow cell. The connection between SPR and FOAS systems is switchable, which allows one to short-cut the connection between SPR flow cell and FOAS system for several minutes, and then let the solution run through the SPR flow cell again. By virtue of this procedure, the catalytic activity detection of “free” enzymes in the fluidic system (compared to enzymes specifically attached to the SPR surface) can be tested, which shows the desorption and contamination of enzymes in the system during the assay process. The whole setup was isolated from ambient light.

2.2.6 Catalytic activity assay of β -lactamase

We chose β -lactamase^{97,98} as a model enzyme in Chapter 3 because its three-dimensional structure is known and it exhibits an extraordinarily high catalytic efficiency, which allows for the quantification of enzyme activity in the femtomole range.⁹⁹ β -lactamases are the most common reason of bacterial resistance to β -lactam antimicrobial agents. The impact of β -lactamase has already been enormous, and its potential to challenge antimicrobial chemotherapy remains promising.¹⁰⁰ A specific amino acid such as a single cysteine residue has been introduced at a surface-exposed position of β -lactamase by site-directed mutagenesis. The unique SH group on the protein surface can then be selectively modified with ligands via thiol-specific chemistry. Biotin- β -lactamase was thus obtained by derivatizing the surface-exposed cysteine with a dithiothreitol (DTT)-cleavable biotinylation reagent for the specific attachment to the interface. Exposure to DTT was used to quantitatively release the biotin- β -lactamase from the chip.¹⁰¹

The activity of β -lactamase was measured quantitatively through the reaction with the chromogenic substrate nitrocefin, which undergoes a distinctive color change from yellow ($\lambda_{\text{max}} = 390 \text{ nm}$ at pH 7.4) to red ($\lambda_{\text{max}} = 486 \text{ nm}$ at pH 7.4) as the amide bond in the β -lactam ring is hydrolyzed by the β -lactamase. The absorbance maximum of the nitrocefin product

shifted from $\lambda = 486$ nm to $\lambda = 500$ nm in the presence of bovine serum albumin (BSA; 0.25 mg/ml), which proved to be necessary for the stabilization of low concentrations of β -lactamase in solution. Firstly, the dark (background) signal is recorded by tuning off the light source. Subsequently, the Tungsten halogen light source was switched on and pure assay buffer was injected to the flow cell, and a reference signal was recorded. After recording the dark signal and the reference signal with pure buffer, the nitrocefin solution was first injected into the FOAS system for several minutes to establish a baseline. Subsequently, the solution was allowed to run through the SPR flow cell. The conversion of the nitrocefin by the catalytic action of biotin- β -lactamase immobilized on the SPR sensor surface was monitored through changes of absorbance at $\lambda = 500$ nm as a function of time at room temperature. A relative standard deviation of 2% for the initial rate of absorbance change measured repeatedly demonstrates the excellent reproducibility of the enzymatic activity assay used in this study (details not shown).

For the Michaelis-Menten analysis, nitrocefin dissolved in assay buffer at 10 different concentrations (8 μ M, 12 μ M, 20 μ M, 28 μ M, 40 μ M, 70 μ M, 80 μ M, 120 μ M, 160 μ M, and 200 μ M) was introduced to record the initial reaction velocities of the change in absorbance. For the enzymatic activity tests in solution, 0.3 nM β -lactamase was added to different concentrations of nitrocefin in assay buffer as described above. The mixture was then immediately circulated through the FOAS system in order to record the absorbance increase at $\lambda = 500$ nm.

A set of kinetic runs was performed with the substrate nitrocefin and analyzed in the framework of the Michaelis-Menten formalism. The values of the kinetic parameters K_M and k_{cat} were determined by measuring the initial reaction velocities at various substrate concentrations. In order to determine the catalytic efficiency, k_{cat}/K_M , of an immobilized enzyme, the exact amount of enzyme on the surface has to be known. For this purpose, SPR served as an independent technique to determine the interfacial enzyme concentration. From the Fresnel analysis, one can calculate the optical thickness of Biotin- β -lactamase (assuming a refractive index of $n=1.41$).^{102;103} The concentration of enzyme inside the SPR flow cell was calculated from the adsorbed mass, converted according to de Feijter et al.'s formula from the optical thickness using a refractive index increment (dn/dc) of 0.18 ml/g for β -lactamase.⁹⁸

2.3 Langmuir Isotherm⁸¹

The development of evanescent wave biosensors offers an easy access to the kinetics of a biomolecule in the solution reversibly interacting with another biomolecule immobilized on the solid surface. The conventional treatment starts with a simple 1:1 interaction model, equivalent to the Langmuir adsorption isotherm. The simplest physically plausible isotherm is based on three assumptions¹⁰⁴:

- 1) Adsorption cannot proceed beyond monolayer coverage;
- 2) All sites are equivalent and the surface is uniform;
- 3) The ability of a molecule to adsorb at a given site is independent of the occupation of neighboring sites.

For the reversible interaction observed between an immobilized ligand B and a soluble ligate A , we have:



The rate of complex AB formation is described by the association rate constant k_{on} , which has units of $M^{-1}s^{-1}$. The rate of complex dissociation is described by k_{off} , which has units of s^{-1} . The rate of association of A with B is equal to $k_{on}[A][B]$. The rate of dissociation of AB is equal to $k_{off}[AB]$. On mixing A and B , association and dissociation of AB will occur. Equilibrium will eventually be reached if the rates of association and dissociation of AB are equal. At equilibrium, $[AB]$, $[A]$ and $[B]$ are constant. Hence, at equilibrium:

$$k_{on}[A][B] = k_{off}[AB] . \quad \text{--- 2.39}$$

This may be rearranged as follows:

$$\frac{[A][B]}{[AB]} = \frac{k_{off}}{k_{on}} = K_D \quad \text{--- 2.40}$$

where K_D is termed the dissociation equilibrium constant, and has units of M. The lower the value of K_D , the greater the affinity. The reciprocal term K_A , the association equilibrium constant, having units of M^{-1} , is sometimes used in the literature as the measure of affinity, where:

$$K_A = \frac{1}{K_D} \quad \text{--- 2.41}$$

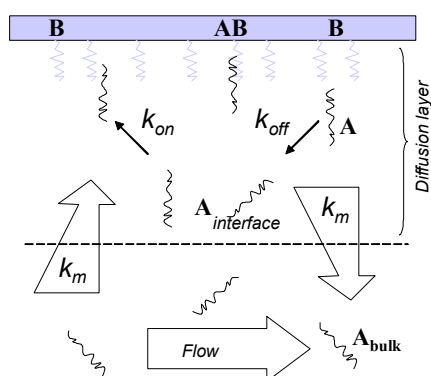


Figure 2.13: Schematic showing basic interactions on the biosensor surface. The ligand (B) is attached to the surface via a flexible linker. During the association phase, analyte (A) is flowed past the surface. k_m is the mass transport coefficient used to describe the diffusion of analyte through the diffusion layer. k_{on} and k_{off} are the association and dissociation rate constants, which describe the formation of the complex (AB).

However, as shown in Figure 2.13, at a solid/liquid interface, the transportation of A from the bulk solution to the interface has to be taken into account. Thus, the formation of the complex AB will be also influenced by the mass-transport rate constant k_m from the bulk to the interface and from the interface to the bulk, expressed as:

$$\frac{d[AB]}{dt} = k_f [A_{bulk}] [B] - k_r [AB] \quad \text{--- 2.42}$$

where k_f is the forward rate constant, and k_r is the reverse rate constant. From (2.38), at the interface, there is also:

$$\frac{d[AB]}{dt} = k_{on}[A_{interface}][B] - k_{off}[AB]. \quad \text{--- 2.43}$$

Combination of (2.42) and (2.43) will yield:

$$k_f = \frac{k_{on}k_m}{k_m + k_{on}[B]} = \frac{k_{on}}{1 + \frac{k_{on}[B]}{k_m}}, \quad k_r = \frac{k_{off}k_m}{k_m + k_{on}[B]} = \frac{k_{off}}{1 + \frac{k_{on}[B]}{k_m}}. \quad \text{--- 2.44}$$

If k_m is very small, or the surface concentration of B is very large, i.e. $k_m \ll k_{on}[B]$, the interaction is controlled by the mass-transport rate:

$$\frac{d[AB]}{dt} = k_m[A_{bulk}] - \frac{k_m k_{off}}{k_{on}[B]}[AB]. \quad \text{--- 2.45}$$

At the initial association stage, $[AB]$ is very small, the complex forming rate is solely dependent on the bulk concentration of A , and the binding signal increases linearly with time t :

$$\frac{d[AB]}{dt} = k_m[A_{bulk}]. \quad \text{--- 2.46}$$

This can be used for the concentration analysis of ligate A .

If the mass-transport rate is much larger than the association rate constant, or the surface concentration of the immobilized species is low, i.e., $k_m \gg k_{on}[B]$, then $[A_{interface}] = [A_{bulk}]$. k_f and k_r approximately equal to the intrinsic rate constants k_{on} and k_{off} . Under such conditions, the binding rate can be expressed as:

$$\frac{d[AB]}{dt} = k_{on}[A][B] - k_{off}[AB]. \quad \text{--- 2.47}$$

After some reaction time, t , $[B] = [B]_0 - [AB]$, where $[B]_0$ is the concentration of B at $t=0$. As shown in Figure 2.13, the ligands are immobilized onto the surface and continuously replenished from the injection volume flowing over the surface. The signal observed, R , is proportional to the formation of AB complexes on the surface and the maximum signal, R_{max} , is proportional to the surface concentration of active ligands on the surface. Therefore, (2.47) becomes:

$$\frac{dR}{dt} = k_{on} C (R_{max} - R) - k_{off} R \quad \text{--- 2.48}$$

where C is the constant concentration of ligates in solution. This yields the solution:

$$R_t = \frac{k_{on} C R_{max}}{k_{on} C + k_{off}} (1 - e^{-(k_{on} C + k_{off})t}) = R_{eq} (1 - e^{-(k_{on} C + k_{off})t}) \quad \text{--- 2.49}$$

where R_{eq} is the equilibrium response at a given ligate concentration C . If considering about the baseline correction, (2.49) becomes:

$$R_t = (R_{eq} - R_{t=0}) (1 - e^{-(k_{on} C + k_{off})t}) + R_{t=0} \quad \text{--- 2.50}$$

where $R_{t=0}$ is an additional fitting parameter equivalent to the signal at the point of injection of ligates ($t = 0$), which is not zero.

In the dissociation process, where $C = 0$ because of the fresh buffer rinse, (2.34) becomes:

$$\frac{dR}{dt} = -k_{off} R \quad \text{--- 2.51}$$

The solution for (2.51) is:

$$R_t = R_0 e^{-k_{off}t} \quad \text{--- 2.52}$$

where R_0 is the response at the start of the dissociation process. If considering about the baseline correction, (2.52) becomes:

$$R_t = (R_0 - R_{t \rightarrow \infty})e^{-k_{off}t} + R_{t \rightarrow \infty} \quad \text{--- 2.53}$$

where $R_{t \rightarrow \infty}$ is the response value after infinite time and represents complete dissociation of the AB complexes. Equation (2.50) and (2.53) can be utilized to yield k_{on} and k_{off} from a single set of association and dissociation data via nonlinear least squares fit.

On the other hand, the interaction dynamic also can be deduced from the equilibrium analysis. Upon equilibrium of the dynamics, the net effect of the association and the dissociation process is zero, from (2.48) one obtains:

$$R_t = R_{eq} = \frac{k_{on}CR_{max}}{k_{on}C + k_{off}} = \frac{CR_{max}}{C + \frac{k_{off}}{k_{on}}} = \frac{CR_{max}}{C + K_D} = \frac{CK_A R_{max}}{CK_A + 1} \quad \text{--- 2.54}$$

which gives the equilibrium response at a given analyte concentration C . Experimentally, this can be achieved by a stepwise saturation of the ligand on the surface by a series of concentrations of ligates, or titration method in this research. Plotting these equilibrium responses R_{eq} as a function of the ligate concentration C results in the well-known Langmuir adsorption isotherm. The dissociation equilibrium constant K_D can be obtained directly from this curve as being equal to the ligate concentration at $R_{max}/2$. Meanwhile, a plot of C/R_{eq} as a function of C yields a straight line with a slope of $1/R_{max}$ and a y -axis intercept of $1/R_{max}K_A$.

3 Comparative detection of interfacial binding of β -lactamase to different matrices combined with catalytic activity assay

3.1 Introduction

Biosensors, consisting of a molecular recognition element and a transducer, are contributing to diverse scientific fields and are used to examine interactions between partners ranging in size from small molecules to whole cells.¹⁰⁵ In this study, the combination of the two different types of biosensors both based on optical transduction principles is presented. Optical biosensors offer advantages in terms of miniaturization, low cost, disposability and lack of electrical interference. A home-built Surface Plasmon Resonance Spectrometer (SPR) and a commercial miniature Fiber Optic Absorbance Spectrometer (FOAS) served as a combined affinity and catalytic biosensor designed for the quantitative in-situ evaluation of the degree of binding and the catalytic activity of surface-immobilized enzymes. A model enzyme was covalently attached to the SPR chip to catalyze the turnover of a substrate, which was detected in situ with the FOAS system. SPR relies on the measurement of binding-induced refractive index changes and thus is a prominent example of label-free detection principles. Over the past ten years, SPR biosensor technology has made great progress, resulting in the development of a large number of SPR sensor platforms, biomolecular recognition elements, and measurement formats.¹⁰⁶ Miniature FOAS, on the other hand, has been described in detail in Section 2.2.5. Briefly, light from a halogen lamp reaches a special FOAS flow cell, which couples the substrate solution flowing through the cell with the surface-immobilized β -lactamase of the SPR sensor to the FOAS system and to two fibers used for excitation and detection. The spectrum of the transmitted light is detected by a miniature fiber optic spectrometer. The parallel measurements offer the opportunity for on-line activity detection of surface-attached enzymes. The immobilized enzyme does not have to be in contact with the catalytic biosensor. The SPR chip can easily be cleaned and reused for several assays.

To be quantitative and efficient, sensors need to be rapid, specific, reproducible, and highly sensitive. Furthermore, they need to have an optimized density of highly selective and specific

biofunctional groups for the recognition (and binding) of the analyte molecule of interest. Improved strategies for the immobilization of biologically active recognition elements have led in the past years to a substantial increase in sensitivity and selectivity of bioaffinity sensor devices. Controlling the immobilization of biomolecules on surfaces, while preventing nonspecific adsorption of undesired species, has become an important goal for monitoring specific biointeractions and binding of biomolecules or cells. Therefore, in the past decades, many immobilization strategies have been established. Attempts to control the biomolecular density and orientation and presentation of biomolecules at the solid-liquid interface for better sensitivity and reproducibility have been undertaken through various strategies for covalent and site-specific immobilization. In this paper, five different types of interfaces were investigated based on a generic biotin-NeutrAvidin binding matrix for the quantitative control of the degree of enzyme binding, as well as for measuring the enzymatic activity of biotin- β -lactamase. Biotin and avidin analogues exhibit one of the strongest noncovalent affinity interactions in nature ($K_d = 10^{13-15} \text{ M}^{-1}$ in solution), and as such have been used for a wide range of applications including immunoassays, cytochemistry, protein purification, and diagnostics.¹⁰⁷ The first example of the five matrices is a monolayer of self-assembled, biotin-terminated alkanethiol (SAM) on gold onto which NeutrAvidin was immobilized. Once the binding of a molecularly ordered NeutrAvidin monolayer was established, the remaining free binding sites exposed to the aqueous phase were used to build subsequent layers. This kind of a well-organized and relatively stiff matrix was used as a control for the other four kinds of highly flexible matrices used in the study. Poly (L-lysine)-*g*-poly (ethylene glycol) (PLL-*g*-PEG) is a polycationic copolymer that adsorbs spontaneously from aqueous solutions onto negatively charged surfaces via electrostatic or covalent interactions. It forms monolayers with densely packed, brush like and highly flexible PEG chains, which extend toward the aqueous solution. In addition, the use of PEG tethers for biomolecular immobilization has been reported to minimize loss of protein activity.¹⁰⁸ PLL-*g*-PEG graft copolymers carrying terminal biotin groups (PLL-*g*-PEG/PEG-biotin) were synthesized and used for the build-up of capture matrices for proteins. These biotinylated, PEG-brush surfaces have been shown to resist nonspecific adsorption from serum while still allowing for the specific surface binding of avidin, NeutrAvidin, or streptavidin and the subsequent immobilization of biotinylated biomolecules such as biotinylated antibodies.¹⁰⁷

As a first variant, carboxyl-terminated alkanethiols were assembled on a gold surface in order to form a negatively charged surface that served as a substrate for the subsequent polymer adsorption via either electrostatic or covalent binding. For comparison, gold substrates were coated with thin metal-oxide layers consisting of niobium oxide (Nb₂O₅) or silicon oxide (SiO₂), onto which polycationic polymeric adlayers were directly adsorbed by electrostatic interactions. Owing to the fact that high-refractive-index, transparent oxides of transition metals such as niobium or tantalum, are suitable as waveguiding layers for optical evanescent-wave-based sensing devices, the deposition of such metal oxide layers on top of a noble metal offers the potential of using surface plasmon (SPR) spectroscopy, optical waveguide lightmode spectroscopy (OWLS), and plasmon-waveguide resonance (PWR) spectroscopy, in particular. This way, results obtained by the different methods can be compared directly.

In this study, surface plasmon resonance (SPR) spectroscopy and optical waveguide lightmode spectroscopy (OWLS) were used to monitor quantitatively and in-situ the spontaneous adsorption of polymers, as well as proteins, onto the sensor surface, and the possibilities to regenerate the sensor surface. For the detection of the activity of the enzyme immobilized on the five different matrices as well as in solution, a miniature Fiber Optic Absorbance Spectroscopy (FOAS) system was assembled for the detection of a chromophoric reaction catalyzed by β -lactamase. We performed a colorimetric assay with the chromogenic substrate nitrocefin¹⁰⁹ in order to quantitatively detect the catalytic activity of β -lactamase. The stability of the surface-immobilized enzyme was explored through enzymatic activity assays. The enzymatic activities in solution and for the enzymes with different surface coverages based on the different interfaces were compared, allowing us to judge and discuss the effect of the different surface immobilization schemes on the catalytic activity.

3.2 Materials

The thiol derivatives (Figure 3.1) were dissolved in ethanol at a concentration of 5mM. NeutrAvidin, purchased from Molecular Probes, Leiden, The Netherlands, was dissolved in 4-(2-Hydroxyethyl) piperazine-1-ethane-sulfonic acid (HEPES) II buffer (10mM HEPES, 150 mM NaCl, pH 7.4) at a concentration of 0.15 mg/ml. Biotin- β -lactamase variants (Q269C) were produced as described before⁹⁹ and dissolved in HEPES II buffer at a concentration of 2 μ M. PLL-g-PEG/PEG-biotin was synthesized and characterized according to published

protocols.⁹⁹ PLL(20kDa)-g(3.4)-PEG(2kDa)/PEG(3.4kDa)-biotin was dissolved in HEPES I buffer (10 mM HEPES, pH 7.4) at a concentration of 1mg/ml. DTT (Dithiothreitol) was dissolved at a concentration of 50 mM in HEPES II buffer. Human serum (10 mg, purchased from Sigma-Aldrich, Germany) was dissolved in water at a concentration of 1mg/ml. D-Biotin, purchased from Sigma-Aldrich was dissolved in HEPES II buffer at a concentration of 1.15 mM. HELLMANEX, purchased from Hellma GmbH, Germany, was diluted with water to a concentration of 1%. Nitrocefin, purchased from Calbiochem, was dissolved in assay buffer (10 mM HEPES-NaOH, pH 7.4, 150 mM NaCl, 0.25mg/ml BSA, 0.5% (v/v) dimethyl sulfoxide (DMSO)) at different concentrations. All other reagents were purchased from Sigma-Aldrich, Germany. Buffers were prepared using ultrapure water (18 M Ω ·cm).

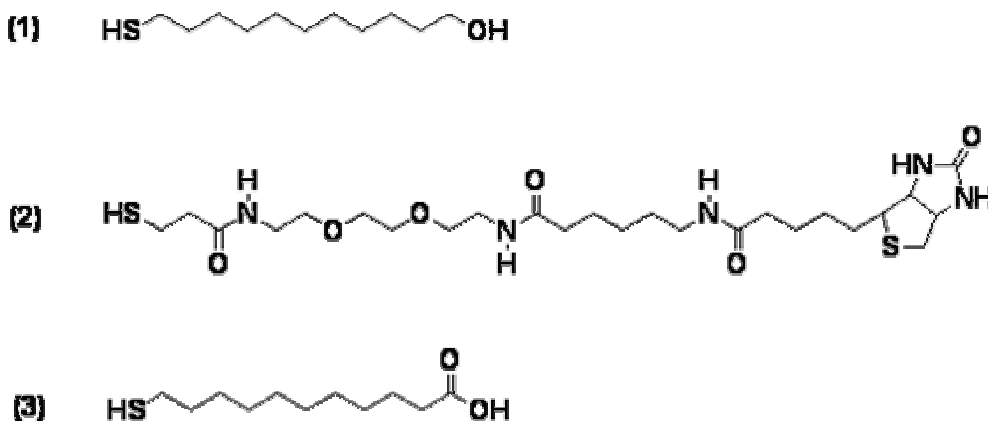


Figure 3.1 Structure formula of (1) hydroxyl-terminated thiol (11-Mercapto-1-undecanol), (2) biotin-terminated thiol (HS-c12-dadcoo-Biotin), and (3) carboxyl-terminated thiol (11-Mercaptoundecanoic acid) employed for the preparation of self-assembled monolayers (SAMs).

3.3 Substrates

Slides (Schott, $n=1.85$ at $\lambda = 633\text{nm}$) were carefully cleaned with 1% HELLMANEX, ultrapure water and ethanol in turn, coated with 2 nm chromium (Cr) followed by 50 nm of gold (Au) by thermal evaporation in a commercial instrument (Edwards). For matrices C and D of Figure 2, either 4 nm Nb₂O₅ or 10 nm SiO₂ were sputter-coated on top of the Cr/Au substrate by a Leybold Z600 magnetron sputtering unit at the Paul Scherrer Institute, Villigen, Switzerland. Metal-oxide-coated substrates were cleaned in a plasma cleaner (Technics

Plasma-Prozessor 200-G, Germany, 300W) for 5 min before surface modifications using oxygen as the plasma gas. For matrices A, B and E, freshly coated Cr/Au substrates were directly immersed into the thiol solutions, then sealed, and kept overnight at room temperature. The substrates were removed, rinsed thoroughly with ethanol, and blown-dried in a stream of nitrogen. The substrates were used immediately after preparation.

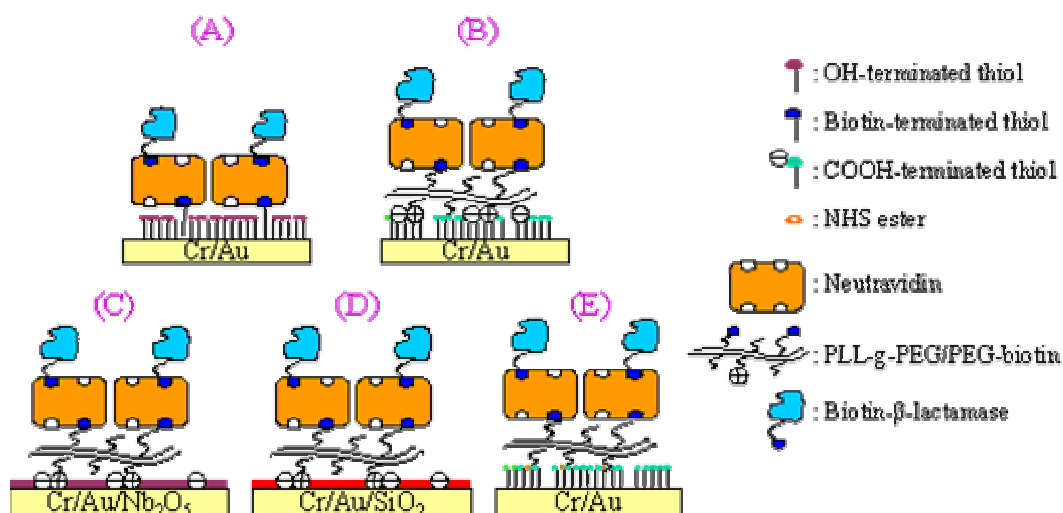


Figure 3.2: Schematic of the five matrices used for protein binding.

3.4 Comparison of Surface modification based on five kinds of matrices

Five different interfacial architectures were produced and served as sensor platforms based on the specific attachment of biotin-functionalized β -lactamase (biotin- β -lactamase). Biotinylated molecular systems were used resulting in five generic biotin-NeutrAvidin binding matrices. As shown in Figure 3.2, thiols (Figure 3.1) were assembled onto chromium/gold films from ethanolic solution for matrices A, B and E. The functionalization of matrix A was achieved by forming biotinylated self-assembled monolayers (SAMs) with a binary mixture containing 10 mol% of the biotinylated thiol and 90 mol% of the OH-terminated diluent thiol at a net thiol concentration of 357 μ M in absolute ethanol (99%) over night,¹¹⁰ followed by the attachment of NeutrAvidin for 30 min and the further attachment of biotin- β -lactamase for another 30 min. The biotin- β -lactamase utilized in this study contains a single biotin group and

a 2.9-nm-long DTT-cleavable disulfide bridge linker between biotin group and surface exposed cystein residue of the genetically modified lactamase. Release of β -lactamase from the surface by DTT was quantitative, thus proving that all β -lactamase molecules were specifically bound to the surface via their biotin groups.¹¹¹

For matrices B and E, carboxyl-terminated alkanethiol SAMs were used for the immobilization of the graft copolymer PLL-g-PEG/PEG-biotin via either electrostatic interaction or covalent binding. Nb₂O₅ and SiO₂ were sputter-coated on top of the Cr/Au substrate for matrix C and D. Nb₂O₅ and SiO₂-coated chips were used in view of the high negative surface charge density at neutral pH and the resulting strong electrostatic binding of the polycationic polymers PLL-g-PEG/PEG-biotin. The general functionality of this type of interface has already been successfully demonstrated¹⁰⁷ for applications in bioaffinity sensing. PLL-g-PEG/PEG-biotin has been chosen as the surface immobilization platform for four out of the five matrices. At neutral pH, PLL-g-PEG/PEG-biotin spontaneously and firmly attaches from aqueous solutions to negatively charged surfaces through multiple-site electrostatic (matrix B, C, and D) or covalent (matrix E) interactions between the polycationic PLL backbone and the negatively charged surface.^{112;113} The high density of PEG molecules results in a brush-like, flexible, uncharged, strongly hydrated, and non-interactive interface, which allows for gentle immobilization of proteins and other biomolecules. The biologically active tertiary structure of the attached protein is preserved as well as the accessibility of its active site to the substrate reaction partner. NeutrAvidin can specifically bind to the biotin groups of the polymer, and the immobilization of β -lactamase onto the NeutrAvidin occurs through a biotinylated spacer.

The SPR technique allows us to determine in situ the amount of biotin- β -lactamase as well as PLL-g-PEG/PEG-biotin and NeutrAvidin bound to the surface. A full angular scan was recorded for every single layer after surface attachment with the wavelength of the laser light source $\lambda = 632.8$ nm (HeNe laser). All respective angular shifts were Fresnel-analyzed. From Fresnel's equations, one can calculate the optical thickness of the coating (assuming for PLL-g-PEG/PEG-biotin and biotin- β -lactamase, a refractive index of $n = 1.41$, and for NeutrAvidin, a refractive index of $n = 1.45$).^{102;103}

The attachment of NeutrAvidin and biotin- β -lactamase for all five matrices was achieved by two different strategies:

1. Stepwise (sequential) binding of NeutrAvidin and biotin- β -lactamase:

Chips were incubated with NeutrAvidin for 30 min and rinsed with HEPES II buffer; then the biotin- β -lactamase was injected into the flow cell and incubated for 30 min. Subsequently, unspecifically bound β -lactamase was removed by rinsing with HEPES II buffer.

2. One-step binding of the complex of NeutrAvidin/biotin- β -lactamase preformed in solution:

NeutrAvidin was first mixed with biotin- β -lactamase in a molar ratio of 1:2 in HEPES II buffer for 30 min at room temperature and a final concentration of 0.03 mg/ml NeutrAvidin and 0.03 mg/ml biotin- β -lactamase. Subsequently, the formed complex was immobilized on the surface until equilibrium was reached (ca. 30 min incubation). Release of immobilized β -lactamase from the surface was achieved by incubation with 50mM DTT in HEPES II buffer for 15 min.

PLL-g-PEG/PEG-biotin monolayers form a soft, gel-like matrix with substantial flexibility of the PEG chains (and the biotin group attached to the PEG termini). A consequence is that with the stepwise (sequential) binding strategy, after the initial binding of NeutrAvidin to the PEG-biotin surface, PEG chains (including both neighboring PEG chains planted on the same PLL backbone and those from other PLL-g-PEG/PEG-biotin chains) with free biotin groups may additionally occupy biotin-binding sites of the surface-bound NeutrAvidin; this time-dependent process may finally result in the majority of the originally free binding sites of NeutrAvidin becoming blocked, and therefore no longer available for subsequent binding of biotinylated molecules in this stepwise functionalization protocol. The alternative to get a higher amount of surface-bound biotin- β -lactamase is to pre-incubate the mixture of NeutrAvidin and biotin- β -lactamase, and subsequently attach the complex to the surface-bound PLL-g-PEG/PEG-biotin in one step (one-step binding strategy). DTT (Dithiothreitol) was used to cleave the disulfide linkage between β -lactamase and its biotin label. This step allows us to compare quantitatively the amount of surface-bound NeutrAvidin/biotin- β -lactamase complex with the mass of β -lactamase released upon DTT exposure. We refer to this strategy as pre-incubation protocol.

The results of the comparative study of stepwise and pre-incubation protocols for all five matrices are given in Figure 3.3. Comparable amounts of immobilized enzyme were obtained for matrix A with both protocols, while for matrices B, C, and D, a significantly lower surface coverage of biotin- β -lactamase was found for the stepwise-binding compared to the pre-

incubation protocol. These differences can be understood on the basis that matrix A is a rather stiff, 2-D molecularly ordered surface-immobilization platform, for which additional blocking of biotin-binding sites of NeutrAvidin (as discussed above) is impossible or very unlikely, while matrices B, C, and D, prepared with the brush-like, flexible polymer, PLL-g-PEG/PEG-biotin, are rather soft matrices for the surface attachment and prone to major rearrangement of immobilized molecules. The property of matrix E assembled according to the covalent binding strategy of PLL-g-PEG/PEG-biotin with the carboxyl-terminated SAMs is expected to be intermediate in view of the lower surface coverage of PLL-g-PEG/PEG-biotin, which subsequently induces the lower binding amount of biotin- β -lactamase compared to other PLL-g-PEG/PEG-biotin based matrices (shown in Figure 3.3), especially to matrix B. The low surface coverage of PLL-g-PEG/PEG-biotin effectively reduced the NeutrAvidin-blocking effect contributed from PEG groups planted on different PLL backbones.

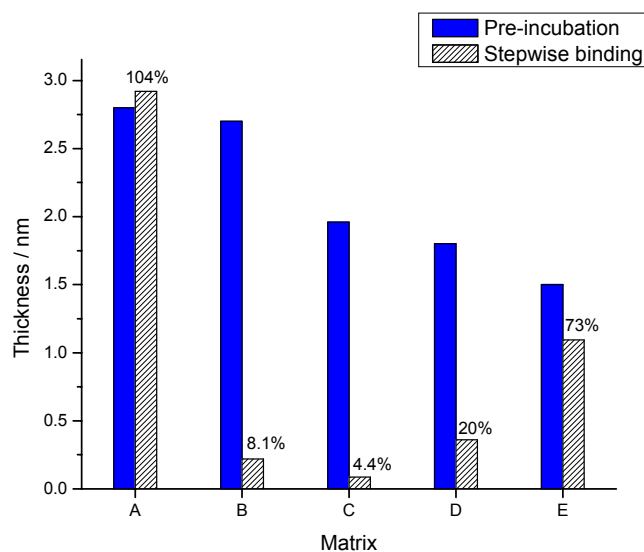


Figure 3.3: Comparison of the optical thickness of surface bound β -lactamase between stepwise binding and pre-incubation strategies based on five different kinds of matrices detected by SPR. Inset numbers indicate the values of $T_{\text{stepwise}} / T_{\text{pre-incubation}}$ (ratio of optical thickness of surface attached biotin- β -lactamase based on stepwise binding strategy to the obtained thickness based on pre-incubation strategy). A, B, C, D, and E: symbols of matrices used in the study.

3.5 Comparison of different optical detection methods (OWLS and SPR):

OWLS is another in situ, label-free, evanescent-field-based technique that measures the refractive index and thickness of adsorbed macromolecules.¹¹⁴ The typical detection sensitivity of the instrument is 1 ng/cm². The same protocols as those for SPR measurements were applied for the in-situ investigation of the surface adsorption and immobilization processes utilizing Nb₂O₅ as the substrate (matrix C). OWLS measurements were performed with chips based on matrix C. Optical waveguide chips for OWLS measurements were purchased from Microvacuum, Ltd. (Budapest, Hungary), and consisted of a 1-mm-thick AF45 glass substrate and a 200-nm-thick Si_{0.75}Ti_{0.25}O₂ waveguiding surface layer. A 12-nm-thick Nb₂O₅ layer was sputter-coated on top of the waveguiding layer. Nb₂O₅-coated waveguide chips were sonicated in 0.1M HCl for 10 min, thoroughly rinsed with ultrapure water, dried in a stream of nitrogen, and treated for 2 min in an oxygen plasma in a plasma cleaner/ sterilizer PDC-32G (Harrick, Ossining, NY, USA). After inserting the chips into the OWLS flow cell, PLL-g-PEG/PEG-biotin was immobilized on the surface as a platform for the further attachment of NeutrAvidin and biotin-β-lactamase. All steps were performed according to the pre-incubation protocol described above.

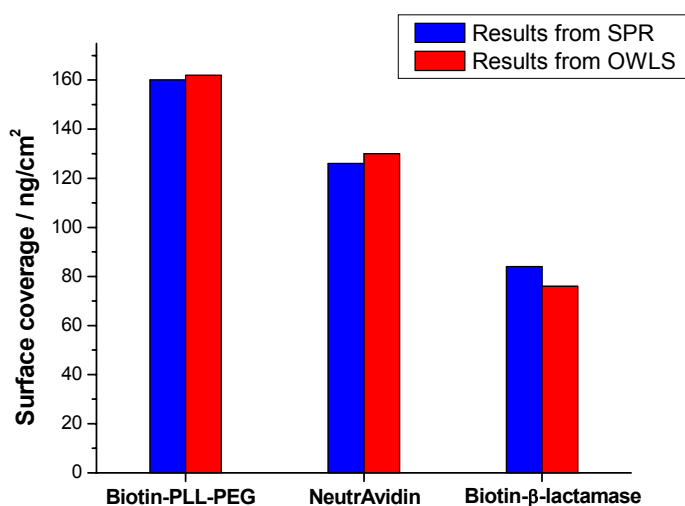


Figure 3.4: Comparisons of the surface coverage amounts of PLL-g-PEG/PEG-Biotin, NeutrAvidin, and β-lactamase based on matrix C with pre-incubation strategy obtained from SPR and OWLS measurements, respectively.

Figure 5 shows the comparison of surface coverages of PLL-g-PEG/PEG-Biotin, NeutrAvidin, and β -lactamase determined by SPR and OWLS. With respect to the data analysis of SPR and OWLS, the adsorbed mass of polymer and protein was calculated from the measured effective refractive indices and thickness values according to

$$A = d \frac{(n - n_o)}{\partial n / \partial c}$$

and de Feijter et al.'s formula.¹¹⁵ With n_0 being the refractive index of the solution, the adsorbed amount A of protein per unit area can be calculated provided the index increment $\partial n / \partial c$ of the protein solution is determined independently.^{99;110} $\partial n / \partial c = 0.212$ ml/g for NeutrAvidin, 0.18 ml/g for β -lactamase, and 0.16 ml/g for polymers were used for the calculation.^{102;103}

With deviations of less than 5% in the adsorbed mass on surfaces of type matrix C (Figure 3.4), we conclude that the results of the two independent sensing techniques are in excellent agreement.

Table 3.1: Evaluation of regeneration possibilities for five matrices based on stepwise binding strategy

Matrix	A	B	C	D	E
	Biotin-terminated SAM	Carboxyl-terminated SAM	Nb ₂ O ₅	SiO ₂	Carboxyl-terminated SAM (NHS ester)
Regeneration Possibility	N	Poor	Y	N	N
PLL-g-PEG/PEG-Biotin	-----	105%	90%	-----	-----
NeutrAvidin	-----	54%	98%	-----	-----
Biotin- β -lactamase	-----	-----	74%	-----	-----

3.6 Estimation of regeneration possibilities

Regeneration procedures are able to disassemble a supramolecular architecture of a sensor chip into its individual building blocks followed by a re-assembly process, thus allowing for the

repetition of surface functionalization and reuse as sensor. The feasibility to regenerate the chip surfaces was tested for all five matrices. 0.1M HCl was used to regenerate the substrates for matrices A, B and E, while for matrices C and D, we used 1% HELLMANEX. The same binding procedures for PLL-g-PEG/PEG-biotin, NeutrAvidin, and biotin- β -lactamase were used based on the stepwise binding strategy to compare the binding abilities after regeneration with those before regeneration.

Table 3.1 shows the regeneration results for all five matrices. The numbers indicate the ratio of the amount of bound PLL-g-PEG/PEG-biotin, NeutrAvidin and biotin- β -lactamase after regeneration to that before regeneration. Matrix C on the Nb₂O₅ surface can be regenerated at a level of 74% (in terms of restored enzyme coverage) using 1% HELLMANEX to deionize the metal oxide surface and release the electrostatically attached PLL-g-PEG/PEG-Biotin. A new supramolecular architecture can be formed if the surface is again exposed to a fresh polymer solution. The amounts of re-assembled PLL-g-PEG/PEG-Biotin, NeutrAvidin, and biotin- β -lactamase on matrix C show a very satisfactory regeneration. Matrix B, built on the carboxyl terminated SAM via electrostatic interaction, can be partly regenerated with 53.6% of NeutrAvidin rebound, indicating the lower amount of re-assembled PLL-g-PEG/PEG-biotin. However, hardly any signal of biotin- β -lactamase attachment can be obtained during the re-assembled process derived from SPR simulation. Assuming that a fraction of biotin- β -lactamase might be attached to the surface-bound NeutrAvidin, there must be some loosely bound molecules (i.e. PLL-g-PEG/PEG-biotin or NeutrAvidin attached to PLL-g-PEG/PEG-biotin) desorbing upon rinsing, indicating the unstable property of Matrix B after regeneration. The SiO₂ substrate of Matrix D is so brittle that the applied regeneration process totally disturbed the shape of SPR curve (details not shown), indicating the perturbation of the sensor surface. As a result, matrix D cannot be regenerated in spite of its assembly mechanism via the electrostatic interaction. Matrix E was assembled through covalent attachment. It cannot be regenerated by simply deprotonating the SAM surface. With respect to matrix A, NeutrAvidin binds biotin at four binding sites, with an extremely high binding constant ($K_d = 10^{13-15} \text{ M}^{-1}$), which makes the binding process effectively irreversible. However, the NeutrAvidin-biotin system of matrix A offers a regeneration strategy by using ligands of biotin analogues with a reduced affinity for the binding pocket. This option could result in a design strategy for the

competitive replacement of one ligand by another one with a higher binding constant thus making the sensor surface reusable.¹¹⁶

3.7 Enzyme activity assay

The activity of β -lactamase was tested quantitatively as described in Section 2.2.6. The combination of SPR and FOAS¹¹⁷ (details see Section 2.2.5) was used for the assay.

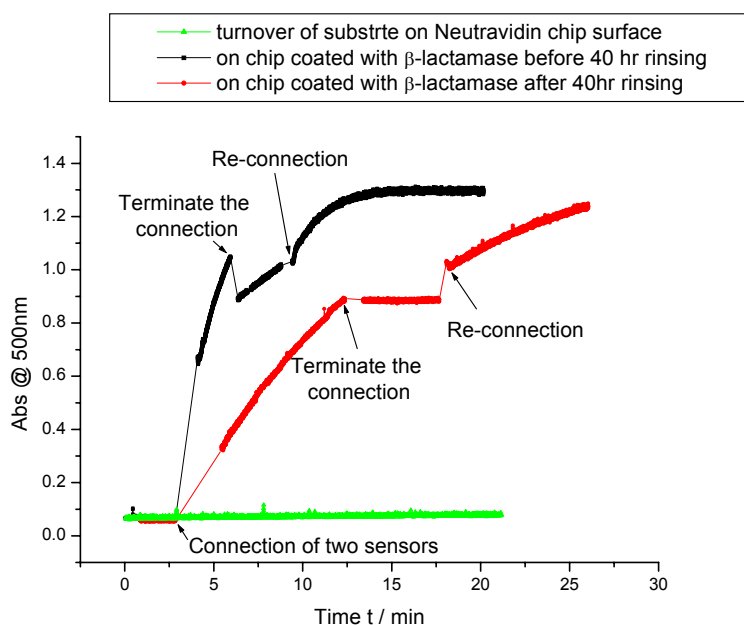


Figure 3.5: Enzymatic activity and Stability of surface immobilized β -lactamase based on matrix A

Enzyme stability, both in terms of active conformation and stable immobilization, is a key factor in terms of sensitivity and lifetime of enzyme-based biosensors. In the standard enzyme assay protocols used in this study, the SPR chip surfaces were either tested immediately after enzyme immobilization, or first rinsed constantly in HEPES II buffer with a flow rate of 37 μ l/min for 40 hours at room temperature before the enzymatic assay was performed in order to remove any loosely bound β -lactamase. We also let the substrate solution run across a NeutrAvidin surface with no β -lactamase immobilized, as a background control of the turnover of the nitrocefin. The kinetics of the absorbance increase for (a) the background, (b) freshly

bound β -lactamase and (c) after 40 hr incubation were monitored as a function of time, and compared for chips based on matrix A and using 80 μ M nitrocefin solution with the flow rate of 1.0 ml/min. The enzymatic turnover after the exposure of the freshly enzyme-coated chip to the substrate solution running through the SPR flow cell, followed by a short rinse in HEPES II buffer is shown in Figure 3.5 (black curve). The immobilized biotin- β -lactamase showed significant enzymatic activity. Upon short-cutting the connection between the SPR and the FOAS flow cell (cf. Figure 2.12), the enzymatic turnover of nitrocefin did not cease as expected but continued at a lower rate, due to loosely bound enzyme molecules, that desorbed from the SPR chip during the assay and catalyzed the turnover of the substrate in solution. If the two systems were re-connected, the enzymatic turnover was re-established.

The red curve in Figure 3.5 shows the same experiment, except that the chip was this time rinsed in the flow cell with pure buffer for 40 hrs and at a low flow rate of 37 ml/min. The chip showed again significant enzymatic activity with, however, a lower reaction rate this time in comparison to the freshly coated β -lactamase chip. This is obviously a consequence of the desorption of loosely bound adsorbed β -lactamase during the long-term buffer storage, which is supported by our previous study with OLWS detection.⁹⁹ If the connection between the SPR and the FOAS flow cell was shortcut, the turnover of nitrocefin ceased, indicating that this time negligible amounts of enzyme were present in solution and that the 40 hrs buffer incubation had efficiently removed the loosely bound enzyme. Combined with the observation that no turnover of nitrocefin was observed if the substrate solution flowed across a chip surface that had immobilized NeutrAvidin, but no β -lactamase (Figure 3.5, green curve), we therefore conclude that the long-term exposure to buffer had indeed removed all or most of the unspecifically bound β -lactamase. β -lactamase, specifically immobilized on chips, was found to be stable and unable to be desorbed from the SPR chip during the assay.

The first set of catalytic activity assay of β -lactamase was performed based on matrix A with different surface coverages of β -lactamase. Different surface coverages were obtained by adding biotin- β -lactamase at concentrations of 100nM, 400nM, and 1 μ M to the NeutrAvidin coated surface to get low, medium, and high surface coverage of biotin- β -lactamase, respectively, followed by rinsing with pure HEPES buffer to terminate the immobilization (Figure 3.6). After the immobilization of biotin- β -lactamase, the chips were rinsed consecutively with pure buffer at a very low flow rate (36.5 μ l/min) for 40 hr before the

enzymatic assay was performed. All measurements were done at room temperature. Table 3.2 lists the quantitative surface immobilization data of β -lactamase, as well as K_M , k_{cat} , and k_{cat}/K_M values for the catalytic analysis. The relatively high standard deviations of kinetic parameters are due to the limited nitrocefin concentration range accessible in the Michaelis-Menten experiment as a result of limited nitrocefin solubility.

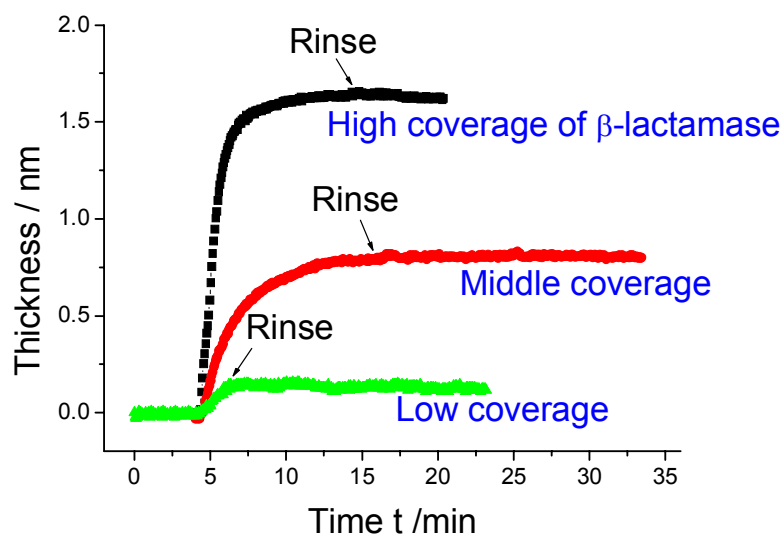


Figure 3.6: Kinetics of the turnover of nitrocefin detected with FOAS for the investigation of surface-bound β -lactamase monitored at $\lambda = 500\text{nm}$.

Table 3.2: SPR results and kinetic parameters obtained from miniature Fiber Optic Absorbance spectroscopy (FOAS) for free and surface immobilized β -lactamase based on matrix A with different enzyme surface coverages

Biotin- β -lactamase	Enzyme immobilized on SAM/Au substrate			"Free" enzyme in solution
	High	Medium	Low	
Thickness (nm) ^a	1.6	0.8	0.13	
c (nM) ^b	6.98	3.45	0.56	0.3
K_M (10^{-6} M) ^c	1070 ± 340	280 ± 80	120 ± 30	200 ± 20
k_{cat} (s^{-1}) ^d	152 ± 42	90 ± 17	149 ± 20	814 ± 71
k_{cat}/K_M ($10^6 M^{-1} s^{-1}$) ^e	0.14 ± 0.03	0.32 ± 0.06	1.24 ± 0.17	4.07 ± 0.36

The numbers are mean values \pm standard deviation. ^aThickness, obtained from Fresnel simulation. ^bC, the concentration of surface immobilized β -lactamase involved in the catalysis of substrate inside the SPR flow cell. ^c K_M , Michaelis constant, the substrate concentration at which the reaction velocity is half-maximal. ^d k_{cat} , turnover number, the number of reaction events per enzyme molecule and second. ^e k_{cat}/K_M , catalytic efficiency of the enzyme.

The activity of β -lactamase was also tested in solution utilizing the FOAS, the result serving later as a control for the evaluation of the kinetic activity of the surface-immobilized enzymes. For the activity tests in solution, we added 0.3 nM β -lactamase to different concentrations of nitrocefin solutions (8, 12, 20, 28, 40, 70, 80, 120, 160, and 200 μ M) in assay buffer. The mixture was then immediately circulated through the FOAS flow cell while recording the absorbance increase at $\lambda=500$ nm. The flow rate of 1.0 ml/min was applied to all the measurements described above.

The data in Table 3.2 demonstrate that all k_{cat} and k_{cat}/K_M values, corresponding to turnover number and enzyme efficiency, respectively, of surface-immobilized β -lactamase (with high, medium, and low surface coverage) based on matrix A were significantly lower than those of the enzyme in solution using nitrocefin as the substrate. Several factors may contribute in principle to the observed reduction in enzymatic activity, in particular partial denaturation of enzyme upon immobilization and substrate diffusion to the interface. A gradual reduction in the K_M values was observed with decreasing enzyme surface coverage, resulting from the decreased protein surface coverage accelerating the mass transport rate. K_M values of the immobilized β -lactamase with medium and low coverage were similar to that of the enzyme in solution, which shows that for matrix A, diluted surface immobilized enzymes and free enzymes in solution have similar enzyme-substrate affinities. In conjunction with the fact that the k_{cat} values, which indicate the ability of product formation and release from the active site, of surface immobilized enzymes with different binding densities are quite similar, we confirmed that the observed reduced enzymatic activity for surface attached enzymes was mainly due to the steric crowding effect of the enzymes and the resulting limited substrate diffusion.

The next set of comparison (cf. Table 3.3) was made between matrices B, C, D, and E, which were assembled on the basis of PLL-g-PEG/PEG-Biotin. Results listed in Table 3.3 show that the K_M values, which indicate the enzyme-substrate affinities, of β -lactamase immobilized on the four types of matrices were all higher than that of the “free” enzyme in

solution using nitrocefin as the substrate. Together with the observed lower k_{cat} and k_{cat}/K_M values, corresponding to the turnover number and enzyme efficiency, respectively, for surface-immobilized enzymes, we conclude that enzymatic activity for surface-immobilized β -lactamase is reduced compared to “free” enzymes in solution. Furthermore, a gradual reduction in the K_M and increase in k_{cat}/K_M values were observed with decreasing enzyme surface coverage, resulting from the decreased protein surface coverage accelerating the mass transport rate, which is consistent with the comparison of catalytic activity of β -lactamase based on matrix A with different surface coverage (see previous paragraph). Another possible factor that contributes to the higher K_M value with higher surface coverage of enzyme, which further indicates a higher surface coverage of PLL-g-PEG/PEG-biotin, is the electrostatic interaction between the negatively charged substrate (Nitrocefin) and the polycationic PLL-g-PEG/PEG-biotin polymer, which attracts a large amount of substrate (nitrocefin) to the polymer surface, however, not to the enzyme action pocket. The higher the density of polymer, the higher the substrate concentration required to achieve half of the maximum velocity, which indicates the K_M value. Compared to the previous results that k_{cat} values of surface immobilized enzymes based on matrix A with different binding densities are quite similar, a different trend of k_{cat} value was obtained for matrices assembled on the basis of polymers with lower k_{cat} value, which indicate the ability of product formation and release from the active site, accompanied with higher surface coverage of enzyme. The separate processes of enzyme catalysis within the SPR flow cell and the absorbance detection in the FOAS flow cell determined that mass transport play a very important role in the observation of substrate turnover, which was supported by the results that higher working flow rate generated by the peristaltic pump increased the initial reaction velocities of the change in absorbance based on matrix B (detail not shown). Different from the 2-D planar system of matrix A, the 3-D architecture of PLL-g-PEG/PEG-Biotin polymer will largely influence the mass transport process of the product. Higher density of polymer contributes to a more complex 3-D system, resulting in a lower velocity of mass transport and k_{cat} values.

Table 3.3: Surface coverage determined by SPR of biotin- β -lactamase immobilized on gold-coated chips with the four different interfacial matrices (B-E, see Fig. 3.2), and kinetic parameters of the enzymatic turnover of Nitrocefin by surface-immobilized β -lactamase and by the “free” enzyme in solution, obtained from miniature Fiber Optic Absorbance spectroscopy (FOAS) .

	Type of interfacial matrix				Enzyme in solution
	(B)	(C)	(D)	(E)	
	Carboxyl terminated SAM	Nb ₂ O ₅	SiO ₂	Carboxyl terminated SAM (NHS)	
Enzyme surface coverage (ng/cm ²)	52.0	42.4	19.3	9.0	
C (nM)	5.17	4.27	1.94	0.91	
K _M (10 ⁻⁶ ·M)	820 ± 270	730 ± 90	560 ± 110	500 ± 130	200 ± 20
k _{cat} (s ⁻¹)	187 ± 53	212 ± 22	374 ± 59	533 ± 108	814 ± 71
k _{cat} /K _M (10 ⁶ ·M ⁻¹ s ⁻¹)	0.23 ± 0.07	0.29 ± 0.03	0.67 ± 0.11	1.07 ± 0.21	4.07 ± 0.36

In order to compare enzyme catalytic activities based on both 2-D and 3-D matrices, similar surface coverage of enzymes should be applied to minimize the influence of the steric crowding effect of the enzyme. As a result, kinetic parameters of enzymes immobilized on matrix A with the medium surface coverage of 0.8 nm (34.3 ng/cm²) were compared to matrices C and D, which have similar amount of enzyme bound (cf. Figure 3.7 (1)). As shown in Figure 3.7 (2), increased K_M values were observed for 3-D matrices (matrix C and D), owing to the electrostatic interaction between substrate (nitrocefin) and polycationic PLL-g-PEG/PEG-biotin polymer of the planar matrix, as described above, compared to matrix A. Higher k_{cat} values were found for matrices C and D (cf. Figure 3.7 (3)), resulting from the relatively free orientation of surface-immobilized enzymes compared to the planar matrix. For the adsorption event between substrates (nitrocefin) in solution phase and the tethered enzymes at the surface, the substrate is free to sample all orientations in 3-D space to adopt the correct geometry for binding. As a result, enzymes attached to 3-D matrices (matrices C and D) are more likely to react as “free” enzymes in solution, which contributes to a higher k_{cat} value compared to 2-D matrix (matrix A). Combined with the significant influence of mass transport on k_{cat} values as described above, k_{cat} value of matrix E with the lowest surface coverage of β -lactamase as well as PLL-g-PEG/PEG-Biotin polymer is the closest to that of “free” enzymes in solution (results

shown in Table 3.3). As a consequence of the patterns of K_M and k_{cat} values, the change of k_{cat}/K_M values (cf. Figure 3.7 (4)) shows the same trend as the surface coverage of enzymes (cf. Figure 3.7 (1)).

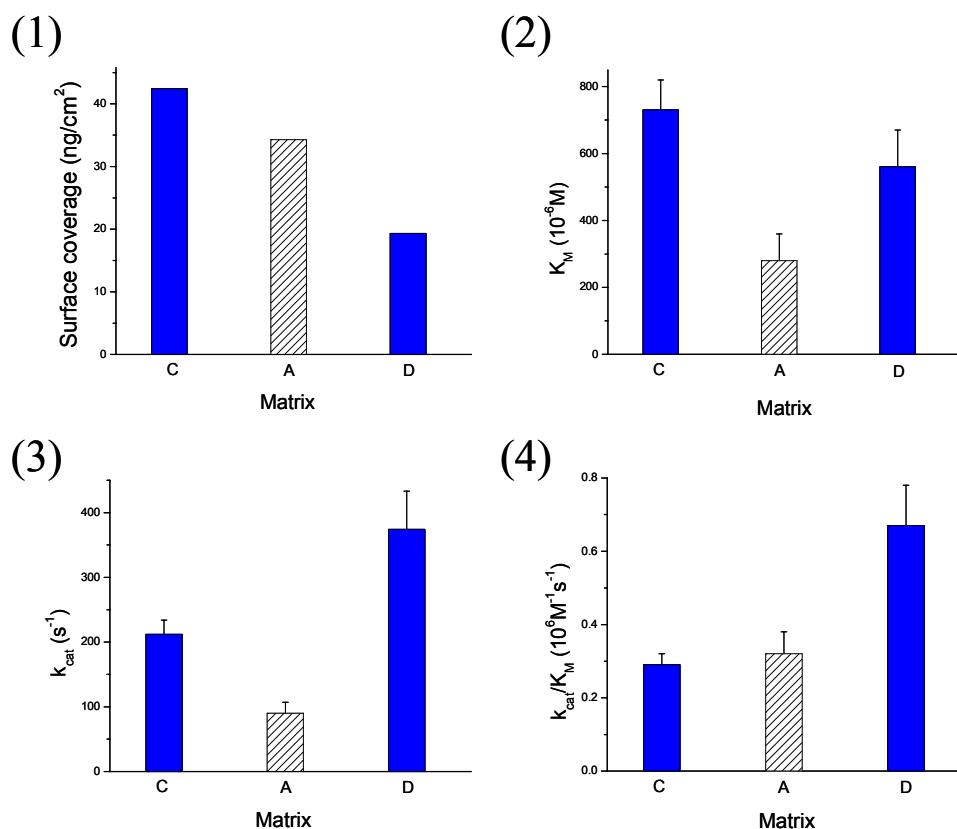


Figure 3.7: Comparison of (1) surface coverage; (2) K_M ; (3) k_{cat} ; (4) k_{cat}/K_M values between matrices based on PLL-g-PEG/PEG-Biotin (matrices C and D) and biotinylated SAMs with medium surface coverage of β -lactamase.

3.8 Conclusion

The aim of this work was to develop a class of interfaces based on the biotin-NeutrAvidin binding matrix for the quantitative control of enzyme surface coverage and activity. Genetically modified β -lactamase was chosen as model enzyme and attached to five different types of NeutrAvidin-functionalized chip surfaces through a biotinylated spacer. All matrices are

suitable for achieving a controlled enzyme surface density. Data obtained by SPR are in excellent agreement with those derived from optical waveguide measurements. Differences were found for the protein-binding strategies investigated in this study, with differences in stiffness and order between alkanethiol-based SAMs and PEGylated surfaces being considered to be important. Matrix D based on a Nb₂O₅ coating showed a satisfactory regeneration possibility. The surface-immobilized enzymes were found to be stable and active enough for a catalytic activity assay. Many factors, such as the steric crowding effect of surface-attached enzymes, the electrostatic interaction between the negatively charged substrate (Nitrocefin) and the polycationic PLL-g-PEG/PEG-Biotin polymer, mass transport effect, and enzyme orientation, may influence the kinetic parameters of catalytic analysis.

Furthermore, there are a number of advantages for the combination of SPR and FOAS techniques. The parallel measurement offers the opportunity of on-line activity detection for surface attached enzymes. The immobilized enzyme does not have to be in contact with the catalytic biosensor. The SPR chip can easily be cleaned and used for recycling. Additionally, with regard to the application of FOAS, the integrated SPR technique allows for the quantitative control of the surface density of the enzyme, which is highly relevant for the enzymatic activity. Finally, the miniaturized portable FOAS devices can easily be combined as an add-on device with many other in situ interfacial detection techniques, such as optical waveguide lightmode spectroscopy (OWLS), quartz crystal microbalance (QCM) measurements, or impedance spectroscopy (IS).

4 Quantification of DNA hybridization based on organometallic chemical vapor deposition (OMCVD) gold particles

4.1 Introduction

The utility of nanoscale curved surfaces such as those provided by metal colloidal particles such as gold, silver and CdS as versatile and efficient templates in the immobilization of biomolecules for immunoassays has been recognized in the early 1980s.¹¹⁸ The high surface-to-volume ratio offered by colloidal particles results in the concentration of the immobilized entity being considerably higher than that afforded by protocols based on immobilization on planar, 2D surfaces. Gold nanoparticles are the most stable metal nanoparticles, and present fascinating aspects such as their assembly of multiple types involving materials science, the behavior of the individual particles, size-related electronic, magnetic and optical properties (quantum size effect), and their applications to catalysis and biology.¹¹⁹ The reasons for the present excitement in gold nanoparticle research are also the extraordinary diversity of their modes of preparations (including biosynthetic modes and template synthesis) involving ceramics, glasses, polymers, ligands, surfaces, films, oxides, zeolites, biomolecules, and bioorganisms.

Chemical Vapour Deposition (CVD) of films and coatings involve the chemical reactions of gaseous reactants on or near the vicinity of a heated substrate surface. This atomistic deposition method can provide highly pure materials with structural control at atomic or nanometer scale level. Moreover, it can produce single layer, multilayer, composite, nanostructured, and functionally graded coating materials with well controlled dimension and unique structure at low processing temperatures. Furthermore, the unique feature of CVD over other deposition techniques such as the non-line-of-sight-deposition capability has allowed the coating of complex shape engineering components and the fabrication of nano-devices, carbon-carbon (C-C) composites, ceramic matrix composite (CMCs), free standing shape components. The versatility of CVD had led to rapid growth and it has become one of the main processing methods for the deposition of thin films and coatings for a wide range of applications, including semiconductors (e.g. Si, Ge, Si_{1-x}Ge_x, III-V, II-VI) for microelectronics, optoelectronics,

energy conversion devices; dielectrics (e.g. SiO₂, AlN, Si₃N₄) for microelectronics; refractory ceramic materials (e.g. SiC, TiN, TiB₂, Al₂O₃, BN, MoSi₂, ZrO₂) used for hard coatings, protection against corrosion, oxidation or as diffusion barriers; metallic films (e.g. W, Mo, Al, Au, Cu, Pt) for microelectronics and for protective coatings; fibre production (e.g. B and SiC monofilament fibres) and fibre coating.¹²⁰ The preparation of gold microstructures via organometallic chemical vapor deposition (OMCVD) on patterned SAMs is possible because of the selectivity of the gold source towards surface thiol groups. Gold is only selectively deposited where thiol functions are available. The gold concentration on top of the thiol functionalized surface can be well controlled by the exposure time and the pressure. The binding of additional thiolated functional molecules on top of the deposited gold, probably forming a second SAM structure, was successful.

Excellent sensory and environmental devices are becoming available by tuning the spectroscopy, fluorescence, luminescence, and electrochemical characteristics of gold nanoparticles with those of substrates including DNA, sugars, and other biological molecules or systems. In particular, DNA is a candidate for this task because of its excellent specificity in base pairing, and it can be easily addressed at the nanoscale for applications in biosensing and bionanotechnology.¹¹⁹ Conjugates of gold nanoparticles-oligonucleotides are of great current interest because of the potential use of the programmability of DNA base-pairing to organize nanocrystals in space and the multiple ways of providing a signature for the detection of precise DNA sequences. Nanoparticles attached DNA retains its ability to hybridize with complementary DNA, and the annealing process was thermally reversible and nondestructive. Applications in the fields of biosensors, disease diagnosis, and gene expression are clearly called for. Many efforts have been made to follow the hybridization process of DNA by developing sensitive colorimetric methods due to the color change^{43;57}, and electrodynamic calculations during the gold nanoparticles aggregation in solution¹²¹. From a more fundamental point of view in surface science, the hybridization event happened on the surface is an interesting example of how surface functionality depends on the (supra-) molecular organization of the reaction partners involved, one being immobilized at the surface, the other approaching freely from the aqueous phase. The efficiency and the kinetics of hybridization reactions depend on many factors like the ionic strength of the buffer, the temperature, the pH value, the length of the nucleotide sequence, the G-C to A-T ratio, the degree of mismatch, to

name but the most important ones. For a surface confined base pairing leading to hybridization, additional factors like steric accessibility, orientational constraints, mass transfer from the bulk to the interface, etc., play an important role and control stability and reaction kinetics of this binding event.¹²²

4.2 Materials

The thiol derivatives (Figure 4.1 (A) and (B))¹¹⁰ and Tri-n-butylphosphine (TBP) were dissolved in ethanol at a concentration of 5mM. Streptavidin, obtained from Roche Diagnostics, was dissolved in PBS buffer (10 mM phosphate buffer, 2.7 mM KCl, 150 mM NaCl, pH 7.4) at a concentration of 0.5µM. DNA probes, biotinylated at one end in order to couple them to the streptavidin matrix, are fully matching to a complementary DNA target sequence, which is labeled with Cy3 at one end. The probes and targets, with the structures given in Figure 4.1 (C), (D), and (E), were purchased from MWG GmbH, and dissolved in PBST (10 mM phosphate buffer, 2.7 mM KCl, 150 mM NaCl, 0.005% Tween 20, pH 7.4) at concentrations of 100nM and 50nM respectively. All other reagents were purchased from Sigma-Aldrich, Germany. Buffers were prepared using ultrapure water (18MΩ·cm).

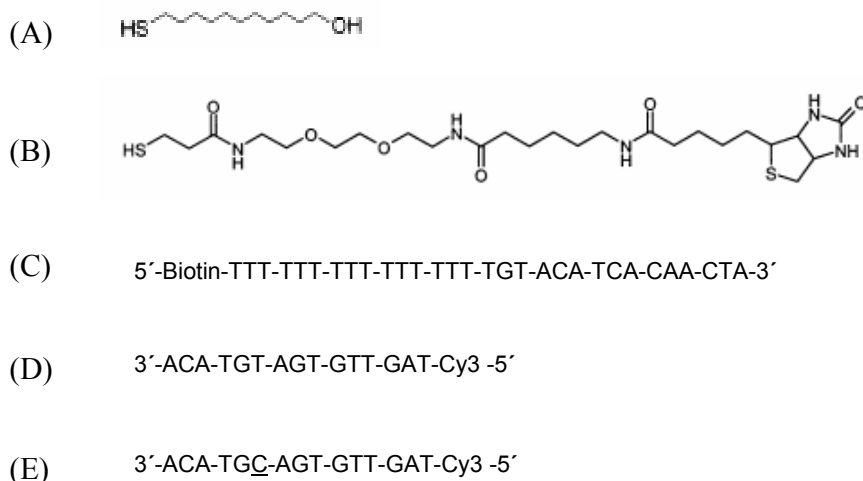


Figure 4.1 Structure formulas of (A) hydroxyl-terminated thiol and (B) biotin-terminated thiol, employed for the preparation of Self-assembled Monolayers (SAMs). (C): The base sequence of the employed probe

oligonucleotides (P2) with 15 thymine spacer units and the biotin-coupling group at the 5' end. (D): The corresponding 15-mer fully complementary DNA target (T2) carries the fluorophore Cy3 at their 5' end. (D): The corresponding 15-mer mismatch 1 DNA target (T1) carries the fluorophore Cy3 at their 5' end.

Organometallic chemical vapor deposition (OMCVD) gold particles, provided by Anne Kathrena A. Aliganga and Silvia Mittler (Department of Physics and Astronomy, The University of Western Ontario, London, Ontario, Canada), were prepared with the extinction maximum at $\lambda = 520\text{-}530$ nm (cf. Figure 4.2), surface coverage of 2×10^{17} gold atoms / cm^2 , and a mean lateral size of 12 nm (cf. Figure 4.3).

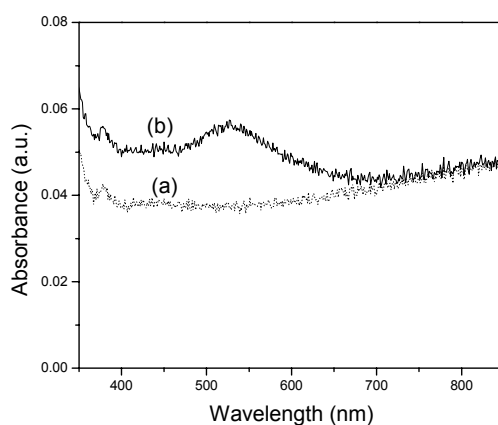


Figure 4.2: UV-Vis spectra of (a) MPTS SAMs and of the (b) OMCVD gold nanoparticles on MPTS SAMs.

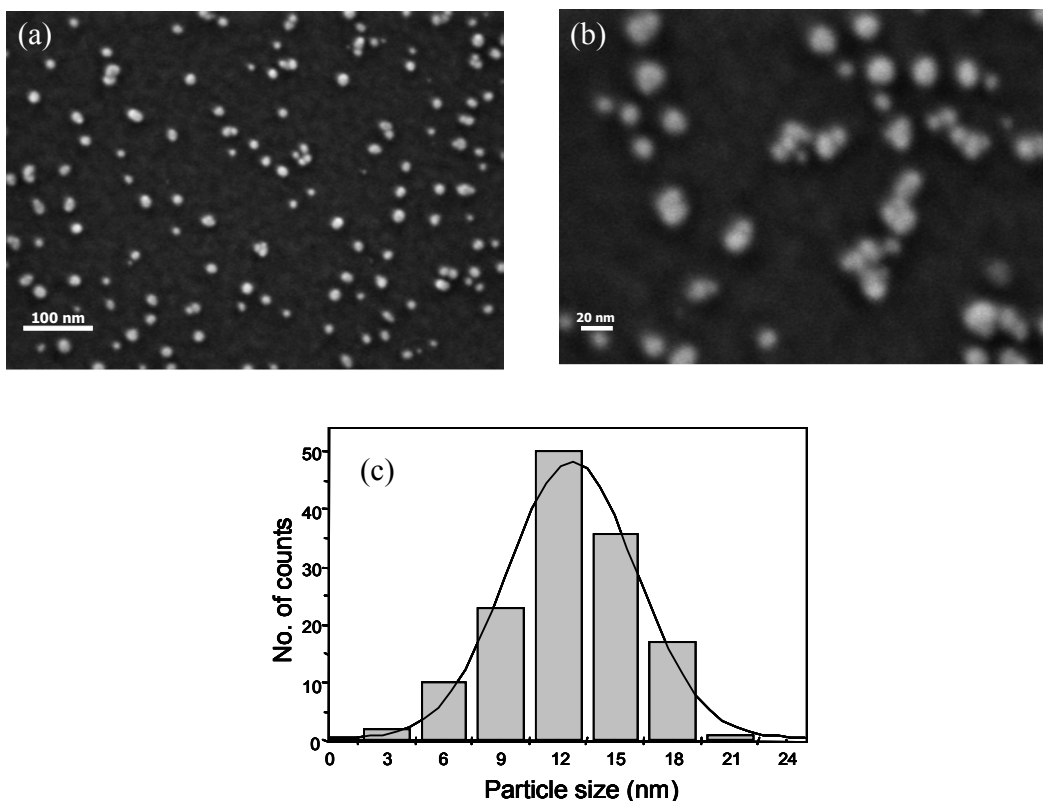


Figure 4.3: (a) SEM images of OMCVD gold on MPTS. (b) Zoom-in of (a). (c) Size distribution of OMCVD gold (using a sample of 150 particles).

Plotting the peak wavelength against deposition time gave us a trend that is consistent with the theoretical schematic dependence of position of the dipolar surface plasmon resonance for metal clusters as a function of cluster size.¹²³⁻¹²⁵ Figure 4.4 shows qualitatively the direct relationship of the increasing OMCVD deposition time and the increase in lateral size and amount of the gold nanoparticles formed being a function of the position of the plasmon resonance. The theoretical scheme supports the shifts observed in the plot of the peak wavelength that is, due to electrodynamic effects, which is due to phase retardation of the electromagnetic waves and the influence of higher multipoles, and the effects of the clustered material.

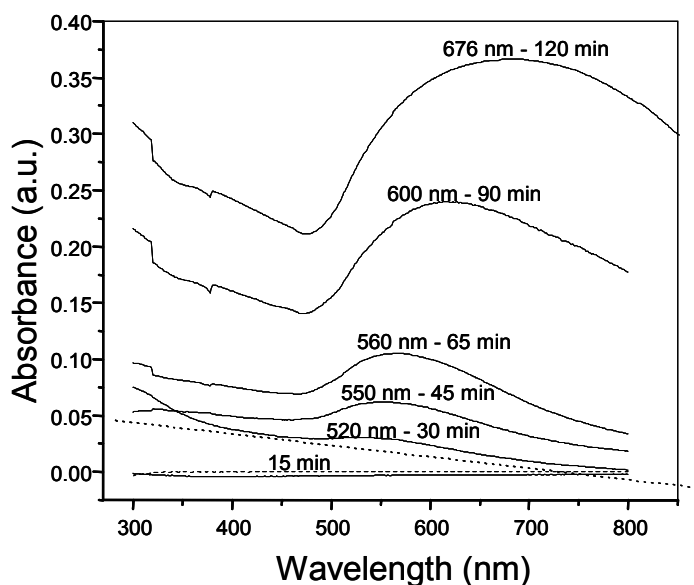


Figure 4.4: UV-Vis spectra of OMCVD gold at different reaction times. The first straight line refers to MPS SAMs without the OMCVD gold.

4.3 Methods

In our study, hybridization of DNA target strands from solution to surface-attached biotinylated DNA probes were investigated based on both planar and OMCVD gold particle matrices as a comparison. The surface modification for DNA catcher matrix based on a planar matrix (cf. cartoon in Figure 4.5 (C1)) was performed using LaSFN9 slides (Schott, $n=1.85$ at $\lambda = 633\text{nm}$) as a substrate. The slides were carefully cleaned and coated in turn with 40nm of Silver (Ag), and 5nm gold (Au) on top by thermal evaporation in a commercial instrument (Edwards). The freshly coated Ag/Au substrates were immersed in the solutions of a binary thiol mixture solution containing 10 mol% of the biotin-terminated thiol and 90mol% of the hydroxy-terminated diluent thiol, then sealed, and kept overnight at room temperature. The mixed thiol solution was prepared at a net thiol concentration of $c= 357 \mu\text{M}$ in absolute ethanol (99%). Subsequently, the substrates were removed, rinsed thoroughly with ethanol, and blown dry by a stream of nitrogen. The prepared substrates were used immediately after preparation. The biotin-terminated self-assembled monolayers (SAMs) allowed for the binding of

Streptavidin during 30min and further attachment of 100nM biotinylated DNA probe (P2, structure formula shown in Figure 4.1 C) during 30min as well. The attachment of the catcher probe strand via a biotin-group at the 5' end of an additional 15mer of thymines used as spacers, ensures a separation of the chromophores beyond 2 Förster radii, thus preventing any significant loss of fluorescence signal due to energy transfer to the (acceptor states of the) metal (quenching).¹²² The same assembly protocols of planar matrix as described above were applied to the particle interfacial matrix (cf. cartoon in Figure 4.5 (C2)), except that the OMCVD gold particle coated slides were immersed in the mixture solution of 10 mol% of the biotin-terminated thiol, 90mol% of the hydroxy-terminated diluent thiol, and 70 μ M Tri-n-butylphosphine (TBP) for the formation of biotinylated SAMs. The presence of TBP in the self-assembly solution prevented the formation of disulfate bonds between the exposed mercaptosilane SAMs on the chip and thiol molecules in the solution, but has no influence on the overall kinetics of the chemisorption of the thiols on the metal surface.¹²⁶

Subsequently, the hybridization of 50nM DNA target strands (T1 or T2, structure formulas shown in Figure 4.1 D and E, respectively) from solution to surface-attached biotinylated DNA probes were performed. The target sequence of T2 matches completely to its corresponding probe (P2) sequence for the mismatch 0 (MM0) hybridization. However, DNA target T1 differs from T2 in one base (cf. the underlined base in the schematic of Figure 4.1 E) resulting in mismatch 1 (MM1) situation upon the cross-hybridization of T1 with P2. For certain applications, methods to detect the presence of the defined DNA sequence is realized by the simple optical means based on the contrast of transmission or reflection images.¹²⁷ In this study, Surface plasmon resonance spectroscopy (SPFS), which is based on a home-built surface plasmon spectrometer and described in detail elsewhere,¹²⁸ was utilized as optical detection scheme. Supplementary to the normal SPR setup, the fluorescence emission of the sample is collected from the backside of the prism by a lens and passes through an interference filter ($\lambda=620\text{nm}$ for the laser wavelength of $\lambda=543\text{nm}$) into a photomultiplier tube, which is connected to a photon counter unit. SPFS allows for the simultaneous recording of reflectivity, as well as the fluorescence intensity data, either as a function of incident angle, θ , or as a function of time in the kinetic mode. The evanescent field of a surface plasmon is enhanced compared to the incident field, and then decays exponentially into the dielectric medium, with the decay length of the surface plasmon in the range of ca. 200 nm. The evanescent character of

the surface plasmon mode leads to an excitation probability that is exponentially decaying away from the interface.

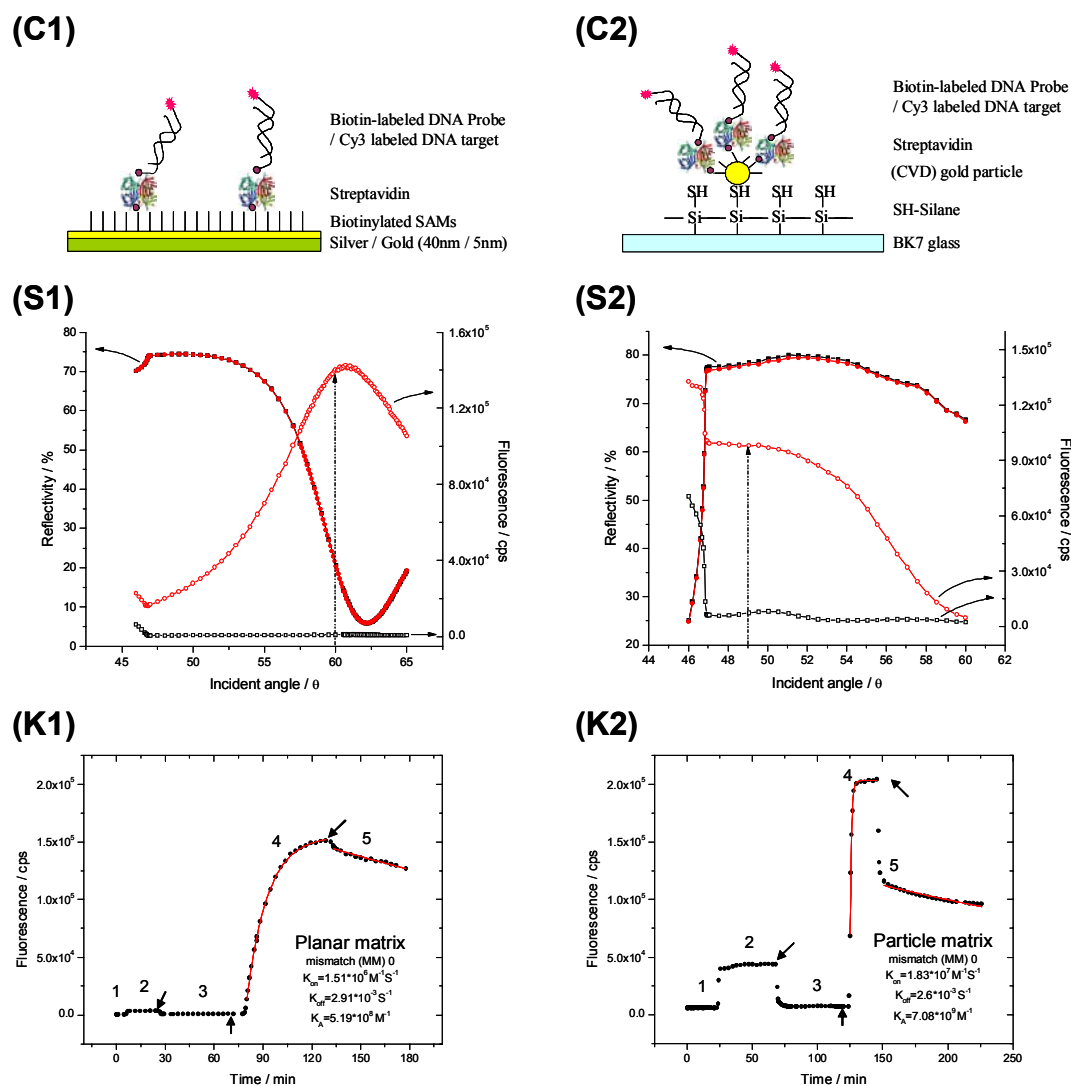


Figure 4.5: (C1) and (C2): Cartoon of planar propagating surface plasmons (PSPs) and particle localized surface plasmons (LSPs) interfacial multilayer matrices, respectively. (S1) and (S2): Angular reflected intensity scans (closed symbols) before (!) and after (,) the hybridization of DNA target (T2) from solution to the surface attached DNA probe (P2), as well as the simultaneously measured fluorescence intensities (open symbols) as a comparison between the background signal (∇) and the signals of taken after the specifically binding of DNA probe and fully complementary target ($-$) (MM0) for different interfacial architectures (cf. (S1): PSPs matrix; (S2): LSPs matrix) detected by SPFS with the incident wavelength of 543nm. Arrows show the fixed incident angle position, 60° and 49° for kinetic measurements for PSPs and LSPs matrices, respectively. (K1) and (K2): kinetic fluorescence scans (black dotted line) taken for hybridization (non-specific binding, association, and dissociation) processes between the surface oligonucleotide (P2) and T2 (mismatch0) target complements from solution. Arrows show the rinsing

steps with pure buffer. The red full curves are theoretical calculations based on langmuir association / dissociation model, with rate constants, adsorption (hybridization) rate constant, K_{on} ; dissociation rate constant, K_{off} ; affinity constant, $K_A=K_{on}/K_{off}$, given beside the curves. 1, 2, 3, 4, and 5 represent the binding protocols of streptavidin modified surface, Non-specific binding of T2, P2 attachment, T2 association, and T2 dissociation processes, respectively.

In earlier experiments SPFS has been shown to allow for the characterization of the interaction of oligonucleotides onto matrices based on propagating surface plasmons with high sensitivity and reliability, and quantitative evaluation of the association (hybridization) and dissociation process of targets binding from solution with k_{on} and k_{off} values that were coverage-independent and represented the individual binding process well described by a simple Langmuir model.¹²² In this study, real time detection of DNA hybridization on matrices based on both planar propagating surface plasmons (PSPs) and localized surface plasmons (LSPs) of 3-dimentional OMCVD gold particles were performed with the SPFS excitation wavelength of $\lambda = 543\text{nm}$, which matches (approximately) the plasmon resonance band of OMCVD gold particles. Meanwhile, the fluorescence labeling of DNA target has to be selected so as to allow for an efficient excitation by the laser source. As a result, 5' end Cy3 ($\lambda_{abs}= 550\text{ nm}$, $\lambda_{emi}= 570\text{ nm}$) labeled DNA target was used, however, with the interference filter wavelength of $\lambda=620\text{nm}$ to avoid the adjacent signal collection of the emission and excitation light ($\lambda=543\text{nm}$) in order to decrease the fluorescence background signal.

4.4 Comparative quantification of DNA hybridization based on planar and gold particle matrices

Two groups of reflectance together with fluorescence intensity angular scans for planar PSPs and particle LSPs matrices are shown in Figure 4.5 (S1 and S2), respectively. The reflectivity (closed symbols) and fluorescence intensity (open symbols) scans were taken prior to and after the association process of fully complementary DNA target (T2) in solution to surface immobilized DNA probe (P2), followed by a dissociation process initiated by a short rinsing step. As respect to planar PSPs matrix (schematically shown in Figure 4.5 (C1)), barely any change of the reflected intensity can be detected, indicating the lack of sensitivity of the bare surface plasmon spectroscopic detection scheme. However, the experimental situation is

fundamentally different if we monitor the fluorescence intensity emitted from this interface originating from the chromophores attached to the DNA target complement. The fluorescence intensity, when measured before the addition of the (labeled) DNA target T2 shows only the flat angle-independent background. After the complement binding, however, a strong fluorescence signal, which shows the angle-dependent expected for propagating surface plasmon field excitation, can be detected. In this case, the enhanced optical field of a resonantly excited surface plasmon mode is exploited as the illumination “light source” for the fluorophores.

Compared to the planar PSPs matrix, the particle LSPs matrix (schematically shown in Figure 4.5 (C2)) shows totally different SPFS angular scans (cf. Figure 4.5 (S2)). The reflectance curves exhibit the typical total internal reflection (TIR) behavior. Below a certain critical angle (47°) which is given by Snellius’ law, i.e. by the refractive indices of the solid and the liquid, respectively, most of the light is transmitted and hence the reflectivity is very low. As we approach the critical angle, however, the reflectivity steeply increases and reaches the maximum at the critical angle. The slightly decreased reflectance above the critical angle mainly attribute to the light extinction effect of the surface-spread gold particles and the refractive index mismatch presented between the coupling prism and the glass substrate ($n=1.52$ at $\lambda = 633\text{nm}$). These influences break the continuity of the reflectance spectrum. Results show that the OMCVD gold particles, with a mean lateral size of 12 nm and surface coverage of 2×10^{17} gold atoms / cm^2 , did not modify the angular scan curves of glass/aqueous medium. Furthermore, the hybridization of DNA target (T2) from solution to the surface-bound probe (P2) did not contribute any detectable signal for the reflectance curve. However, if the binding molecules carry a chromophore, an evanescent field created by totally internal reflection of laser beam can be used to excite this optical label and the resulting fluorescence can be monitored with high sensitivities, which realizes a quantitative measurement of the biomolecular interaction in-situ and in real-time. Additionally, the interaction of fluorophores with the localized surface plasmons generated from metallic particles will also influence the fluorescence signal. As a comparison between the background signal (cf. open black curve in Figure 4.5 (S2)) and the signals taken after the specifically binding of DNA probe and fully complementary target (cf. open red curve in Figure 4.5 (S2)), the fluorescence intensity below the critical angle is rather high because the transmitted incident light was utilized as the

excitation source of the surface-bound fluorophores labeled on the target (T2). The fluorophores are excited by the evanescent field of the interface light if we approach the critical angle. There is a moderate enhancement of the interface light intensity at the critical angle which originates from the constructive interference of the two amplitudes of the incoming and reflected electromagnetic field.¹²⁸ Above the critical angle, the light intensity at the interface decreases and results in the decrease of fluorescence intensity. The fluorescence intensity can also be modified by the excitation of localized surface plasmons resonance, which will be discussed later.

In order to quantitatively evaluate the association (hybridization) and dissociation process of DNA target from solution to the probes on the surface, kinetic experiments were taken for planar (cf. Figure 4.5 (K1)) and particle (cf. Figure 4.5 (K2)) matrices. Such kinetic runs are typically recorded by monitoring the fluorescence signal at a fixed angle of observation. One can select this angle of observation within the most sensitive detection region thus guaranteeing a near linear relation between the observed fluorescence intensity change and the angular fluorescence enhancement. As a result, 60° and 49° were chosen as the fixed incident angle position for kinetic measurements for PSPs and LSPs matrices, respectively. Once the background fluorescence signal was recorded for a few minutes, non-specific binding (NSB) of DNA target was performed by injecting 50nM Cy3 labeled DNA target (T2) to both the planar and particle substrates, however, without the surface-bound DNA probe. Shown in the working curve, no detectable fluorescence signal remains in the system after a rinsing step, indicating that there is no NSB of DNA target on both planar and particle matrices. One phenomenon to note is the higher target NSB (background) signal (cf. Step 2 in Figure 4.5 (K1) and (K2)) for particle matrix compared to planar matrix. Subsequently, 100nM biotin labeled DNA probe (P2) was injected to the streptavidin coated surface and coupled to the binding matrix via the specific recognition of its biotin moieties. The association process of DNA hybridization was initiated by adding 50nM Cy3 labeled DNA target (T2) to the DNA probe-attached surface and the increase in fluorescence intensity was measured as a function of time until the equilibrium between the bulk concentration and the corresponding surface coverage was reached. Upon the addition of T2 solution to the planar matrix (cf. Figure 4.5 (K1)), the fluorescence intensity rises very rapidly. The reversibility of this surface binding was tested by injecting pure buffer through the system. A small instant decrease of the fluorescence intensity is followed by a

gradual decrease in intensity corresponding to the dissociation of target strands from the surface-bound probe DNA. However, if T2 solution was added to the particle matrix (cf. Figure 4.5 (K2)), the fluorescence intensity rises even faster than that of planar matrix due to the fast association rate and rather high non-specific binding (NSB) signal (described above) of DNA target to the surface, and reached a stable constant value. Rinsing with pure buffer triggered firstly a fast fluorescence decrease attribute to the rinsing of NSB target out of the surface, and later a very slow decrease of fluorescence intensity with time. The red full curves in Figure 4.5 (K1) and (K2) are theoretical calculations based on a Langmuir association/dissociation (pseudo-single-exponential kinetic) model, with values of two reaction rate constants, k_{on} and k_{off} describing the whole process, as well as, the affinity constant ($K_A = k_{on} / k_{off}$) indicated beside the curves for both interfacial matrices, respectively. As respect to the particle matrices for both MM0 and MM1 hybridization (to be described later), the kinetic curves were fitted avoiding the first several data points due to the high level of background signal for both the association and dissociation processes. If we compare the rate constants for the planar and particle matrices, we find that the K_A of particle matrix (7.08×10^9) is more than 13 times of that of the planar matrix (5.19×10^8), resulting from the higher k_{on} and lower k_{off} values for particle matrix. The three-dimensional gold particle interfacial architecture with larger aspect ratios provides a faster and more forceful DNA hybridization process of target from solution to the probe-immobilized surface, which contributes to a higher affinity constant compared to the two-dimensional metal film matrix with smaller aspect ratios.

4.5 Non-specific binding of DNA on a OMCVD gold particle matrix

A negative control measurement was performed for the DNA hybridization on bare mercaptosilane SAMs substrate before the OMCVD of gold particles (kinetic curve and cartoon shown in Figure 4.6 (A)). Slides were immersed in the solution of 10 mol% of the biotin-terminated thiol, 90mol% of the hydroxy-terminated diluent thiol, and 70 μ M Tri-n-butylphosphine (TBP). The formation of biotinylated SAMs was forbidden because of both the lack of gold particles and the presence of TBP. After repeating the same procedures (mentioned in detail in 4.3) for streptavidin and P2 attachment, DNA target (T2) was injected to the system. The totally rinsed-back fluorescence signal indicates the absence of DNA catcher matrix on the

substrate and further illuminates the specific association process from DNA targets in solution to their complementary surface-attached probes. If we compare the NSB (background) signals of target injection for both the mercaptosilane SAMs (cf. Step 4 in Figure 4.6 (A)) and OMCVD gold particle (cf. Step 2 in Figure 4.6 (B) and (C)) coated substrates, similar fluorescence intensities were obtained indicating that the OMCVD gold particles has negligible effect on the modification of the fluorescence signal of the non-specifically bound fluorophores.

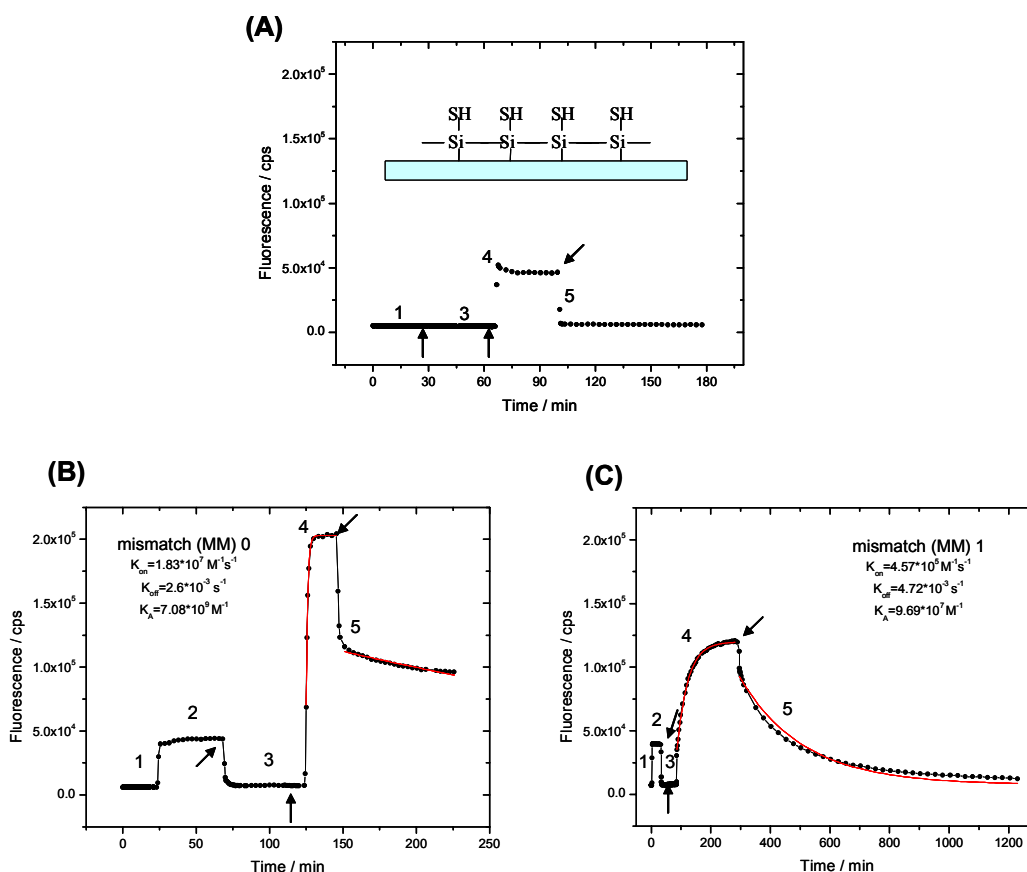


Figure 4.6: (A): Schematic representation and fluorescence kinetic measurement of the binding process of DNA target (T2) on the mercaptosilane SAMs system (without the OMCVD of gold particles). (B): kinetic fluorescence scans (black curve) taken for mismatch0 (MM0) hybridization (non-specific-binding, association, and dissociation) processes between the probe (P2) oligonucleotide surface and fully complementary DNA target complements (T2) from the solution. (C): kinetic fluorescence measurement (black curve) for mismatch1 (MM1) hybridization between P2 and T1. Arrows show the rinsing steps with pure buffer. The red full curves in (B) and (C) are theoretical calculations based on Langmuir association / dissociation model, with rate constants, adsorption (hybridization) rate constant, K_{on} ; dissociation rate constant, K_{off} ; affinity constant, $K_A = K_{on}/K_{off}$, given beside the curves. 1, 2, 3, 4, and 5 represent the binding protocol of streptavidin modified surface, Non-specific binding of DNA target (T2 for (B) and T1 for (C)), P2 attachment, association, and dissociation processes of DNA target (T2 for (A) and (B); T1 for (C)), respectively.

4.6 Sequence-specific detection of DNA hybridization based on OMCVD gold particles

Figure 4.6 (B) and (C) summarize two experiments that were all performed with the P2-probe oligonucleotide particle matrix but with two different target strands, T2 and T1, representing MM0 and MM1 situations, respectively. The target complement concentrations applied were all $c_0=5\times 10^{-8}$ M. A remarkably different behavior is found for the P2 / T1 hybridization, i.e. a MM1 experiment (cf. Figure 4.6 (C)) compared to the MM0 case (cf. Figure 4.6 (B)) as described above. Upon the addition of the labeled complement (T1) solution, the fluorescence rises to more than half of the fluorescence intensity level as MM0 case, and reached a stable constant value with a considerably reduced binding rate constant. However, if the complement solution is replaced by pure buffer, the fluorescence signal gradually decreases with time until after several hours no intensity can be detected any more. The red full curves in Figure 4.6 (B) and (C) are theoretical calculations based on a Langmuir association/dissociation model, with values of two reaction rate constants, k_{on} , k_{off} , and the affinity constant (K_A) indicated beside the curves for both measurements. If we now compare the rate constants for the hybridization of the target sequences T2 and T1 to the probe strand P2 at the sensor surface, we see the expected behavior, i.e. with increasing mismatch the association rate constant k_{on} decreases from 1.83×10^7 $M^{-1}s^{-1}$ to 4.57×10^5 $M^{-1}s^{-1}$, whereas the dissociation rate constant k_{off} increases from 2.6×10^{-3} s^{-1} to 4.72×10^{-3} s^{-1} . This then adds up to the finding that the affinity constant K_A drops from 7.08×10^9 M^{-1} for the MM0 situation to 9.7×10^7 M^{-1} by almost two orders of magnitude if only a single base (out of 15) is replaced in the complement strand resulting in a single mismatch.

4.7 Conclusion and outlook

In this study, SPFS allows for an absolute determination of intrinsic rate constants describing the true parameters that control interfacial hybridization, and thus also allows for a study of the surface coupling properties of OMCVD gold particles and planar metal films. The multilayer growth process was found to proceed similarly to the way which occurs on planar metal

substrates. The results of sequence-specific detection of DNA hybridization based on OMCVD gold particles provide an excellent application potential for this kind of cheap, simple, and mild condition required gold fabrication method. Recently, the interactions of fluorophores with metallic particles and surfaces (metals) have been used to obtain increased fluorescence intensities, to develop assays based on fluorescence quenching by gold colloids, and to obtain directional radiation from fluorophores near thin metal films. In contrast to continuous metal surfaces, metal colloids exhibit a strong UV-vis absorption band. This absorption band occurs if the incident photon frequency is resonant with the collective oscillation of the conduction electrons and is known as the localized surface plasmon resonance (LSPR). LSPR excitation results in extremely large molar extinction coefficients, which are due to a combination of both absorption and scattering. When considering metal-enhanced fluorescence we expect the absorption to cause quenching and the scattering to cause enhancement. The relative contribution of absorption and scattering depends on the metal and on the size of the colloids. Small colloids are expected to quench fluorescence because absorption is dominant over scattering. Larger colloids are expected to enhance fluorescence because the scattering component is dominant over absorption. The ability of a metal surface to absorb or reflect light is due to wavenumber matching requirements at the metal-sample interface. The possibility of wavevector matching across a metal/dielectric interface determines whether the plasmons can radiate or are trapped and dissipated as lossy surface waves. The difference between enhanced fluorescence and quenching is the nature of the induced plasmons on the metal surface. In order to get enhanced fluorescence, the radii of particles over 20 and 40 nm is required for silver and gold colloids, respectively.⁴⁴ It is well established that the peak extinction wavelength of the LSPR spectrum is dependent upon the size, shape, and interparticle spacing of the nanoparticle as well as its dielectric properties and those of the local environment.⁴¹ Our further study will focus on the developing of a detection platform with larger gold particles, which will display a dominant scattering component and enhance the fluorescence signal.

5 External stimuli and internal crosslink responses of Carboxymethyl dextran (CMD) for surface plasmon resonance (SPR) applications

5.1 Introduction

For more than a decade, remarkable progress in the development of affinity biosensors and their applications in areas such as environmental monitoring, biotechnology, medical diagnostics, drug screening, food safety, and so on have been developed.¹²⁹ Optical biosensors offer distinctive advantages in terms of miniaturization, low cost, disposability and lack of electrical interference. Various optical methods have been exploited for biosensors including fluorescence spectroscopy,¹³⁰ interferometry (reflectometric white light interferometry¹³¹ and modal interferometry in optical waveguide structures¹³²), spectroscopy of guided modes of optical waveguides (grating coupler¹³³ and resonant mirror¹³⁴), and surface plasmon resonance (SPR).¹¹⁰

Biosensors based on surface plasmon resonance (SPR) have made great strides, and a large number of SPR sensor platforms, biomolecular recognition elements, and measurement formats have been developed. SPR-based optical sensors exploit special electromagnetic waves (surface plasmon polaritons) to probe interactions between an analyte in solution and a biomolecular recognition element immobilized on the sensor surface. In the so-called Kretschmann configuration, a thin metal film is optically coupled to a prism made of a high-refractive-index material. Illumination of the film through this prism under total internal reflection conditions allows then for the excitation of a surface plasmon mode via an evanescent wave. As it is typical for surface-confined modes, the transverse component (perpendicular to the metal surface) of the electric field vector decays exponentially into the dielectric medium from a maximal value at the metal surface. With typical decay lengths being ~200nm (at mid-visible excitation wavelength), surface plasmons are exquisitely sensitive to changes in the properties of the interface. In particular, minor changes of the thickness of a thin coating and/or the refractive index of the medium in contact with the metal film result in a change in the propagation of the surface plasmon mode, and, hence, in the coupling conditions.

SPR biosensors provide numerous advantages. This technique is label-free; no enzyme, fluorophore, or radioisotope labeling is required for detection or amplification of a binding event. SPR can also be performed in real time, thereby allowing for kinetic as well as thermodynamic parameters to be determined. And finally, the technique offers an additional behavior to the Kretschmann “back-side” illumination geometry. The excitation light beam does not have to travel through the sample solution during operation. This decreases any interference, i.e. scattering, that could arise from turbid or strongly absorbing solutions. Despite these advantages, it is still desirable in some applications to use “tagging” strategies to either amplify or differentiate observables in the SPR experiment.¹³⁵ In case of a very dilute lateral packing of the analyte or very small analytes of low molecular mass are to be detected, only very thin effective layers are generated on the sensor surface, eventually resulting in SPR angular shifts, too low to be detected. This then generates severe sensitivity limitations and, as a consequence, the concept of using (fluorescence) label techniques in connection with surface plasmon spectroscopy as a means to enhance the signal of the interfacial binding events are to be considered. Surface plasmon field-enhanced fluorescence spectroscopy (SPFS) is the combination of surface plasmon excitation and fluorescence spectroscopy for sensor applications. The field enhancement at the (noble) metal/dielectric interface could be used very efficiently to excite a chromophore located within the evanescent field, i.e. near the interface. Analytical methods incorporating a labeling technique, on the contrary, are less dependent on the molecular weight of the analyte and can generally provide much higher sensitivity by several orders of magnitude for monitoring binding reactions of an analyte from the aqueous phase to the recognition sites at a functionalized interface, especially for small analytes.¹²⁸

A number of commercial SPR biosensor instruments are available by which the SPR-based detection of biological analytes and the analysis of biomolecular interactions have been greatly promoted. The first commercial SPR was launched by Biacore International AB in 1990. The sensor chip is composed of extended carboxymethyl dextran (CMD) chains. The carboxymethyl groups offer versatile reaction sites to CMD for modifications with bioactive moieties or for chemical crosslinker groups. Since SPR measurements can be compromised by interfering effects of background refractive index variations due to external parameter fluctuations, a good understanding of how the CMD behaves under external perturbations was key to major breakthroughs using in this matrix.

Once crosslinked, the CMD matrix acts as a hydrogel and has the ability of reversibly switching in aqueous solutions between a collapsed and a swollen states in response to environmental changes, e.g., pH and ionic strength.^{136;137} Water-swellaable hydrogel networks can be formed based on the CMD through chemical or physical crosslinks. Once crosslinked, the polymers lose individual identity and become part of a large three-dimensional interconnected network.¹³⁸ Different from the conventional characterization of hydrogel conformation changes by weighing the hydrogel prior to and after the swelling/collapse process, SPR/SPFS offers the opportunity to on-line monitor the whole process.

In this study, effects of surface charge and crosslink density on the swelling/collapse properties of different CMD matrices under external stimuli (pH, ionic strength) fluctuations were investigated in detail.

5.2 Materials

Commercially available carboxymethyl dextran (CMD) chips, with a dextran concentration of 200ng/cm², and a carboxyl group concentration of 1n mole/cm² on the surface, were used. Alexa Fluor 647 hydrazide (Alexa), purchased from Molecular Probes, was firstly dissolved in (DMF) at a concentration of 2mM, then diluted to 2.2μM with 20mM phosphate buffer, pH 7.0. N-ethyl-N'-(dimethylaminopropyl) carbodiimide (EDC), purchased from Sigma-Aldrich and N-hydroxysuccinimide (NHS), obtained from Perbio Science Deutschland GmbH, were individually dissolved in water at a concentration of 75mg/ml and 11.5mg/ml, respectively, and stored in 500μl aliquots at -20°C until use. For pH measurements, HCl or NaOH were used to adjust the buffer solution (1.25mM citric acid, 1.25mM potassium dihydrogenphosphate, 1.25mM sodium tetraborate, 1.25mM tris (hydroxymethyl) aminomethane, and 1.25mM potassium chloride) to the desired pH values. Solutions with different ionic strengths were prepared by adding NaCl to phosphate buffer, pH 7.0. Octanethiol was dissolved in ethanol at a concentration of 5.76mM. Ethylenediamine (EDA) was dissolved in MilliQ at a concentration of 1M. Poly (ethylene glycol) bis (3-aminopropyl) terminated (PEGBA) was dissolved in 20mM phosphate buffer, pH 8.5 at a concentration of 85μM. Glutaraldehyde (GA) was dissolved in water at a concentration of 5%. Toluidine blue O (TBO) was dissolved in water at the desired concentrations, and adjusted to pH=10 with 0.1mM NaOH. All reagents were

purchased from Sigma-Aldrich, Germany. Buffers were prepared using ultrapure water (18M Ω ·cm).

5.3 Stimuli responses of CMD characterized from SPR simulation

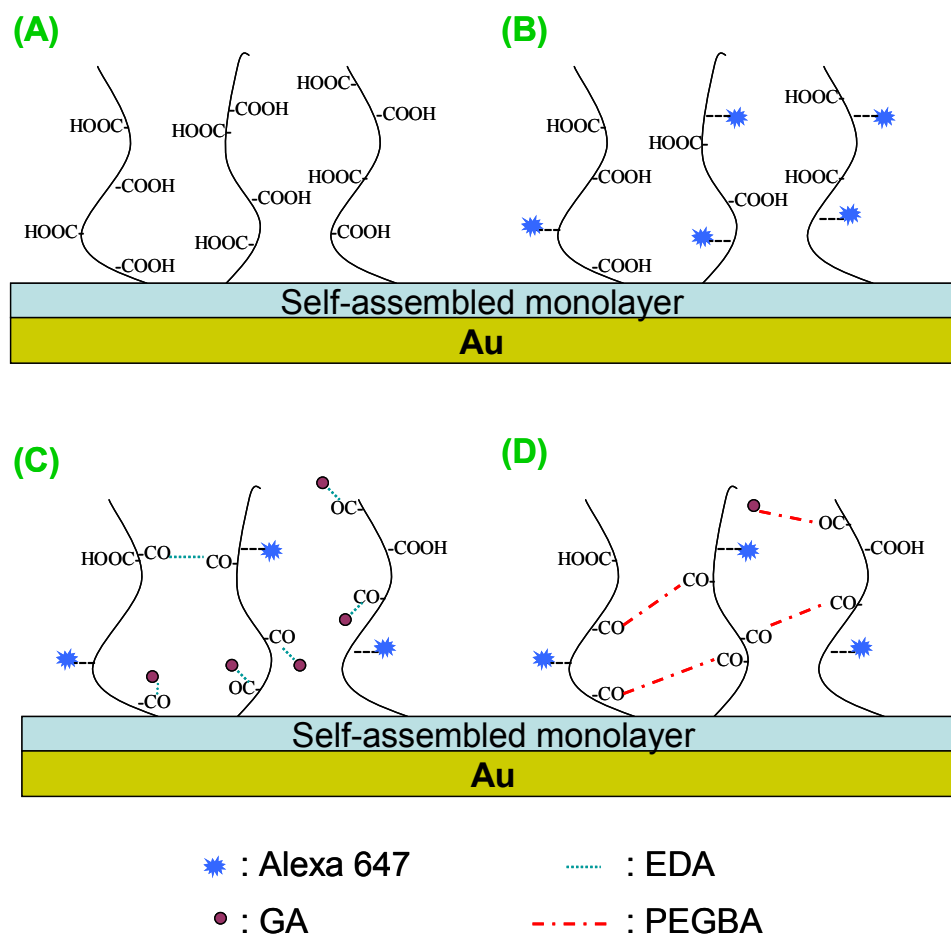


Figure 5.1: Schematics of interfacial architectures of (1) sparsely bound carboxymethyl dextran (CMD), (2) Alexa labeled CMD brush, (3) Alexa labeled CMD/EDA/GA brush, and (4) Alexa 647 labeled CMD/PEGBA/GA network.

For commercial CMD substrates, 1, ω -hydroxyalkanethiols are attached to the gold surface in order to generate a self-assembled monolayer, creating not only a hydrophilic surface but also a barrier to non-specific adsorption of macromolecules to the metal. The hydrophilic

surface serves as a functionalized structure for further modification of the surface. In particular, the surface is modified with a covalently attached dextran, which in turn is carboxymethylated with bromoacetic acid to yield an average of one carboxyl group per glucose residue. The surface coverage of dextran is $200\text{ng}/\text{cm}^2$. The carboxyl groups can be converted to NHS esters, which in turn can be used to immobilize proteins and other molecules. Some limitations and constraints remain, and should be remembered when using CMD. They include the difficulties in coupling molecules with a net negative charge to the negatively charged CMD layer, non-specific electrostatic binding of positively charged molecules to the CMD, and interference with reaction rate measurements by the dextran layer, either by charge effects or steric hindrance. These problems can be minimized by the appropriate choice of the solution pH and ionic strength.¹³⁹ However, the coiled CMD (shown as Figure 5.1A) with its stimuli-responsive carboxymethyl groups and high plasticity acts as a polyelectrolyte layer responding to variable conditions. Therefore, the CMD optical responses corresponding to the stimuli variations as the background signal of the sensor should be investigated and revised without any delay.

It is well known that the swelling equilibrium of a brush is given by the balance of osmotic forces and the elastic force of the stretched subchains. In the charged polyelectrolyte brush, the osmotic force driving solvent into the layer is dominated by the electrostatic repulsion between charges.¹⁴⁰ Specifically, the carboxyl groups on the CMD can be protonated (below the pKa) or deprotonated (above the pKa). Additionally, the electrostatic effects can be controlled by the addition of counter ions that can screen the charges to varying degrees. As a result, the polymer should have a stretched or coiled conformation at the interface depending on the external stimuli, such as pH or ionic strength.

The first set of measurements was performed with the commercial CMD without any further modification (Figure 5.1A). The non-labeled matrix was studied with the conventional reflectivity detection part of the setup. The equilibrium swelling/collapse of CMD was studied as a function of pH or ionic strength. For the pH variation measurements, solutions were gradually changed from acidic (pH=3) to neutral (pH=7) through pH=3, 4, 5, 6, and then directly changed back to acidic conditions (pH=3). The effect of ionic strength was studied by gradually changing solutions from low ionic strength (20mM) to high ionic strength (500mM) through 100mM and 200mM, followed directly again by a measurement at low ionic strength (20mM), while the solution pH was fixed at pH=7.

Surface plasmons are exquisitely sensitive to changes in the properties of the interface. Specifically, changes in the thickness and/or the refractive index of the medium in contact with the metal film result in a change of the dispersion behavior of surface plasmon modes. A quantitative description of all observed phenomena is possible within a theoretical treatment that goes back to Fresnel and models the optical response of a layered architecture by solving Maxwell's equations.¹⁰² The CMD matrix can be described by its dielectric function with a real part and the layer thickness. The SPR resonance angle increases with both increasing thickness and refractive index. Any (partial) collapse-induced decrease of its optical thickness will be accompanied by the increase of its effective refractive index and a swelling induced thickness increase will inversely decrease the effective refractive index. For the surface bound CMD, the gradually increasing solution ionic strength increases the degree of electrostatic screening. The electrostatic repulsion between the polymer charges, which causes swelling/contraction, will be mitigated by the salt. Furthermore, the refractive index of the solvent medium above the film will also contribute to the changes of SPR angular scans (positions of critical angle (cf. Figure 5.3 B) and resonance angle). A monotonic increase of the reflectance of light in the kinetic measurement was observed, resulting both from the increase of CMD refractive index, indicating the increasing degree of collapse at neutral pH, and from the increase of solvent refractive index, as a function of salinity (Figure 5.2A). To exclude the influence of the solution refractive index, octanethiol, as a rigid thiol derivative, was used to self-assemble as an inert, non-responsive layer on the Au surface overnight at room temperature. Subsequently, the substrate was removed, rinsed thoroughly with ethanol, and blown dry by a stream of nitrogen. The substrates thus prepared were used immediately, and the pH and ionic strength dependent measurements were repeated for the octanethiol coated substrate, keeping all other experimental conditions unchanged. The SPR response angles were recorded and used as reference for the measurements with the CMD brush (results not shown).

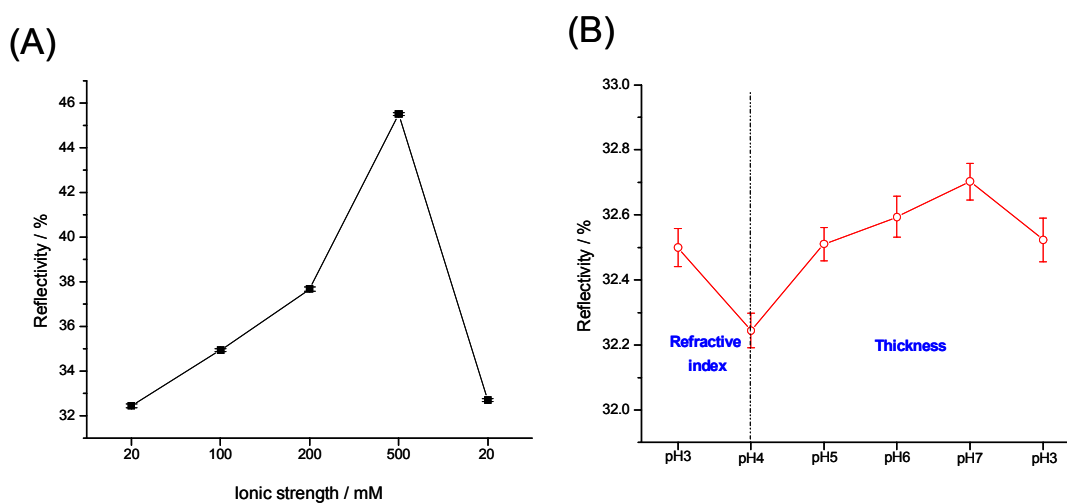


Figure 5.2 Influence of ionic strength (■) and pH (○) variation on the reflected intensity of CMD detected by SPR. Reflected intensities were recorded at a fixed angle of incidence. (A): solution ionic strength was changed from 20 mM to 500 mM, and inversely changed back to 20 mM. (B): solution pH value was changed from acidic (pH=3) to neutral (pH=7) conditions, and inversely changed back to acidic (pH=3) solution.

If we keep the solution ionic strength constant, the influence of solution pH on CMD conformation can be determined (Figure 5.2B) if kinetic measurements were performed by monitoring the reflectance at a fixed laser incidence angle. The solution pH value was changed from 3 to 7, and the reversibility of the reflectivity changes if the pH value was changed back to 3. The protonated dextran chains at lower pH (pH=3) underwent a swelling process while increasing the solution pH value due to the property of CMD ($pK_a \sim 3.5$). Figure 5.2 B shows the appearance of a minimum in the reflectivity at pH 4. The minimum represents the point on either side of which the SPR response is governed predominantly either by thickness variation effects or by changes of the effective refractive index of the layer. Either the increase of thickness or of the refractive index will cause an increase of the observed reflectance. The effect of each of the two factors can vary in magnitude resulting in opposing tendencies. As the pH was increased, the carboxylic acid groups along the CMD were deprotonated. The electrostatic repulsion induced the polymer thickness to increase. As a result, the structure opened up and the solvent molecules start reaching into the inner part of CMD matrix, and the

refractive index decreased. This is represented in the section “Refractive index” of the left part of Figure 5.2 B, where the SPR response is governed predominantly by the effect of a decreasing refractive index. However, it should be noted that the decreasing reflectance before the minimum point is still a result of increasing thickness. If the refractive index decrease is smaller than the sensitivity level of the instrument and the thickness increase effects, gradually a point (minimum point at pH 4) which is represented as the major contributing factor to the SPR response in the section “Thickness” of the right part of Figure 3.2 B, came into play leading to the overall increase in the reflectance. In contrast, the refractive index changes of CMD as a function of different ionic strength is larger and prominent enough to offset the thickness changing effect, and hence shows a persistent tendency. In order to better understand the CMD conformational changes corresponding to stimuli variations, a detection method is preferred, providing more information, rather than balancing several factors like conventional SPR. As a result, SPFS served as a more sensitive detection technique for further investigations.

5.4 Stimuli response of fluorophores labeled CMD detected by SPFS

SPFS is a novel, recently introduced optical detection scheme based on the well-known surface plasmon excitation but involving, in particular, the recording of fluorescence emitted from suitable chromophores excited by the surface plasmon wave. Besides the reflectivity data obtained by conventional SPR studies, parallel fluorescence intensity measurements were taken in order to investigate the conformational changes of CMD (both as a brush and as a crosslinked network) under stimuli variations. To this end, labeling of the CMD with the appropriate fluorophores is required. The surface fluorophore has to be selected so as to allow for an efficient excitation by the laser light source. The maximum absorption peak of Alexa is at $\lambda_{\text{abs}}=649\text{nm}$, which allows for efficient excitation at $\lambda=632.8\text{nm}$ by a red HeNe laser. Furthermore, Alexa offers a significant improvement over many other conventional fluorophores, because it is much brighter and more resistant to photobleaching.¹⁴¹

The kinetic data for the formation of Alexa labeled CMD (Figure 5.1B) is presented in Figure 5.3A. The covalent immobilization process followed a well established amine-coupling protocol.¹⁴² The CMD was activated for 7 min by exposure to a fresh mixture of EDC and NHS,

forming the terminal NHS ester moieties. The Alexa was then injected at a concentration of 2.2 μ M and incubated with the surface overnight. Subsequently, unreacted NHS ester moieties were deactivated by injection of a 1 M ethanolamine hydrochloride solution. Finally, the non-specifically bound Alexa was eliminated from the surface by flushing with 0.1M HCl. All procedures described above were followed by rinsing with water.

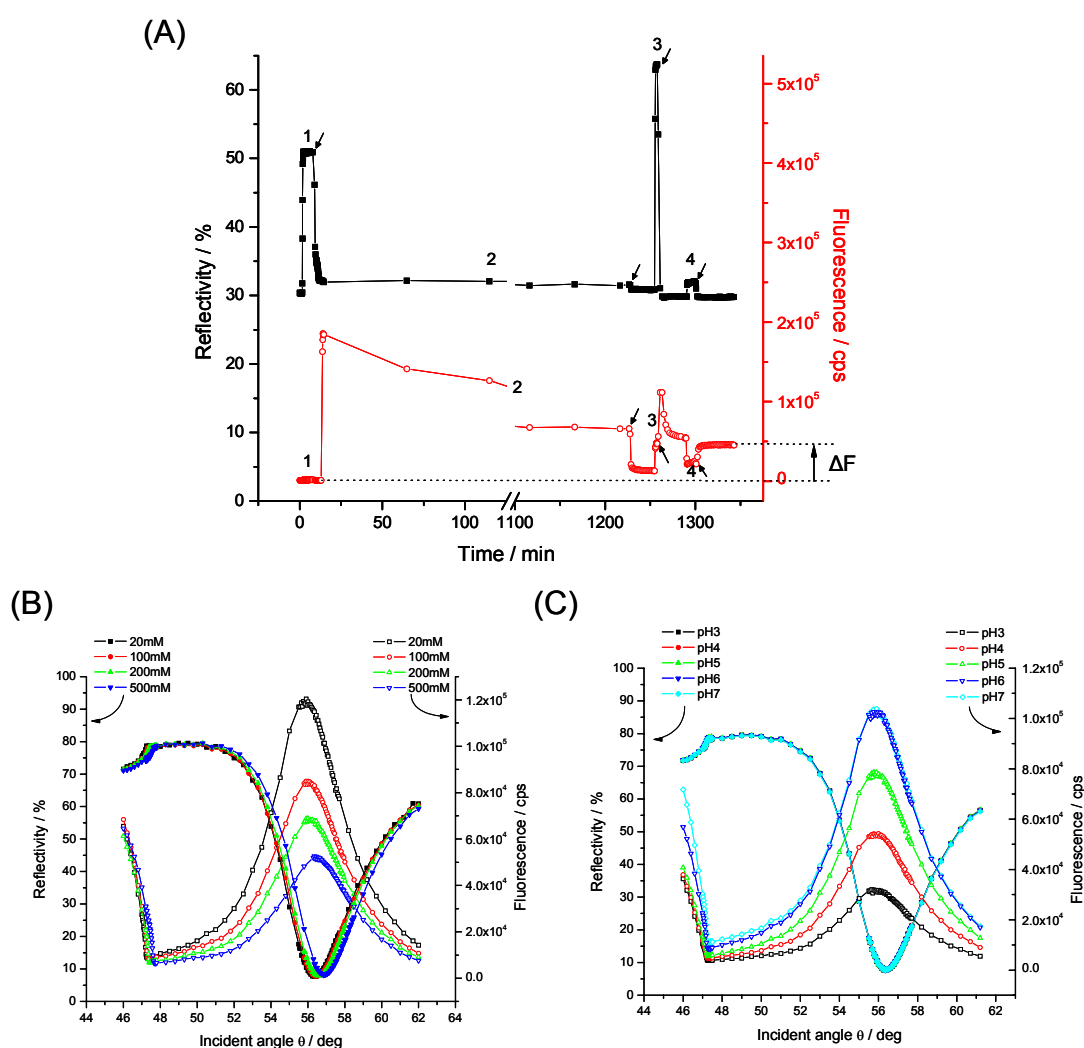


Figure 5.3 (A) Kinetics of reflectivity as well as fluorescence signals for the protocol of covalent immobilization of Alexa to CMD matrix. (1), (2), (3) and (4) represent the EDC/NHS activation, the Alexa immobilization, the deactivation with ethanolamine, and the elimination of non-specific binding of Alexa by HCl, respectively. Arrows indicate the rinse step with water. ΔF shows the final fluorescence intensity after rinsing gained from Alexa immobilization compared to background signal. (B) and (C) show the angular dependences of the reflectivity

(closed symbols) and the simultaneously measured fluorescence intensities (open symbols) for Alexa modified CMD under different pH (B) and ionic strength (C) conditions, respectively.

For SPFS measurements, the variation of the fluorescence intensity following CMD conformational changes can be recorded either by comparing a series of reflectivity scans together with fluorescence intensity angular scans or from the fluorescence kinetic curves measured as a function of time while varying the stimuli conditions. During the kinetic measurements, we monitor signals at a fixed laser incidence angle. Any positive shift of the surface plasmon angular position results in a decrease of the light resonantly coupled, which is used to excite the fluorophores. Due to this fluorescence “detuning” effect the fluorescence intensity at a fixed angle of observation does not scale linearly with the thickness of the adsorbed layer,¹²⁸ and the fluorescence kinetic curves will be distorted if one is dealing with the thickness dependent fluorescence calculations. As a result, the comparison of a series of angular reflectivity and fluorescence intensity scans was preferred for the investigation. For all the matrices investigated in this study, angular scan curves were recorded (Figure 5.3B and C for CMD/Alexa matrix as an example) after the swelling/collapse equilibrium detected from the kinetics study under various stimuli conditions was reached. Subsequently, the peak intensities of the fluorescence curves were taken at different conditions, normalized and plotted as a function of pH or ionic strength for comparisons (as shown, e.g., in Figure 5.4).

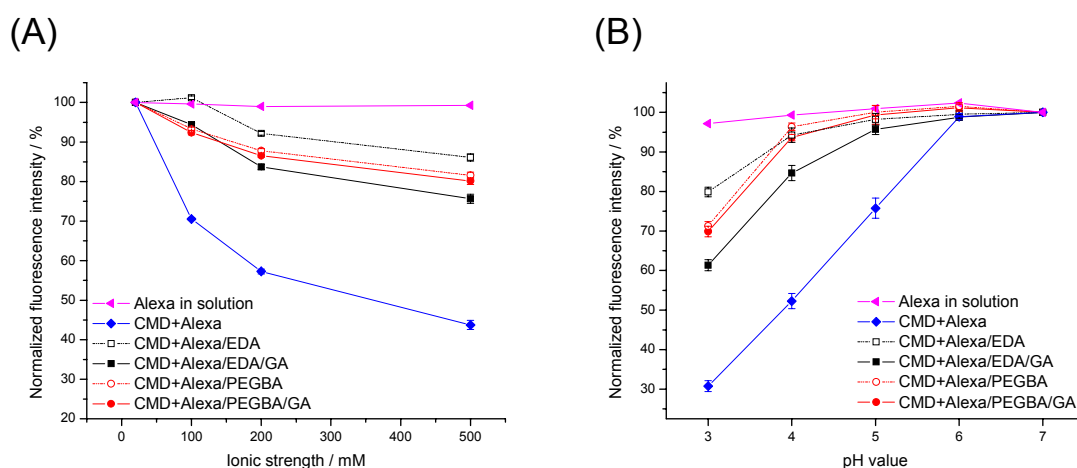


Figure 5.4 Comparisons of ionic strength (A) and pH (B) responses of normalized fluorescence intensity of free Alexa in solution (\blacktriangle), Alexa labeled CMD (\blacklozenge), Alexa labeled CMD/EDA (\square), CMD/EDA/GA (\blacksquare), CMD/PEGBA (\circ), and CMD/PEGBA/GA (\bullet).

The evanescent field of a surface plasmon is enhanced compared to the incident field, and then decays exponentially into the dielectric medium, with the decay length of the surface plasmon being in the range of ca. 200 nm. The evanescent character of the surface plasmon mode leads to an excitation probability that is exponentially decaying away from the interface. The chromophores, hence, should be placed as close to the sensor surface as possible. However, the metallic character of a substrate that is able to carry a surface mode at the same time constitutes a broad band acceptor for energy transfer (Förster) processes between an excited chromophore and the noble metal substrate. The fluorescence is consequently ‘quenched’, dissipating the excitation energy in the metal as heat. The relevant distance dependence, however, for this coupling scheme is governed by the Förster radius for energy transfer and leads to a significant loss of fluorescence intensity by quenching.⁹ Inspired by the fact that the behavior of a chromophore (dipole) in front of a metal surface is largely dependent on the separation distance, the fluorescence intensity observed for chromophores that are placed within a matrix layer assembled on the (Au) sensor surface can be used to imply the conformation of the studied matrices. According to the relationship between fluorescence intensity and its separation distance to the sensor surface, the fluorescence intensity of surface immobilized Alexa molecules under different conditions can be interpreted to the conformational changes of CMD matrices.

The profile of pH and ionic strength influences on the conformation of surface bound CMD matrices is shown in Figure 5.4. The peak intensities of fluorescence angular scans (shown in Figure 5.3B and C as an example) were taken at different pH, normalized to the intensities obtained at pH=3 (cf. Figure 5.4 A), or at 20mM buffer for the ionic strength dependence (cf. Figure 5.4 B), and plotted as a function of pH or ionic strength for comparisons. Furthermore, the stimuli responses of Alexa were also tested in solution using regular fluorescence spectroscopy (TIDAS Fluorescence-Diode-Spectrometer, J&M Analytische Mess- und Regeltechnik GmbH), with the results serving as a control. Alexa, dissolved at a concentration of 1 μ M, was excited at $\lambda = 645\text{nm}$, and the fluorescence emission was collected at $\lambda = 670\text{nm}$. We found that no variation of the fluorescence intensity in Figure 5.4A and B was observed for free Alexa in solution under different conditions. By virtue of this fact, we attribute changes of fluorescence intensities observed to the distance-dependent behavior of the surface

immobilized chromophores, which further indicates the conformational changes of the CMD caused by stimuli variations.

For the ionic strength-responsive characteristics (Figure 5.4 A), the solution pH was fixed at pH = 7.0 to provide deprotonated carboxyl groups for the maximum performing of charge screening. An increase in ionic strength generally decreases the fluorescence intensity for all the matrices investigated, because the salt induced CMD contraction (mechanism described above) shortens the separation distance between the fluorophores and the sensor surface, which in turn reduces the fluorescence intensity due to the quenching effect. Additionally, the pH-induced swelling behavior of the CMD matrices is shown in Figure 5.4 B. An increase in pH from 3 to 7 generally caused an increase in the fluorescence intensity for different matrices, as a result of the CMD swelling induced by the pH increase. The same was observed in the SPR measurements, extend the separation distance of Alexa to the sensor surface. Longer distance consequently reduced the quenching effect of the fluorophore and increased the fluorescence intensity. The maximum extents of swelling were reached at pH 6 in all investigated matrices, due to complete deprotonation of carboxyl groups of CMD at this pH value.

5.5 Influence of surface charge and crosslink densities on the stimuli responses of CMD

Figure 5.4 shows the effect of crosslinks on the conformational changes of CMD. It is well known that polysaccharides, including dextran, is easily crosslinked with various functional organic and inorganic compounds thus forming a swollen aqueous gel.¹⁴³⁻¹⁴⁵ Two kinds of CMD matrices, CMD/EDA/GA (Figure 5.1C) and CMD/PEGBA/GA (Figure 5.1D), were obtained by crosslinking CMD with a shorter crosslinker, EDA, or an extended crosslinker, PEGBA, respectively. The EDC/NHS activated CMD brush was first incubated with 2.2 μ M Alexa for 2hr. After rinsing with water, 1M EDA or 85 μ M PEGBA was injected and allowed to react with the remaining carboxyl groups on the CMD substrates overnight. Next, the unreacted NHS ester moieties were capped with ethanolamine. Free Alexa, EDA, and PEGBA molecules were removed from the surface by rinsing with HCl. Alternatively, 5% glutaraldehyde (GA) was used as blocking reagent for unreacted end-amino groups decorated

by EDA or PEGBA on the surface, forming the matrices of CMD/EDA/GA and CMD/PEGBA/GA.

Different situations were generated when EDA and PEGBA were used as shorter and extended crosslinkers, respectively. In particular, EDA (diamine with a short intermediate linker) due to its short chain length will probably expose one amino end-group to free space while the other amino group is covalently bound to a carboxyl group on the CMD. A buffering system was generated with unreacted carboxyl groups on the CMD and newly attached amino groups. As a result, a low degree of contraction/swelling extent was obtained for the CMD/EDA matrix as a function of both the ionic strength (Figure 5.4 A) and the pH (Figure 5.4 B). For comparison, the newly generated amino groups normally used as crosslink reagent between amino groups were blocked by GA. The CMD/EDA/GA system shows a higher extent of conformational changes compared to the CMD/EDA system according to the stimuli variation experiments (Figure 5.4). The effective function of GA indicates the large amount of end-exposed amino groups of the surface attached EDA, resulting in the low level of crosslink density of CMD matrix. As a result, we still regard CMD/EDA/GA as a brush matrix in view of the small amount of EDA-induced CMD crosslink. Correspondingly, PEGBA, a diamine with a long (M_w : 2100) PEG chain as intermediate linker, was used to obtain a CMD network with a high crosslink density. The high level of crosslink was proved by the comparison of the stimuli responses of CMD/PEGBA with CMD/PEGBA/GA (cf. Figure 5.4). The similar collapse/swelling ratios obtained for both matrices indicates the weak effect of GA, which further demonstrates the small amount of exposed one amine-end groups of the surface attached PEGBA. As a result, a higher crosslink density was obtained for the CMD/PEGBA/GA matrix compared to CMD/EDA/GA system.

The effect of crosslinks on the extent of CMD stimuli response can be explained by taking into consideration the carboxyl group concentration present on the CMD chains. The surface concentrations of carboxyl groups on four different kinds of matrices (schematics shown in Figure 5.1A, B, C, and D) were determined by reactions with TBO as described elsewhere.¹⁴⁶ A calibration curve was first generated for the absorbance of a series of TBO solutions of known concentrations, taken at $\lambda=633$ nm by an UV/VIS/NIR spectrometer (Perkin Elmer, Lambda 900). One milliliter of the aqueous solution containing 0.5mM TBO was injected to circulate through the sensor chip with an area of 0.28 cm². The formation of ionic complexes between

the COOH groups of the CMD and the cationic dyes was allowed to proceed for 5 hr at room temperature at constant circulation with a flow rate of 1 ml/min. Subsequently, the sensor surface was rinsed thoroughly with 0.1mM NaOH solution in order to remove any non-complexed TBO molecules. Then the TBO molecules complexed to the CMD were desorbed from the surface by incubating the chip in 1mL of 50% acetic acid solution for 10 min under circulation. The concentration of the COOH groups on the CMD surface was calculated from the absorbance of the desorbed dye at $\lambda = 633$ nm. The calculation was based on the assumption that 1 mol of TBO combines with 1 mol of the carboxyl group on the CMD matrix.^{147,148}

A maximum concentration of carboxyl groups of $1.17\text{nM}/\text{cm}^2$ was achieved for the original CMD surface without any modification (Figure 5.1A), which is quite consistent with the theoretical COOH concentration of CMD with $1\text{nM}/\text{cm}^2$. For the Alexa labeled CMD brushes (Figure 5.1B), a carboxyl concentration of $0.74\text{nM}/\text{cm}^2$ was obtained, while for the Alexa labeled CMD/EDA/GA (Figure 5.1C) and CMD/PEGBA/GA (Figure 5.1D) systems, similar surface carboxyl group concentrations were found, with $0.53\text{nM}/\text{cm}^2$ and $0.56\text{nM}/\text{cm}^2$, respectively. The trend of an increasing swelling/contraction ratio with increasing carboxyl groups was apparent in the comparison of the matrices CMD/Alexa and CMD/EDA/GA, both of which are matrices with brush conformation. Since the swelling of a hydrogel is induced by the electrostatic repulsion of the ionic charges, the carboxyl groups provide the only charges in CMD causing the hydrogel to swell or to contract. The number of carboxyl groups of the matrix CMD/Alexa is larger than that of the matrix CMD/EDA/GA which, in turn, results in a higher degree of swelling/contraction. This is an expected result, because EDA is chemically bound to the carboxymethyl groups and thus reduce the amount of charged groups participating in the swelling/collapse behavior.

According to the fact that the charge density of the polymer chain will largely influence the degree of swelling/collapse, the two matrices CMD/EDA/GA and CMD/PEGBA/GA with similar surface carboxyl group concentrations were used in order to investigate the effect of crosslinks on the extent of the CMD stimuli response. Figure 5.4 show that the extent of swelling of the CMD/EDA/GA matrix is higher than that of CMD/PEGBA/GA. This is in spite of two contributions for the latter matrix (CMD/PEGBA/GA), i.e., the slightly higher amount of free carboxyl groups available and the increase of driving force for swelling due to the highly soluble intermediate PEG chains of PEGBA,¹⁴⁰ which then lead the crosslinked matrix

to higher swelling ratio. The low swelling/collapse ratio for CMD/PEGBA/GA can be explained by increased retractive forces for increased crosslink densities, which prevent the hydrogel from expanding. Higher crosslink density intensifies a resistance to chain extension, thereby reducing the equilibrium swelling, and reduces the availability of the free carboxyl groups and hence alters the hydrophilic content in CMD. Both these factors contribute towards lowering of equilibrium swelling in the CMD matrix with higher crosslink density.

5.6 Conclusion

We reported here the influences of external stimuli (pH, and ionic strength) and internal properties (surface charge and crosslink density) on the conformational changes of CMD, a commercially available sensor matrix from Biacore. SPFS, which provides information complementary to conventional SPR, is an appropriate method for the investigation of conformational changes of interfacial architectures. The pH response of CMD is due to the changes in the electrostatics of the system between its protonated and deprotonated forms, while the ionic strength response is attributed to the charge screening effect of the cations that shield the charge of the carboxyl groups and prevent an efficient electrostatic repulsion. Meanwhile, results revealed that the levels of surface carboxyl groups and crosslink density can be used to fine-tune the degree of CMD swelling within a modest range. The range of swelling/collapse increases with the CMD charge density (i.e., the amount of free carboxyl groups on the surface). Furthermore, CMD showed decreasing swelling ratios, upon an increased level of crosslinks. The study of CMD responses to external and internal variables will provide valuable background information for practical applications.

6 SUMMARY

The research has included the efforts in designing, assembling and structurally and functionally characterizing supramolecular biofunctional architectures for optical biosensing applications.

In the first part of the study, a class of interfaces based on the biotin-NeutrAvidin binding matrix for the quantitative control of enzyme surface coverage and activity was developed. Genetically modified β -lactamase was chosen as a model enzyme and attached to five different types of NeutrAvidin-functionalized chip surfaces through a biotinylated spacer. All matrices are suitable for achieving a controlled enzyme surface density. Data obtained by SPR are in excellent agreement with those derived from optical waveguide measurements. Among the various protein-binding strategies investigated in this study, it was found that stiffness and order between alkanethiol-based SAMs and PEGylated surfaces are very important. Matrix D based on a Nb₂O₅ coating showed a satisfactory regeneration possibility. The surface-immobilized enzymes were found to be stable and sufficiently active enough for a catalytic activity assay. Many factors, such as the steric crowding effect of surface-attached enzymes, the electrostatic interaction between the negatively charged substrate (Nitrocefin) and the polycationic PLL-g-PEG/PEG-Biotin polymer, mass transport effect, and enzyme orientation, are shown to influence the kinetic parameters of catalytic analysis.

Furthermore, a home-built Surface Plasmon Resonance Spectrometer of SPR and a commercial miniature Fiber Optic Absorbance Spectrometer (FOAS), served as a combination set-up for affinity and catalytic biosensor, respectively. The parallel measurements offer the opportunity of on-line activity detection of surface attached enzymes. The immobilized enzyme does not have to be in contact with the catalytic biosensor. The SPR chip can easily be cleaned and used for recycling. Additionally, with regard to the application of FOAS, the integrated SPR technique allows for the quantitative control of the surface density of the enzyme, which is highly relevant for the enzymatic activity. Finally, the miniaturized portable FOAS devices can easily be combined as an add-on device with many other in situ interfacial detection techniques,

such as optical waveguide lightmode spectroscopy (OWLS), the quartz crystal microbalance (QCM) measurements, or impedance spectroscopy (IS).

Surface plasmon field-enhanced fluorescence spectroscopy (SPFS) allows for an absolute determination of intrinsic rate constants describing the true parameters that control interfacial hybridization. Thus it also allows for a study of the difference of the surface coupling influences between OMCVD gold particles and planar metal films presented in the second part. The multilayer growth process was found to proceed similarly to the way it occurs on planar metal substrates. In contrast to planar bulk metal surfaces, metal colloids exhibit a narrow UV-vis absorption band. This absorption band is observed if the incident photon frequency is resonant with the collective oscillation of the conduction electrons and is known as the localized surface plasmon resonance (LSPR). LSPR excitation results in extremely large molar extinction coefficients, which are due to a combination of both absorption and scattering. When considering metal-enhanced fluorescence we expect the absorption to cause quenching and the scattering to cause enhancement. Our further study will focus on the developing of a detection platform with larger gold particles, which will display a dominant scattering component and enhance the fluorescence signal. Furthermore, the results of sequence-specific detection of DNA hybridization based on OMCVD gold particles provide an excellent application potential for this kind of cheap, simple, and mild preparation protocol applied in this gold fabrication method.

In the final chapter, SPFS was used for the in-depth characterizations of the conformational changes of commercial carboxymethyl dextran (CMD) substrate induced by pH and ionic strength variations were studied using surface plasmon resonance spectroscopy. The pH response of CMD is due to the changes in the electrostatics of the system between its protonated and deprotonated forms, while the ionic strength response is attributed from the charge screening effect of the cations that shield the charge of the carboxyl groups and prevent an efficient electrostatic repulsion. Additional studies were performed using SPFS with the aim of fluorophore labeling the carboxymethyl groups. CMD matrices showed typical pH and ionic strength responses, such as high pH and low ionic strength swelling. Furthermore, the effects of the surface charge and the crosslink density of the CMD matrix on the extent of stimuli responses were investigated. The

swelling/collapse ratio decreased with decreasing surface concentration of the carboxyl groups and increasing crosslink density. The study of the CMD responses to external and internal variables will provide valuable background information for practical applications.

7 SUPPLEMENT

7.1 Abbreviations

Alexa	Alexa Fluor 647 hydrazide
ATR	attenuated total reflection
BSA	bovine serum albumin
CMCs	ceramic matrix composite
CMD	carboxymethyl dextran
cps	counts per second
CVD	Chemical Vapour Deposition
Cy5/Cy3	cyanine dye
DNA	deoxyribonucleic acid
DMSO	dimethyl sulfoxide
DTT	dithiothreitol
EDA	ethylenediamine
EDC	carbodiimide hydrochloride
FOAS	miniature Fiber Optic Absorbance Spectroscopy
GA	Glutaraldehyde
HEPES	4-(2-Hydroxyethyl) piperazine-1-ethane-sulfonic acid
HeNe	Helium-Heon
IS	impedance spectroscopy
I.U.	international units
LASFN9	high refractive index glass from Schott
LEDs	light-emitting diodes
LSPR	localized surface plasmon resonance
LSPs	localized surface plasmons
MM	(base pair) Mismatch
Mw	molecular weight
n	refractive index
Nb ₂ O ₅	niobium oxide
NHS	N-hydroxy succinimide
NSB	non-specific binding
OMCVD	organometallic chemical vapor deposition
OWLS	optical waveguide lightmode spectroscopy
PBST	10 mM phosphate buffer, 2.7 mM KCl, 150 mM NaCl,
0.005% Tween 20, pH 7.4	
PEGBA	Poly (ethylene glycol) bis (3-aminopropyl) terminated
PLL-g-PEG	Poly (L-lysine)-g-poly (ethylene glycol)
PLL-g-PEG/PEG-biotin groups	PLL-g-PEG graft copolymers carrying terminal biotin groups
PMT	photomultiplier
PS	polystyrene
PSP	plasmon surface polariton
PSPs	propagating surface plasmons

PWR	plasmon-waveguide resonance
QCM	quartz crystal microbalance
RP _s	radiating plasmons
SAM	self-assembled monolayer
SAR	scanning angle reflectometry
SERS	surface enhanced Raman spectroscopy
SiO ₂	silicon oxide
SMS	single molecule spectroscopy
SP	surface plasmons
SPFS	surface plasmon fluorescence spectroscopy
SPR	surface plasmon resonance
TBO	Toluidine blue O
TBP	Tri-n-butylphosphine
TE	transversal electric (s-) polarization
TIR	total internal reflection
TIRF	total internal reflection fluorescence
TIRS	total internal reflection spectroscopy
TM	transversal magnetic (p-) polarization
UV	ultraviolet

7.2 List of Figures

Figure 1.1: a schematic of a charged hydrogel film. The gel is composed of subchains (dark grey) linked through crosslinks (black). Each subchain carries fixed charges (white). However, the charges may be dissociated (active) or undissociated (inactive), depending on the location of their counterions (light grey). The electrostatic repulsion between neighboring fixed charges drives for swelling, while the stretching energy of the subchains between crosslinks favors collapse. The gel may also carry uncharged pendant chains (striped) such as PEG, which do not participate in the electrostatic interactions or in the hydrogel chain elasticity, but do contribute to the overall osmotic force in the system..... 6

Figure 2.1: Evanescent field excitation using TIR (a) and SPR (b) mode..... 20

Figure 2.2: Schematic presentation of a surface plasmon at the interface between a metal and a dielectric. Note the sign of the two media need to be opposite to allow for plasmon excitation... 22

Figure 2.3: The dispersion relation of free photons in a dielectric (A), and in a coupling prism (B), compared to the dispersion relation for non-radiative surface plasmons at the metal/dielectric interface before (SP1) and after (SP2) the adsorption of an additional dielectric layer..... 25

Figure 2.4: Prism coupling geometries for Otto configuration (A) and Kretschmann-Raether configuration (B). Coupling is only possible when the refractive index of the prism is higher than that of the dielectric..... 26

Figure 2.5: Typical surface plasmon resonance curves of the prism/gold/water system before (solid line) and after (dot line) the deposition of an ultrathin layer onto the gold..... 28

Figure 2.6: Reflectivity R and the relative intensity $I_S:I_0$, i.e. the optical intensity at the surface, I_S , scaled to the incoming intensity, I_0 , as a function of the angle of incidence, u , for a mere total internal reflection (TIR) geometry, i.e. for a glass:water-interface (a), or for plasmon surface polariton excitation at a silver:water-interface (b), or a Au:water-interface (c). Note the different intensity enhancements for the three situations..... 33

Figure 2.7: Schematic of the different electronic coupling regimes for a fluorophore in water at different distances to a metal film surface..... 36

Figure 2.8: Comparative presentation of the distance dependence of the optical field enhancement of a surface plasmon evanescent wave mode excited at a prism/Au/water interface (solid curve), and the Förster energy transfer mechanism, expressed as the relative fluorescence intensity (dashed curve) placed at a certain distance above the metal/water interface..... 37

Figure 2.9: (a) Surface intensity (dotted curves) and resulting fluorescence intensity (full curve) for a bare Au:water interface, and with a thin dielectric coating of 2.5 or 5 nm, respectively, doped with a fictive fluorescent dye system. The corresponding shift of the PSP resonance angle results, at a fixed angle of observation, e.g. at u_k , in a less than linear increase of the fluorescence intensity (cf. the different shaded arrows). (b) Simulation of the deviation of a linear fluorescence intensity increase from an increase in layer thickness, equivalent to a shift of the resonance angle for PSP excitation. Note that only for very thin layers, i.e. for $d \ll \lambda$, a linear approximation holds..... 38

Figure 2.10: Schematic of a surface plasmon field-enhanced fluorescence spectroscopy setup with two separate excitation laser sources..... 40

Figure 2.11: Lineweaver-Burk Plots..... 47

Figure 2.12: Schematic of the FOAS setup for the enzymatic activity assay..... 48

Figure 2.13: Schematic showing basic interactions on the biosensor surface. The ligand (B) is attached to the surface via a flexible linker. During the association phase, analyte (A) is flowed past the surface. k_m is the mass transport coefficient used to describe the diffusion of analyte through the diffusion layer. k_{on} and k_{off} are the association and dissociation rate constants, which describe the formation of the complex (AB)..... 52

Figure 3.1 Structure formula of (1) hydroxyl-terminated thiol (11-Mercapto-1-undecanol), (2) biotin-terminated thiol (HS-c12-dadoo-Biotin), and (3) carboxyl-terminated thiol (11-

Mercaptoundecanoic acid) employed for the preparation of self-assembled monolayers (SAMs). 59

Figure 3.2: Schematic of the five matrices used for protein binding. 60

Figure 3.3: Comparison of the optical thickness of surface bound β -lactamase between stepwise binding and pre-incubation strategies based on five different kinds of matrices detected by SPR. Inset numbers indicate the values of $T_{\text{stepwise}} / T_{\text{pre-incubation}}$ (ratio of optical thickness of surface attached biotin- β -lactamase based on stepwise binding strategy to the obtained thickness based on pre-incubation strategy. A, B, C, D, and E: symbols of matrices used in the study. 63

Figure 3.4: Comparisons of the surface coverage amounts of PLL-g-PEG/PEG-Biotin, NeutrAvidin, and β -lactamase based on matrix C with pre-incubation strategy obtained from SPR and OWLS measurements, respectively. 64

Figure 3.5: Enzymatic activity and Stability of surface immobilized β -lactamase based on matrix A. 67

Figure 3.6: Kinetics of the turnover of nitrocefin detected with FOAS for the investigation of surface-bound β -lactamase monitored at $\lambda = 500\text{nm}$ 69

Figure 3.7: Comparison of (1) surface coverage; (2) K_M ; (3) k_{cat} ; (4) k_{cat}/K_M values between matrices based on PLL-g-PEG/PEG-Biotin (matrices C and D) and biotinylated SAMs with medium surface coverage of β -lactamase. 73

Figure 4.1 Structure formulas of (A) hydroxyl-terminated thiol and (B) biotin-terminated thiol, employed for the preparation of Self-assembled Monolayers (SAMs). (C): The base sequence of the employed probe oligonucleotides (P2) with 15 thymine spacer units and the biotin-coupling group at the 5' end. (D): The corresponding 15-mer fully complementary DNA target (T2) carries the fluorophore Cy3 at their 5' end. (E): The corresponding 15-mer mismatch 1 DNA target (T1) carries the fluorophore Cy3 at their 5' end. 77

Figure 4.2: UV-Vis spectra of (a) MPTS SAMs and of the (b) OMCVD gold nanoparticles on MPTS SAMs. 78

Figure 4.3: (a) SEM images of OMCVD gold on MPTS. (b) Zoom-in of (a). (c) Size distribution of OMCVD gold (using a sample of 150 particles). 79

Figure 4.4: UV-Vis spectra of OMCVD gold at different reaction times. The first straight line refers to MPS SAMs without the OMCVD gold. 80

Figure 4.5: (C1) and (C2): Cartoon of planar propagating surface plasmons (PSPs) and particle localized surface plasmons (LSPs) interfacial multilayer matrices, respectively. (S1) and (S2): Angular reflected intensity scans (closed symbols) before (!) and after (,) the hybridization of DNA target (T2) from solution to the surface attached DNA probe (P2), as well as the simultaneously measured fluorescence intensities (open symbols) as a comparison between the background signal (∇) and the signals of taken after the specifically binding of DNA probe and fully complementary target (-) (MM0) for different interfacial architectures (cf. (S1): PSPs matrix; (S2): LSPs matrix) detected by SPFS with the incident wavelength of 543nm. Arrows show the fixed incident angle position, 60° and 49° for kinetic measurements for PSPs and LSPs matrices, respectively. (K1) and (K2): kinetic fluorescence scans (black dotted line) taken for hybridization (non-specific binding, association, and dissociation) processes between the surface oligonucleotide (P2) and T2 (mismatch0) target complements from solution. Arrows show the rinsing steps with pure buffer. The red full curves are theoretical calculations based on langmuir association / dissociation model, with rate constants, adsorption (hybridization) rate constant, K_{on} ; dissociation rate constant, K_{off} ; affinity constant, $K_A=K_{\text{on}}/K_{\text{off}}$, given beside the curves. 1, 2, 3, 4, and 5 represent the binding protocols of streptavidin modified surface, Non-specific binding of T2, P2 attachment, T2 association, and T2 dissociation processes, respectively. 82

Figure 4.6: (A): Schematic representation and fluorescence kinetic measurement of the binding process of DNA target (T2) on the mercaptosilane SAMs system (without the OMCVD of gold particles). (B): kinetic fluorescence scans (black curve) taken for mismatch0 (MM0) hybridization (non-specific-binding, association, and dissociation) processes between the probe (P2) oligonucleotide surface and fully complementary DNA target complements (T2) from the solution. (C): kinetic fluorescence measurement (black curve) for mismatch1 (MM1) hybridization between P2 and T1. Arrows show the rinsing steps with pure buffer. The red full

curves in (B) and (C) are theoretical calculations based on Langmuir association / dissociation model, with rate constants, adsorption (hybridization) rate constant, K_{on} ; dissociation rate constant, K_{off} ; affinity constant, $K_A=K_{on}/K_{off}$, given beside the curves. 1, 2, 3, 4, and 5 represent the binding protocol of streptavidin modified surface, Non-specific binding of DNA target (T2 for (B) and T1 for (C)), P2 attachment, association, and dissociation processes of DNA target (T2 for (A) and (B); T1 for (C)), respectively. 87

Figure 5.1: Schematics of interfacial architectures of (1) sparsely bound carboxymethyl dextran (CMD), (2) Alexa labeled CMD brush, (3) Alexa labeled CMD/EDA/GA brush, and (4) Alexa 647 labeled CMD/PEGBA/GA network. 93

Figure 5.2 Influence of ionic strength (■) and pH (○) variation on the reflected intensity of CMD detected by SPR. Reflected intensities were recorded at a fixed angle of incidence. (A): solution ionic strength was changed from 20 mM to 500 mM, and inversely changed back to 20 mM. (B): solution pH value was changed from acidic (pH=3) to neutral (pH=7) conditions, and inversely changed back to acidic (pH=3) solution. 96

Figure 5.3 (A) Kinetics of reflectivity as well as fluorescence signals for the protocol of covalent immobilization of Alexa to CMD matrix. (1), (2), (3) and (4) represent the EDC/NHS activation, the Alexa immobilization, the deactivation with ethanolamine, and the elimination of non-specific binding of Alexa by HCl, respectively. Arrows indicate the rinse step with water. ΔF shows the final fluorescence intensity after rinsing gained from Alexa immobilization compared to background signal. (B) and (C) show the angular dependences of the reflectivity (closed symbols) and the simultaneously measured fluorescence intensities (open symbols) for Alexa modified CMD under different pH (B) and ionic strength (C) conditions, respectively. 98

Figure 5.4 Comparisons of ionic strength (A) and pH (B) responses of normalized fluorescence intensity of free Alexa in solution (◀), Alexa labeled CMD (◆), Alexa labeled CMD/EDA (□), CMD/EDA/GA (■), CMD/PEGBA (○), and CMD/PEGBA/GA (●). 99

7.3 List of Tables

Table 3.1: Evaluation of regeneration possibilities for five matrices based on stepwise binding strategy..... 65

Table 3.2: SPR results and kinetic parameters obtained from miniature Fiber Optic Absorbance spectroscopy (FOAS) for free and surface immobilized β -lactamase based on matrix A with different enzyme surface coverages 69

Table 3.3: Surface coverage determined by SPR of biotin- β -lactamase immobilized on gold-coated chips with the four different interfacial matrices (B-E, see Fig. 3.2), and kinetic parameters of the enzymatic turnover of Nitrocefin by surface-immobilized β -lactamase and by the “free” enzyme in solution, obtained from miniature Fiber Optic Absorbance spectroscopy (FOAS) 72

7.4 Bibliography

1. Eggins, B. R. *Biosensors: an Introduction*, John Wiley and Sons Inc: New York, 1996.
2. Rogers, K. R. *Handbook of biosensors and electronic noses: Medicine, Food, and the Environment*, CRC Press Inc.: Boca Raton, 1997.
3. Jonsson, U.; Fagerstam, L.; Ivarsson, B.; Johnsson, B.; Karlsson, R.; Lundh, K.; Lofas, S.; Persson, B.; Roos, H.; Ronnberg, I.; Sjolander, S.; Stenberg, E.; Stahlberg, R.; Urbaniczky, C.; Ostlin, H.; Malmqvist, M. *Biotechniques* **1991**, *11*, 620-&.
4. Day, Y. S. N.; Baird, C. L.; Rich, R. L.; Myszka, D. G. *Protein Science* **2002**, *11*, 1017-25.
5. Liebermann, T.; Knoll, W. *Colloids and Surfaces A-Physicochemical and Engineering Aspects* **2000**, *171*, 115-30.
6. Neumann, T.; Johansson, M. L.; Kambhampati, D.; Knoll, W. *Advanced Functional Materials* **2002**, *12*, 575-86.
7. Kuswandi, B.; Andres, R.; Narayanaswamy, R. *Analyst* **2001**, *126*, 1469-91.
8. Wise, D. L.; Wingard, L. B. *Biosensors with Fiberoptics*, Humana Press: New Jersey, 1991.
9. Knoll, W.; Park, H.; Sinner, E.; Yao, D.; Yu, F. *Surface Science* **2004**, *570*, 30-42.
10. Lowman, A. M.; Peppas, N. A. *Hydrogels*, Mathiowitz, E., Ed.; Wiley: New York, 1999.
11. Qiu, Y.; Park, K. *Adv Drug Delivery Rev* **2001**, *53*, 321-39.
12. Hoffman, A. S. *Adv Drug Delivery Rev* **2002**, *54*, 3-12.
13. Silberberg-Bouhnik, M.; Ramon, N.; Ladyzhinski, I.; Mizrahi, S. *J Polym Sci: Part B: Polym Phys* **1995**, *33*, 2269-79.
14. Khare, A. R.; Peppas, N. A.; Massimo, G.; Colombo, P. *J Controlled Rel* **1992**, *22*, 239-44.
15. Hariharan, D.; Peppas, N. A. *Polymer* **1996**, *37*, 149-61.
16. Peppas, N. A. *Compatible Polym* **1991**, *6*, 241-46.
17. Chiu, H. C.; Lin, Y. F.; Hsu, Y. H. *Biomaterials* **2002**, *23*, 1103-12.
18. Eichenbaum, G. M.; Kiser, P. F.; Simon, S. A.; Needham, D. *Macromolecules* **1998**, *31*, 5084-93.
19. Matsuda, A.; Katayama, Y.; Kaneko, T.; Gong, J. P.; Osada, Y. *J Mol Struct* **2000**, *554*, 91-97.
20. Nisato, G.; Schosseler, F.; Candau, S. J. *Polym Gels Networks* **1996**, *4*, 481-98.
21. De, S. K.; Aluru, N. R.; Johnson, B.; Crone, W. C.; Beebe, D. J.; Moore, J. J. *Microelectromechanical Systems* **2002**, *11*, 544-55.
22. Podual III, K. F. J. D.; Peppas, N. A. *Polymer* **2000**, *41*, 3975-83.

23. Horkay, F.; Basser, P. J. 33 ed.; 8333, 2000.
24. Peppas, N. A.; Barr-Howell Characterization of the cross-linked structure of hydrogels., Peppas, N. A., Ed.; CRC Press: West Lafayette, 1986.
25. Mark, J. E. *J Phys Chem B* **2003**, *107*, 903-13.
26. Bromberg, L.; Grosberg, A. Y.; Matsuo, E. S.; Suzuki, Y.; Tanaka, T. *JCP* **1997**, *106*, 2906-10.
27. Alvarez-Lorenzo, C.; Concheiro, A. *J Control Rel* **2002**, *80*, 247-57.
28. English, A. E.; Tanaka, T. *J Chem Phys* **1996**, *105*, 10606-13.
29. Khare, A. R.; Peppas, N. A. *Biomaterials* **1995**, *16*, 559-67.
30. Kikuchi, A.; Okano, T. *Adv Drug Delivery Rev* **2002**, *54*, 53-77.
31. Murray, R. J. Peroral Insulin Delivery Using pH-Responsive P(MAA-g-EG) Gels [MS]., Drexel University: Philadelphia, 2001.
32. Torres-Lugo, M.; Peppas, N. A. *Macromolecules* **1999**, *32*, 6646-51.
33. Dan, N. *Langmuir* **2002**, *18*, 3524-27.
34. Dan, N. *Colloids Surf B: Biointerfaces* **2003**, *27*, 41-47.
35. Nelson, P. Biological physics, Freeman: New York, 2002.
36. Israelachvili, J. N. Intermolecular and surface forces., Academic Press: London, 1992.
37. Kumar, A.; Gupta, R. K. Fundamentals of polymers., McGraw-Hill: New York, 1998.
38. Schwarte, L. M.; Peppas, N. A. *Polymer* **1998**, *39*, 6057-66.
39. Lowman, A. M.; Peppas, N. A. *J Biomater Sci-Polym Ed* **1999**, *10*, 999-1009.
40. Jensen, T. R.; Malinsky, M. D.; Haynes, C. L.; Van Duyne, R. P. *J.Phys.Chem.B* **2000**, *104*, 10549-56.
41. Haes, A. J.; Van Duyne, R. P. *Journal of American Chemical Society* **2002**.
42. Leff, D. V.; Ohara, P. C.; Heath, J. R.; Gelbart, W. M. *J.Phys.Chem.* **1995**, *99*, 7036.
43. Mirkin, C. A.; Letsinger, R. L.; Mucic, R. C.; Storhoff, J. J. *Nature* **1996**, *382*, 607-09.
44. Lakowicz, J. R. *Analytical Biochemistry* **2005**, *337*, 171-94.
45. Rembaum, A.; Dreyer, W. J. *Science* **1980**, *208*, 364-68.
46. Caruso, F.; Mohwald, H. *J.Am.Chem.Soc.* **1999**, *121*, 6039-46.
47. Schmitt, A.; Fernandez-Barbero, A.; Cabrerizo-Vilchez, M.; Hidalgo-Alvarez, R. *Prog.Colloid Polym.Sci.* **1997**, *104*, 144-49.

48. Elgersma, A. V.; Zsom, R. L. J.; Norde, W.; Lyklema, J. *J.ColloidInterface Sci.* **1990**, *138*, 145-56.
49. Keating, C. D.; Kovaleski, K. M.; Natan, M. J. *J.Phys.Chem.B.* **1998**, *102*, 9404-13.
50. Keating, C. D.; Kovaleski, K. M.; Natan, M. J. *J.Phys.Chem.B.* **1998**, *102*, 9414-25.
51. Macdonald, I. D. G.; Smith, W. E. *Langmuir* **1996**, *12*, 706-13.
52. Xu, H.; Bjerneld, E. J.; Kall, M.; Borjesson, L. *Phys.Rev.Lett.* **1999**, *83*, 4357-60.
53. Gole, A.; Dash, C.; Ramakrishnan, V.; Sainkar, S. R.; Mandale, A. B.; Rao, M.; Sastry, M. *Langmuir* **2001**, *17*, 1674-79.
54. Crumbliss, A. L.; Perine, S. C.; Stonehuerner, J.; Tubergen, K. R.; Zhao, J.; O'Daly, J. P. *Biotech.Bioeng.* **1992**, *40*, 483-90.
55. Storhoff, I. J.; Mucic, R. C.; Mirkin, C. A. *J.Clust.Sci.* **1997**, *8*, 179-216.
56. Alivisatos, A. P.; Johnsson, K. P.; Peng, X.; Wislon, T. E.; Loweth, C. J.; Bruchez, M. P.; Schultz, P. G. *Nature* **1996**, *382*, 609-11.
57. Storhoff, J. J.; Elghanian, R.; Mucic, C. A.; Mirkin, C. A.; Letsinger, R. L. *J.Am.Chem.Soc.* **1998**, *120*, 1959.
58. Taton, T. A.; Mucic, R. C.; Mirkin, C. A.; Letsinger, R. L. *J.Am.Chem.Soc.* **2000**, *122*, 6305-06.
59. Reynolds, R. A.; Mirkin, C. A.; Letsinger, R. L. *J.Am.Chem.Soc.* **2000**, *122*, 3795-96.
60. Elghanian, R.; Storhoff, J. J.; Mucic, R. C.; Letsinger, R. L.; Mirkin, C. A. *Science* **1997**, *277*, 1078-81.
61. Cao, Y. W. C.; Jin, R.; Mirkin, C. A. *Science* **2002**, *297*, 1536-40.
62. Wang, J.; Song, F.; Zhou, F. *Langmuir* **2002**, *18*, 6653-58.
63. Iacopino, D.; Ongaro, A.; Nagle, L.; Eritja, R.; Fitzmaurice, D. *Nanotechnology* **2003**, *14*, 447-52.
64. Imahori, H.; Fukuzumi, S. *Adv.Mater.* **2001**, *13*, 1197-99.
65. Sauthier, M. L.; Carroll, R. L.; Gorman, C. B.; Franzen, S. *Langmuir* **2002**, *18*, 1825-30.
66. Gearheart, L. A.; Ploehn, H. J.; Murphy, C. J. *J.Phys.Chem.B* **2001**, *105*, 12609-15.
67. Bogatyrev, V. A.; Dykman, L. A.; Krasnov, YA. M.; Plotnikov, V. K.; Khlebtsov, N. G. *Colloid J.* **2002**, *64*, 671-80.
68. Zhao, H. Q.; Lin, L.; Li, J. R.; Tang, J. A.; Duan, M. X.; Jiang, L. *J.Nanopart.Res.* **2001**, *3*, 321-23.
69. Patolsky, F.; Ranjit, K. T.; Lichtenstein, A.; Willner, I. *Chem.Commun.* **2000**, 1025-26.
70. Su, M.; Li, S.; Dravid, V. P. *Appl.Phys.Lett.* **2003**, *82*, 3562-64.
71. Liu, T.; Tang, J.; Han, M.; Jiang, L. *Biochem.Biophys.Res.Commun.* **2003**, *304*, 98-100.
72. Glynou, K.; Ioannou, P. C.; Christopoulos, T. K.; Syriopoulou, V. *Anal.Chem.* **2003**, *75*, 4155-60.

73. Wang, J.; Li, J.; Baca, A.; Hu, J.; Zhou, F.; Yan, W.; Pang, D. W. *Anal.Chem.* **2003**, *75*, 3941-45.
74. Zheng, M.; Davidson, F.; Huang, X. *J.Am.Chem.Soc.* **2003**, *125*, 7790-91.
75. Collings, A. F.; Caruso, F. *Reports on Progress in Physics* **1997**, *60*, 1397-445.
76. Wood, R. W. *Proceedings of the Physical Society of London* **1902**, 269-75.
77. Otto, A. *Zeitschrift fur Physik* **1968**, *216*, 398-&.
78. Kretschmann, E.; Raether, H. *Zeitschrift fur Naturforschung Part A-Astrophysik Physik und Physikalische Chemie* **1968**, *A 23*, 2135-&.
79. Agarwal, G. S. *Physical Review B* **1973**, *8*, 4768-79.
80. Swalen, J. D. *Journal of Molecular Electronics* **1986**, *2*, 155-81.
81. Liu, J. Systematic Studies of Protein Immobilization by Surface Plasmon Field-Enhanced Fluorescence Spectroscopy. 2005.
Ref Type: Thesis/Dissertation
82. Hickel, W.; Rothenhausler, B.; Knoll, W. *Journal of Applied Physics* **1989**, *66*, 4832-36.
83. Yu, F. Surface Plasmon Fluorescence Spectroscopy and Surface Plasmon Diffraction in Biomolecular Interaction Studies. 2004. Max-Planck-Institut für Polymerforschung.
Ref Type: Thesis/Dissertation
84. Nelson, B. P.; Frutos, A. G.; Brockman, J. M.; Corn, R. M. *Analytical Chemistry* **1999**, *71*, 3928.
85. Frutos, A. G.; Weibel, S. C.; Corn, R. M. *Analytical Chemistry* **1999**, *71*, 3935.
86. Perez-Luna, V. H.; O'Brien, M. J.; Opperman, K. A.; Hampton, P. D.; Lopez, G. P.; Klumb, L. A.; Stayton, P. S. *Journal of the American Chemical Society* **1999**, *121*, 6469-78.
87. Knoll, W. *Annual Review of Physical Chemistry* **1998**, *49*, 569-638.
88. Jung, L. S.; Nelson, K. E.; Campbell, C. T.; Stayton, P. S.; Yee, S. S.; Perez-Luna, V.; Lopez, G. P. *Sensors and Actuators B-Chemical* **1999**, *54*, 137-44.
89. Spinke, J.; Liley, M.; et al *Langmuir* **1993**, *9*, 1821-25.
90. Axelrod, D.; Burghardt, T. P.; Thompson, N. L. *Annual Review of Biophysics and Bioengineering* **1984**, *13*, 247-68.
91. Burstein, E.; Chen, W. P.; Chen, Y. J.; Hartstein, A. *J.Vac.Sci.Technol.* **1972**, *11*, 1004-19.
92. Raether, H. Surface Plasmons on Smooth and Rough Surfaces and on Gratings, Springer-Verlag: 1988.
93. Nemetz, A.; Knoll, W. *Journal of Raman Spectroscopy* **1996**, *27*, 587-92.
94. Liebermann, T.; Knoll, W. *Colloids and Surfaces A-Physicochemical and Engineering Aspects* **2000**, *171*, 115-30.
95. Homola, J.; Yee, S. S.; Gauglitz, G. *Sensors and Actuators B-Chemical* **1999**, *54*, 3-15.

96. Mckee, T.; Mckee, J. R. *Biochemistry (An introduction)*, Second edition ed.; McGraw-Hill Companies, Inc.: 2001.
97. Knowles, J. R. *Acc.Chem.Res.* **1985**, *18*, 97-104.
98. Albery, W. J.; Knowles, J. R. *Biochemistry* **1976**, *15*, 5588-600.
99. Zhen, G.; Eggli, V.; Vörös, J.; Zammaretti, P.; Textor, M.; Glockshuber, R.; Kuennemann, E. *Langmuir* **2004**, *20*, 10464-73.
100. Livermore, D. M. *Clinical Microbiology Reviews* **1995**, *8*, 557-83.
101. Huang, W.; Wang, J.; Bhattacharyya, D.; Bachas, L. G. *Anal.Chem.* **1997**, *69*, 4601-07.
102. Gordon II, J. G.; Swalen, J. D. *Optics Communications* **1977**, *22*, 374-76.
103. Aust, E. F.; Sawodny, M.; Ito, S.; Knoll, W. *Scanning* **1994**, *16*, 353-61.
104. Atkins, P. W. *Physical Chemistry*, 6th Edition ed.; Oxford University Press: 1998.
105. Rich, R. L.; Myszka, D. G. *J.Mol.Recognit.* **2003**, *16*, 351-82.
106. Homola, J. *J.Anal Bioanal Chem* **2003**, *377*, 528-39.
107. Huang, N.; Voeroes, J.; De Paul, S. M.; Textor, M.; Spencer, N. *Langmuir* **2002**, *18*, 220-30.
108. Park, K. D.; Kim, S. M. *Poly (Ethylene Glycol) Chemistry: Biotechnical and Biomedical Applications*, Harris, J. M., Ed.; Plenum, New York, 1992.
109. Ocallagh, C. H.; Shingler, A. H.; Kirby, S. M.; Morris, A. *Antimicrob.Agents Chemother.* **1972**, *1*, 283-88.
110. Knoll, W.; Zizlsperger, M.; Liebermann, T.; Arnold, S.; Badia, A.; Liley, M.; Piscevic, D.; Schmitt, F.; Spinke, J. *Colloids and Surfaces A: Physicochemical and Engineering Aspects* **2000**, *161*, 115-37.
111. <http://www.piercenet.com> . 2005.
Ref Type: Electronic Citation
112. Kenausis, G. L.; Voeroes, J.; Elbert, D. L.; Huang, N.; Hofer, R.; Ruiz-Taylor, L.; Textor, M.; Hubbell, J. A.; Spencer, N. D. *J.Phys.Chem.B* **2000**, *104*, 3298-309.
113. Huang, N.; Michel, R.; Voeroes, J.; Textor, M.; Hofer, R.; Rossi, A.; Elbert, D. L.; Hubbell, J. A.; Spencer, N. D. *Langmuir* **2001**, *17*, 489-98.
114. Voeroes, J.; Ramsden, J. J.; Csucs, G.; Szendro, I.; De Paul, S. M.; Textor, M.; Spencer, N. D. *Biomaterials* **2002**, *23*, 2710.
115. de Feijter, J. A.; Benjamins, J.; Veer, F. A. *Biopolymers* **1978**, *17*, 1759-72.
116. Jung, L. S.; Nelson, K. E.; Campbell, C. T.; Stayton, P. S.; Yee, S. S.; Perez-Luna, Y.; Lopez, G. P. *Sens.Actuators B* **1999**, *54*, 137-44.

117. Xu, F., Zhen, G., Yu, F., Kuennemann, E., Textor, M., and Knoll, W. *Journal of American Chemical Society* . 2005.
Ref Type: Unpublished Work
118. Gole, A.; Vyas, S.; Phadtare, S.; Lachke, A.; Sastry, M. *Colloids and Surfaces B: Biointerfaces* **2002**, *25*, 129-38.
119. Daniel, M.; Astruc, D. *Chem.Rev.* **2004**, *104*, 293-46.
120. Choy, K. L. *Progress in Materials Science* **2003**, *48*, 57-170.
121. *J.Phys.Chem.B* **2000**, *104*, 460.
122. Liebermann, T.; Knoll, W.; Sluka, P.; Herrmann, R. *Colloids Surf.A* **2000**, *169*, 337-50.
123. Kreibig, U.; Vollmer, M. *Optical Properties of Metal Clusters*, Springer-Verlag: Berlin, Germany, 1995.
124. Link, S.; El-Sayed, M. A. *Int.Rev.Phys.Chem.* **2000**, *19*, 409.
125. Kreibig, U.; Genzel, L. *Surf.Sci.* **1985**, *156*, 678.
126. Weckenmann, U.; Mittler, S.; Naumann, K.; Fischer, R. A. *Langmuir* **2002**, *18*, 5479-86.
127. Reichert, M.; Csaki, K.; Koehler, J. M.; Fritzsche, W. *Anal Chem* **2000**, *72*, 6025-29.
128. Liebermann, T.; Knoll, W. *Colloid Surf.A* **2000**, *171*, 115-30.
129. Homola, J. *Anal Bioanal Chem* **2003**, *377*, 528-39.
130. Rowe-Taitt, C. A.; Hazzard, J. W.; Hoffman, K. E.; Cras, J. J.; Golden, L. P.; Ligler, F. S. *Biosens Bioelectron* **2000**, *15*, 579-89.
131. Piehler, J.; Brecht, A.; Gauglitz, G. *Anal Chem* **1996**, *68*, 139-43.
132. Heideman, R. G.; Kooyman, R. P. H.; Greve, J. *Sens Actuators B* **1993**, *10*, 209-17.
133. Clerc, D.; Lukosz, W. *Sens Actuators B* **1994**, *19*, 581-86.
134. Cush, R.; Cronin, J. M.; Stewart, W. J.; Maule, C. H.; Molloy, J.; Goddard, N. J. *Biosens Bioelectron* **1993**, *8*, 347-53.
135. Natan, M. J.; Lyon, L. A. *Metal nanoparticles*, Feldheim, D. L.; Foss, C. A. J., Eds.; New York, Basel, 2002.
136. Kaetsu, I.; Uchida, K.; Morita, Y.; Okubo, M. *Radiat Phys Chem* **1992**, *40*, 157.
137. Kaetsu, I.; Morita, Y.; Otori, A.; Naka, Y. *Artificial Organs* **1990**, *14*, 237.
138. *Polymer gels*, Washington, DC, 2002.
139. Garland, P. B. *Quarterly reviews of biophysics* **1996**, 91-117.
140. Ostroha, J.; Pong, M.; Lowman, A.; Dan, A. *Biomaterials* **2004**, *25*, 4345-53.

141. Alexa Fluor Hydrazides. <http://www.probes.com/media/pis/mp10436.pdf> . 2004.
Ref Type: Electronic Citation
142. Löfås, S.; Johnsson, B. J. *Chem.Soc., Chem.Commun.* **1990**, *21*, 1526-28.
143. Bartkowiak, A.; Jezierska, I.; Sychai, T. *Polym.Bull.* **1998**, *41*, 191.
144. Martin, J.; Rhoades, T.; Ferguson, T. *J.Anal.Chem.* **1982**, *54*, 1639.
145. Qjima, T.; Nakamoso, A.; Yamamoto, M. *Starch / Starke* **1986**, *38*, 297.
146. Ying, L.; Yin, C.; Zhuo, R. X.; Leong, K. W.; Mao, H. Q.; Kang, E. T.; Neoh, K. G. *Biomacromolecules* **2003**, *4*, 157-65.
147. Uchida, E.; Uyama, Y.; Ikada, Y. *Langmuir* **1993**, *9*, 1121-24.
148. Kang, E. T.; Tan, K. L.; Kato, K.; Uyama, Y.; Ikada, Y. *Macromolecules* **1996**, *29*, 6872.

CURRICULUM VITAE

Surname: Xu

Firstname: Fei

Gender: Female

Nationality: Chinese

Date of Birth: 10th, August, 1978

Phone: +49-6131-4636573

Fax: +49-6131-379100

E-mail Address: xu@mpip-mainz.mpg.de

Xufei201@yahoo.com

Mailing Address: Max-Planck-Institut für Polymerforschung, Ackermannweg 10,
55128 Mainz, Germany

Living Address: Hechtsheimer Str. 37A, Apt. 1427, 55131 Mainz, Germany

Education:

- ✿ 2002 – Present Material Science Group (AK Knoll),
Max-Planck-Institut für Polymerforschung,
Fachbereich Biologie der Johannes Gutenberg-Universität in
Mainz
- ✿ 1999 – 2002 College of Life Science, Jilin University, Changchun, P. R. China
Degree Conferred and Date: Master of Science, July, 2002
- ✿ 2001 – 2002 Institut für Pharmazie, Johannes-Gutenberg Universität Mainz,
Germany, National cooperation project
- ✿ 1995 – 1999 College of Life Science, Jilin University, Changchun, P. R. China
Degree Conferred and Date: Bachelor of Science, Jul, 1999

Publications:

- ✿ Xu Fei, Marco Hill, Xueyan Ma, Lirong Teng, Qingshan Li, Joachim Stoeckigt,
“isolation of a Putative Ribosome Inactivating Protein from Dried Roots of
Trichosanthes Kirilwii Used in Traditional Chinese Medicine”, *Planta med*, 2004,
70, 364-365

- ✱ F.Xu, G.Zhen, E.Zobeley, V.Eggli, R.Glockshuber, M.Textor & W.Knoll, “interfacial binding of beta-lactamase to different matrices monitored by surface plasmon spectroscopy”, *European Cells and Materials*, **2003**, 6, 59
- ✱ Fei Xu, Guoliang Zhen, Fang Yu, Eva Kuennemann, Marcus Textor, Wolfgang Knoll, “Combined affinity and catalytic biosensor: in-situ enzymatic activity monitoring of surface-bound enzymes”, submitted to *Journal of American Chemical Society*.
- ✱ Fei Xu, Anne Kathrena A. Aliganga, Silvia Mittler, Wolfgang Knoll, “Quantification of DNA hybridization based on chemical vapour deposition (CVD) gold particles”, in preparation.
- ✱ Fei Xu, Guoliang Zhen, Marcus Textor, Wolfgang Knoll, “Surface plasmon combined fiber optic absorbance spectroscopy detection for the comparative analysis of surface-bound beta-lactamase based on different interfacial matrices”, in preparation.
- ✱ Fei Xu, Bjoern Persson, Stefan Loefas and Wolfgang Knoll, “Characterization of external stimuli and internal crosslink responses of Carboxymethyl dextran (CMD) for surface plasmon resonance (SPR) applications”, in preparation.
- ✱ Fei Xu, Guoliang Zhen, Marcus Textor, Wolfgang Knoll, “Comparative analysis of planar and particle matrices for the surface-attachment of enzymes and oligonucleotides”, in preparation.
- ✱ Moustafa. A. Abdalla, Fei Xu, Wolfgang Knoll and Klaus Müllen, “Bisbiotinylated perylenediimide as a building block for multilayered nanostructures”, Submitted.